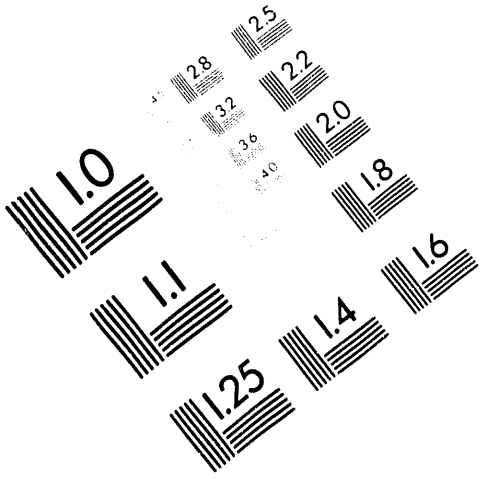

Association for Information and Image Management
1100 Wayne Avenue, Suite 1100
Silver Spring, Maryland 20910
301/587-8202

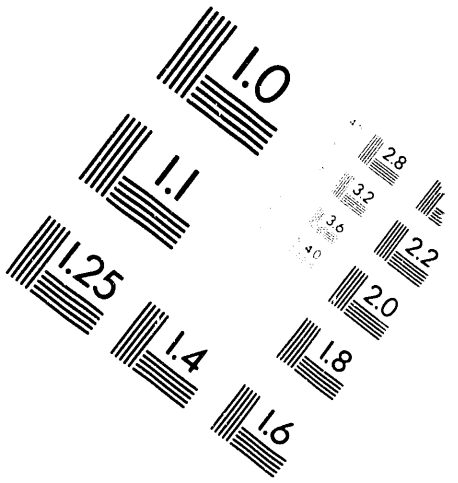

Centimeter

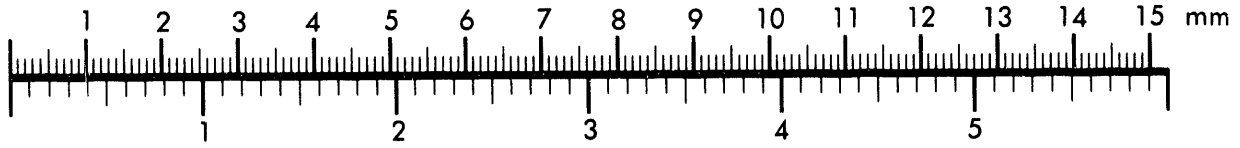

Inches

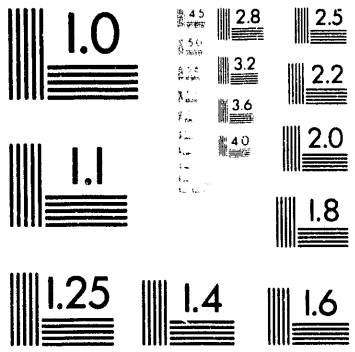

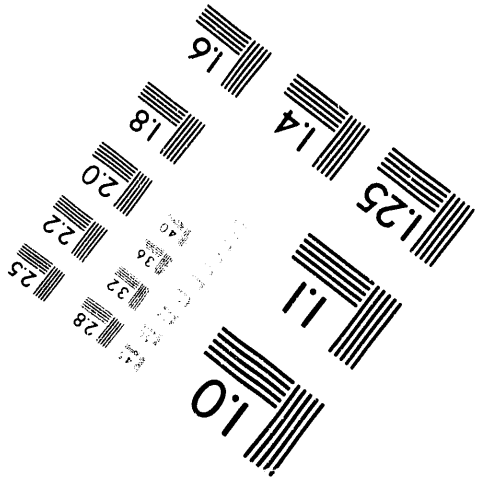

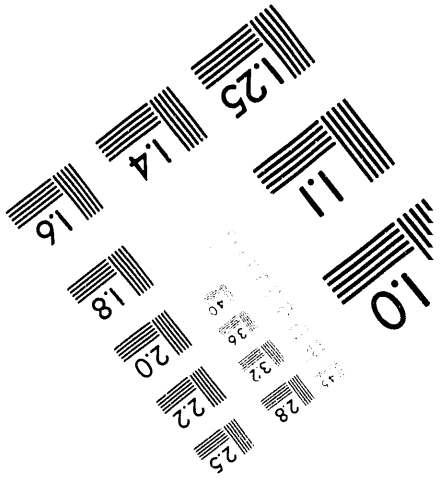

MANUFACTURED TO AIIM STANDARDS
BY APPLIED IMAGE, INC.

1 of 1

DISCLAIMER

Table of Contents

I.

Feasibility Experiment for Sodium-Layer Laser Guide Stars at the Lawrence Livermore National Laboratory

by

C. Max, K. Avicola, H. Bissinger,
J. Brase, D. Gavel, H. Friedman,
J. Morris, S. Olivier, J. T. Salmon
and K. Waltjen

FEASIBILITY EXPERIMENT FOR SODIUM-LAYER LASER GUIDE STARS AT THE LAWRENCE LIVERMORE NATIONAL LABORATORY

C. Max, K. Avicola, H. Bissinger, J. Brase, D. Gavel,
H. Friedman, J. Morris, S. Olivier, J.T. Salmon, and K. Waltjen

Lawrence Livermore National Laboratory
Livermore, CA 94550

ABSTRACT

We are developing a feasibility experiment to demonstrate closed-loop adaptive optics using a sodium-layer laser guide star. We will use the copper-vapor-pumped dye lasers developed for LLNL's Atomic Vapor Laser Isotope Separation Program to create the laser guide star. Closed-loop adaptive corrections will be accomplished using a 69-subaperture adaptive optics system on a one-meter telescope at LLNL. The laser beam will be projected upwards from a beam director approximately 5 meters away from the main telescope, and is expected to form a spot about a meter in diameter at the atmospheric sodium layer (at an altitude of 95 km). Details of the adaptive optics components and an analysis of the expected performance will be presented in companion papers for this Workshop. Here we summarize the overall architecture and system objectives. The long-term goal of our effort is to develop laser guide stars and adaptive optics for large astronomical telescopes.

I. INTRODUCTION

For astronomical applications, sodium-layer laser guide stars[1,2] have a large potential advantage over Rayleigh guide stars[3], because their altitude of about 95 km allows an adaptive optics system to sense an atmospheric path closer to that of a distant astronomical object. As a consequence large astronomical telescopes using sodium beacons should require fewer guide stars to avoid focus anisoplanatism[4], and hence to obtain a given quality of wavefront correction on distant objects.

However, the high altitude of the atmospheric sodium layer and the modest atmospheric column density of atomic sodium result in demanding requirements on the laser needed, in order to make a sodium-layer laser guide star bright enough to do high-order wavefront corrections.

It would be highly advantageous for the largest telescopes (in the 8-10 meter range) to utilize the sodium guide-star technology. To begin to approach this regime, we have undertaken a feasibility demonstration of such a system on a one-meter telescope at the Livermore site, using a laser developed for the Atomic Vapor Laser Isotope Separation (AVLIS) program We have chosen our system parameters such that D / r_o on our one-meter telescope scales to near-infrared observing conditions on the 10-meter Keck Telescope, as shown in Table 1. Here D is the diameter of the telescope primary mirror, and r_o is the atmospheric coherence length[5] at the wavelength used for astronomical observations.

TABLE 1. Atmospheric and Adaptive Optics Parameters for a One-Meter Telescope at the LLNL Site and for the Ten-meter Keck Telescope at Mauna Kea, Hawaii.

Telescope Diameter	Subapertures	Observing Wavelength λ	$r_0(\lambda)$	$D / r_0(\lambda)$
1 meter (LLNL)	69	0.8 microns	10 cm	10
10 meter (Keck)	69	2 microns	0.8 m	12.5

II. LASER PROPERTIES AND BEAM DIRECTOR GEOMETRY

Our feasibility experiment will use the existing AVLIS laser system at Livermore. This system consists of 12 chains of copper vapor lasers, whose green light is used to pump 3 chains of dye lasers. We have re-tuned the dye lasers to produce light at the sodium wavelength of 589 nm. The present laser system has an average power of 1.5 kilowatts in the sodium D_2 line, far larger than will be required for astronomical applications at the best observatory sites. However, the extra laser power affords us the luxury of beginning with more than enough power to achieve closed-loop operations. Later we will "turn down" the laser power in order to investigate the minimum needed for adequate higher-order wavefront correction. Our calculations suggest[6] that 100 Watts of 589 nm light would more than suffice at the largest observatories, for astronomical observations at wavelengths greater than or equal to 0.8 microns.

The AVLIS laser system has several properties that would be very favorable for use in an observatory configuration[7]. It is modular in design, with very long mean-time-between-failure. It is nearly diffraction-limited (measurements indicate between 1.3 and 1.5 times the diffraction limit); this makes it possible to transport the laser beam through vacuum pipes for many kilometers. The laser system is very stable: the copper vapor lasers presently run 24 hours a day for months at a time with very low maintenance. The modules have been engineered for use in a factory setting, and the same attributes of reliability and stability that make them attractive for a factory also would make them attractive for routine use at an observatory. Whatever laser technology is eventually chosen for astronomical applications will have to be engineered for reliability and stability in a manner analogous to the AVLIS laser system. Figure 1 illustrates the kind of power reliability that can presently be expected from the AVLIS dye lasers; for this example the system availability was greater than 90% over the 100-hour run duration.

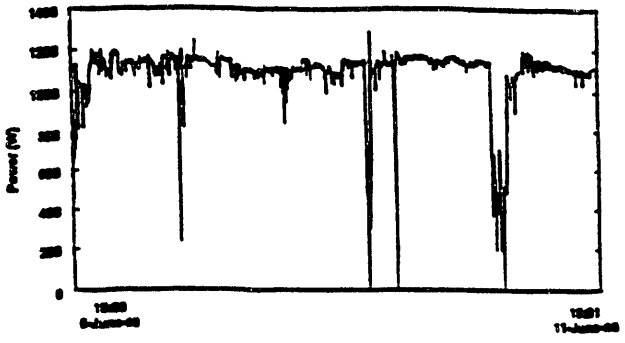

Figure 1. Power delivered by AVLIS dye lasers versus time, from a 100-hour run in 1989. An observatory site would need runs of at most 10-12 hours.

The native pulse format for the AVLIS laser has a peak power sufficiently high that the desired transition in the sodium layer would be saturated. Consequently we are building a pulse stretcher[7] (using an optical delay-line concept) that will lengthen each pulse by a factor of 16. The laser pulse format after stretching will be the following: average power 1.5 kW, pulse repetition frequency 26 kHz, pulse length 800 nsec, peak power 72 kW, and duty factor 2%. With a pulse repetition time of only 38.5 microseconds and a light travel-time of about 33 microseconds through the 10-km-thick sodium layer, the backscattered light from the whole sodium layer will be "smeared out" so as to be almost continuous in time, as seen from the ground. Thus it is convenient to treat our system as if the sodium laser guide star were always "shining".

This laser pulse format suggests a convenient "off-axis" geometry for the laser beam director. Rather than using temporal gating to discriminate against stray light due to Rayleigh scattering on the way up through the atmosphere, we will discriminate against stray light by broadcasting our laser from a separate beam director located about 5 meters to the side of our adaptive-optics telescope. The 5 meter offset is chosen so that light that is Rayleigh scattered from altitudes less than about 30 km is excluded from the field-of-view of the wavefront sensor (10 arc seconds). The geometry is illustrated in Figure 2. Thus it is not necessary to time-gate the wavefront sensor or the electronics packages.

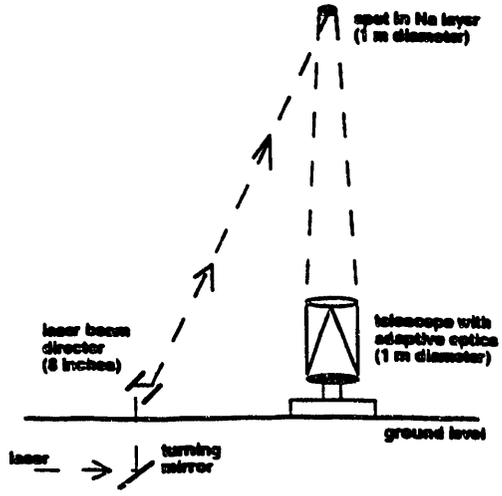

Figure 2. Schematic illustration of beam-director and telescope geometry for the LLNL laser guide star experiment.

The aperture of the upgoing laser beam in the beam director is 5 cm by 10 cm, slightly larger than typical values for r_0 at 589 nm. Calculations of the upward propagation of the laser beam to the sodium layer[6] show that the sodium spot will be about 1 meter in diameter, at a height of 95 km. This spot size will be just slightly resolved by the subapertures of our adaptive optics system.

III. ADAPTIVE OPTICS SYSTEM

Our adaptive optics system will have 69 active subapertures.

We are planning to use an existing Itek continuous face-sheet deformable mirror, in a collaboration with D. Aspinwall, D. Tiszauer and their colleagues at Lockheed. For the longer term, we are also pursuing development of an alternative "hybrid" deformable mirror technology, based on PMN actuators and a grooved continuous face-sheet mirror surface. We have previously built and patented mirrors of this type, but optimized to operate at low bandwidth, in order to correct for low-frequency thermal distortions *within* our laser systems. We are now planning to build and test one to operate at the kilohertz rates required for atmospheric correction. The "hybrid" mirror technology has the potential to be substantially less expensive than mirrors presently available.

Our Hartmann wavefront sensor is based on a new Kodak motion analysis camera with two stages of image intensification. With an allocation of 10 X 10 CCD pixels for each subaperture, the camera functions well at 1000 frames per second[8], allowing us to achieve a closed-loop bandwidth of about 100 Hz. Tests of this wavefront sensor in the laboratory indicate that our stretched-pulse laser guide star will provide sufficient photons to perform full closed-loop corrections for 69 subapertures at the desired observing wavelength of 0.8 microns, at the LLNL site.

Our tip-tilt system will be capable of obtaining tilt information either from the astronomical object (if it is bright enough), or from an off-axis natural tip-tilt guide star. We are designing the tip-tilt system to function with a closed-loop bandwidth of at least 100 Hz, using avalanche photodiodes in a quad-cell configuration as our first-generation tip-tilt sensor. Eventually we plan to experiment with a more advanced tip-tilt sensing system that detects coma, and hence allows us to deduce wavefront tilt more accurately based on a centroid measurement of the tip-tilt guide star[9,10].

We are also implementing a servo system to control the tip-tilt motion of the laser guide star itself, relative to the background stars. This is necessary because the laser beam director is offset to the side of the main telescope, and therefore atmospheric turbulence on the way up will cause the sodium spot to wander relative to the background stars, as seen by the main telescope. We will control the laser guide-star tilt with a separate tip-tilt mirror located below the laser beam director.

We are experimenting with a wavefront reconstructor based on commercial board-level parallel processing, using four Intel i860 vector processors. We plan to investigate several reconstruction algorithms, and to compare their performance to that of a more traditional array-processor-based reconstructor, in collaboration with D. Aspinwall, D. Tiszauer and their colleagues at Lockheed.

IV. SYSTEMS ANALYSIS AND SIMULATIONS

We are constructing two types of models to aid in analyzing the performance of our laser guide star and adaptive optics system[6].

The first is a "bottoms-up" calculation of the residual wavefront errors that we should expect, using statistical expressions for the root-mean-square errors of all the relevant subsystems. Residual errors are calculated separately for the tip-tilt (jitter) control loop and for the higher-order-correction control loop. Each of these two control loops is affected by the accuracy of *sensing* the relevant wavefront aberrations (which depends on signal strength, integration time, detector efficiency, and noise properties), and the accuracy of *correcting* the relevant aberrations (which depends on the number of subapertures, the servo control bandwidth compared to the atmospheric turnover frequency, and the offset angle of the guide star). This model was developed in collaboration with R. Vernon of SAIC. It runs on a Macintosh computer, as an *Excel* spreadsheet

Our predictions for the LLNL feasibility experiment using this model are baselined at $r_0 = 5$ cm at 0.5 microns, corresponding to approximately 2 arc second seeing. (Our data on seeing and r_0 are not yet comprehensive, but we typically measure seeing of 2 arc sec on our better nights.) The baseline model predicts higher-order Strehl ratios of approximately 0.5 for observations at 0.8 micron wavelength. Under these conditions the corresponding spatial resolution is determined by the quality of the tip-tilt correction[9], and should vary between 0.15 and 0.6 arc sec depending on the proximity and brightness of the tip-tilt guide star.

The second type of model we are developing is a Monte Carlo simulation of the laser guide star and adaptive optical system. As shown in Figure 3, this model consists of a linked series of simulations representing sub-systems of the feasibility experiment. The atmospheric turbulence is represented by specific realizations on discrete phase screens, with statistics derived from the appropriately scaled Kolmogorov spectrum.

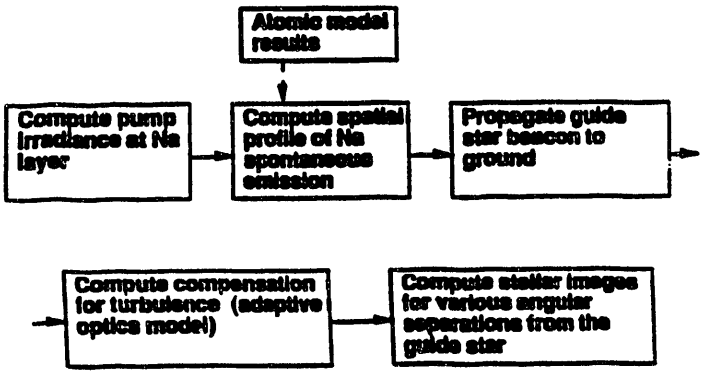

Figure 3. Schematic representation of Monte Carlo simulation model for the LLNL laser guide star experiment.

We begin by propagating the laser beam upwards through a representative set of turbulence phase screens. Once the incident intensity distribution at the sodium layer is known, we calculate the consequent emission of 589 nm light. At present this sodium-layer simulation includes a 6-level Bloch equation representation of the atomic states, with 120 Doppler bins. Figure 4 shows a typical intensity distribution for sodium-layer emission, using our stretched laser pulse format.

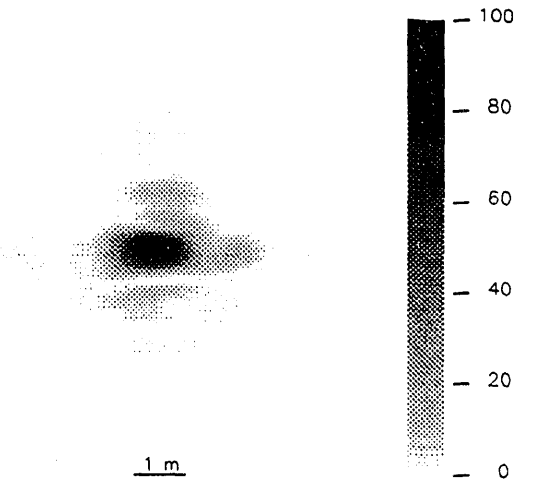

Figure 4. Predicted intensity distribution of sodium emission for our stretched laser pulse, assuming r_0 = 5 cm. The characteristic "cross-shaped" diffraction pattern is due to the rectangular shape of the laser beam at the beam director (5 cm by 10 cm). At the sodium layer, the central core is roughly 1 meter in size.

The sodium-layer emission must then be propagated down again through the atmosphere (using more turbulent phase screens) to the wavefront sensor, forming the perturbed wavefront which the adaptive optics system will try to correct. Next, a Hartmann wavefront sensor model (including noise, realistic lenslets, and appropriate pixel sizes) calculates the centroids that would be measured from the perturbed wavefront. If desired, these centroids can be used as inputs to a wavefront reconstructor, which generates instructions for a model deformable mirror. The quality of the final correction is calculated by applying the shape of the deformable mirror to the wavefront from a distant astronomical object.

Figure 5 illustrates this last segment of the simulation process. In this case we have simplified the simulation by using a natural guide star (in the upper left-hand corner of the field, at position 0,0) to obtain the wavefront information. The astronomical object is an open cluster of stars. The left frame shows the uncorrected image of the star cluster, while the right frame shows the same field of view after correction. We are using simulations such as this to study the effect of anisoplanatism. In this example the Strehl falls from 0.3 for stars nearest the natural guide star to 0.15 for stars farthest from the natural guide star.

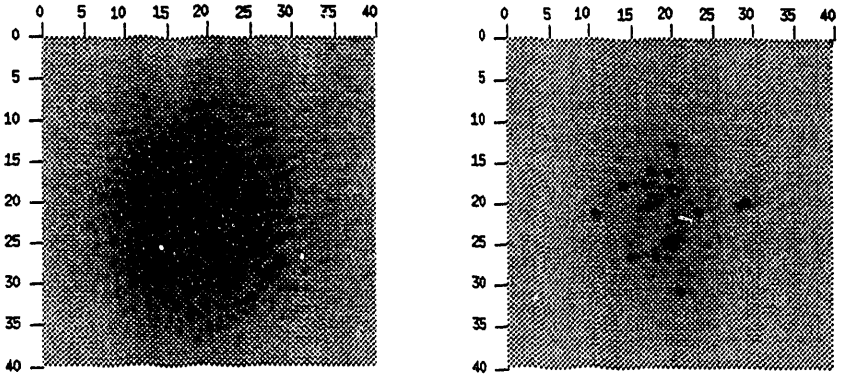

Figure 5. Simulation of adaptive optical correction for an open star cluster, using a natural guide star for the wavefront reference. The scale is in microradians (5 microradians is approximately 1 arc second).

V. EXPERIMENTAL PLANS

Our first experiments will characterize the sodium-layer laser guide star, including its intensity distribution, total energy, and sensitivity to laser pulse format. We will project the laser straight upwards, and characterize the spot in the sodium layer using a half-meter telescope located a few meters from the beam director. At the same time we will be measuring the atmospheric turbulence using a quarter-meter telescope, so that we will be able to relate the intensity distribution and size of the sodium spot to atmospheric parameters such as r_0. We will use our wavefront sensor on the half-meter telescope to measure the wavefront from the pulse-stretched sodium guide star at a 1 kHz sample rate. Wavefronts from the un-pulse-stretched laser guide star will be measured with a slower sample rate, due to its lower intensity. The observing site for these first experiments is located above a pre-existing evacuated laser beam tube at LLNL, and is not optimal for astronomical observations due to its proximity to an office building.

Closed-loop adaptive optics experiments will take place on a new one-meter telescope, which will be sited in a field at LLNL farther from surrounding structures. The laser beam tube will be extended under-ground to this new observing site, where it will feed the laser beam directly into an alt-azimuth beam director located about 5 meters from the telescope. The start date for these closed-loop experiments will be determined by delivery of the new telescope, presently scheduled to occur in mid-1992 at the earliest. All closed-loop adaptive optics experiments will be accompanied by atmospheric measurements on an adjacent telescope, so that the actual adaptive corrections achieved can be compared with the corresponding performance predicted for similar atmospheric parameters.

Specific issues that we wish to address include the size of the isoplanatic patch for both tip-tilt and higher-order corrections, the optimum laser pulse format and frequency modulation, the effect of laser beam polarization, and the realistic utility of laser guide stars and adaptive optics for different types of astronomical observations.

Research supported by the US Department of Energy under contract number W-7405-ENG-48 to the Lawrence Livermore National Laboratory.

REFERENCES

1 R. Foy and A. Labeyrie, Astronomy and Astrophysics 152, 129 (1985).
2 L.A. Thompson and C.S. Gardner, Nature 328, 229 (1987); R.A. Humphries et al., Optics Letters 16, 1367 (1991).
3 R. Fugate et al., Nature 353, 144 (1991); C. Primmerman et al., Nature 353, 141 (1991).
4 R. Vernon, private communication; Lincoln Laboratories and the Optical Sciences Corp., unpublished reports; B. Welsh and C.S. Gardner, JOSA A 8, 69 (1991).
5 D.L Fried and G.E. Meyers, Applied Optics 13, 2620 (1974).
6 Donald Gavel et al., LLNL, paper presented at this Workshop.
7 Herbert Friedman et al., LLNL, paper presented at this Workshop.
8 Kenneth Avicola et al., LLNL, paper presented at this Workshop.
9 Scot Olivier et al., LLNL, paper presented at this Workshop.
10 G.A. Tyler, report number TR-634, the Optical Sciences Corporation (1985).

II.

System Design for a High Power Sodium Beacon Laser

by

H. Friedman, J. Morris, and J. Horton

System Design for a High Power Sodium Beacon Laser

Herbert Friedman, James Morris and James Horton
Lawrence Livermore National Laboratory
Livermore, CA

I. Background

Sodium laser guide stars have been proposed[1,2] as a means to correct for the effects of atmospheric turbulence in large astronomical telescopes. Several groups[3-6] have produced such guide stars, but as yet, none has been able to close a control loop for an adaptive optics system using this means largely because of the limited power available in the laser system. In this paper, the effort to utilize a high power laser system developed by LLNL for laser isotope separation, for the generation of a sodium guide star, is described.

The requirements of the laser system are developed by examining the photon signal necessary to achieve sufficient signal to noise in the wavefront detector. The laser system developed for isotope separation is described and the performance characteristics are presented. A novel optical apparatus for reducing the peak power of the laser system to optimize the backscatter return is also described. The beam transport system presently under development at LLNL is discussed and the design for a smaller version of the laser system suitable for deployment at an astronomical site is shown.

II. Laser Power Requirements

The parameters of the sodium layer in the mesosphere are well known[7] and are summarized in Figure 1. As a best case calculation, if all the sodium atoms within a column were excited by a tuned laser beam, the photon rate at a detector on the ground is given by the relation in Figure 2 and would yield a return signal shown in Figure 3 for the parameters listed therein. A typical value for the required number of photons in an atmospheric sampling time and in a wavefront sensing subaperture is of the order of 2000. Thus, for the photon rate of 1.9×10^8/sec, at least 10 μsec of signal integration is required and based upon an atmospheric sampling time of 1 msec, the minimum duty cycle required for the sodium layer is of the order of 1%.

This calculation indicates that there are at least 100 times more sodium atoms present in the mesosphere than are required to receive sufficient signal to close a control loop. The laser power required to achieve that return signal depends critically upon the spectral match between the laser and the sodium absorption line and the laser flux as compared to the saturation level. In terms of saturation, Figure 4 illustrates an often confusing point. The photon return is a monotonically increasing function of laser power for a fixed pulse format, i.e., ratio of peak to average power or $(\text{duty factor})^{-1}$. The more important case is for fixed average power wherein the photon return decreases as the duty factor decreases. Increased peak power saturates the sodium transition driving the radiation forward and away from the receiver. The laser to be used in these experiments has an average power capability of a kilowatt and pulse repetition frequency of 26 kHz which corresponds to a pulse energy of 38 mJ. For the pulse duration of 32 ns (FWHM) as shown in Figure 5, the peak power over a one meter spot at the sodium layer is of the order of 75 W/cm^2 which is approximately 15 times the saturation flux. A pulse stretcher with a strecth factor of 15 is under construction and is described later in this paper.

The effects of laser pulse width and modulation on the efficiency of backscatter are illustrated in Figure 6. The calculations are based on single pulse effects since the interpulse duration of 38 μs is much greater than either the spontaneous lifetime (16 ns). The unmodulated case assumes two lines spaced 1.8 GHz apart with transform limited spectral widths, a few tens of megahertz, while a modulation format has broadened each line to match the sodium linewidth. For an unstretched pulse with a width of 32 ns (FWHM), the pulse energy at 1 kW average power is 38 mJ and the calculation shows an increase of 2.3 between the modulated and unmodulated pulse returns. The effects of modulation are minimized in the unstretched case because both pulses saturate the sodium layer heavily. When the laser is pulse stretched by a factor of 15, which is our baseline case, the pulse energy within one 32 ns "subpulse" is reduced to 2.5 mJ and the effect of modulation is to increase the backscatter efficiency by 3.5 times.

The effect of pulse stretching on the backscatter efficiency is shown in Figure 7 for our basic pulse format shown in Figure 5. The solid lines indicate the photon return assuming that all the laser power is uniformly distributed within a spot diameter of 1.3 meters. The photon return for a stretched pulse format is over four times that of the unstretched pulse at the kilowatt power level. Using a propagation model, the spot size is not uniformly distributed but spreads due to diffraction and turbulence. The photon returns from the 2 meter diameter central portion of the spot and from the entire spot are also indicated. In this calculation the laser beam was assumed to be a rectangle with dimensions 5 cm x 10 cm and diffraction limited. Beam propagation through an atmosphere with r_0=5 cm (at 500 nm) was calculated and an example of the spot irradiance and D_2 emission using the propagation model is shown in Figure 8.

The amount of laser power needed to generate a photon return signal sufficient to close a control system is critically dependent upon the sensitivity and noise characteristics of the receiver. Although LLNL and others are actively involved in CCD development, no suitable CCD chip is presently available to us. We have chosen a wavefront measurement system based upon a high speed, image intensified camera, Kodak Ektapro, which is described elsewhere in this Workshop[8]. Calibration data from the camera shown in Figure 9 indicate that a minimum of approximately 500 photons collected in a subaperture are required to achieve a maximum acceptable wavefront measurement error of approximately 1/8 wave. Also shown on the plot are the estimated performance of our kilowatt laser system for various pulse formats. If our laser system is stretched to achieve pulse widths of 750 ns, we can use this camera with integration times of 1 ms and a subaperture diameter of 5 cm to measure the wavefront of the sodium guide star. Increasing the integration to 2 ms provides margin without a strong penalty in overall system performance.

III. Laser System Design

The high average power laser system developed at LLNL for the Atomic Vapor Laser Isotope Separation (AVLIS) program is ideally suited for this sodium beacon application. The laser system is capable of producing in excess of a kilowatt of average power tuned to the sodium line at 589 nm. The high PRF of 26 kHz minimizes the peak power in order to reduce saturation effects. The bandwidth of the laser is narrow and stable to a few tens of megahertz and the capability exists to modulate the laser beam to match the sodium spectral profile. The system also has the capability to correct the wavefront for low (spatial and temporal) frequencies using a closed loop deformable mirror system and a beam quality of less than 1.5 times the diffraction limit at high average power has been achieved.

The design concept for the AVLIS laser system is shown in Figure 10 and consists of twelve chains of Copper Vapor Lasers (CVL's) pumping three chains of dye lasers. For the guide star application, one of the dye laser chains is tuned to the sodium wavelength and the beam is diverted to an underground turning vault where an up turn mirror diverts the beam into the atmosphere. For the AVLIS process, the dye lasers are combined into one beam and multipassed through metallic uranium vapor in order to achieve isotope enrichment by selective photoionization. The multipass cell also has application for the guide star program. High quality mirrors and optical coatings with extremely low loss have been developed and these components find application in an optical system to stretch the dye laser pulse thereby reducing the effects of saturation in the sodium layer.

A photograph of an individual CVL and the chain configuration is shown in Figure 11. An individual chain of CVL's consisting of an oscillator and three, single pass amplifiers has produced over 1.5 kW. A portion of the array of 12 CVL chains is also shown in Figure 11 and this array routinely produces over 8 kW as indicated in Figure 12.

The CVL chains pump a set of three dye laser chains through a highly redundant optical transport system which insures that every dye laser amplifier is pumped by a small portion of each CVL chain. The characteristics of the dye laser system are listed in Figure 13 and a high power run is shown in Figure 14. The high power dye laser chain, which is the one to be used for the guide star operation, has produced over 1.5 kW of average power at a pulse repetition rate of 2ϵ kHz. Wavelength stability and beam quality at high average power are shown in Figures 15 and 16.

IV. Pulse Stretcher

In order to stretch the pulse of the dye lasers to reduce saturation effects, a multipass optical system consisting of multiple White cells has been designed. The concept is illustrated in Figure 17. A series of optical delay lines of 1, 2, 4 and 8 times the input pulse width and 50/50 beam splitters creates a stack of 16 subpulses for every input pulse. Each subpulse is of equal magnitude, neglecting coating losses for the moment, so that the effect is to lower the intensity by a factor of 2^4=16. The result is two separate beams which can be combined using polarization techniques or left as two parallel beams to be overlapped in the mesosphere. The AVLIS program has developed high power coatings with reflection coefficients of 0.998 or better so that the effect of coating losses is approximately an 11% droop at the end of the train of subpulses.

A novel optical technique[8] of realizing this pulse stretcher concept is shown in Figure 18. The input pulse is split in two by the 50/50 beam splitter with half going through the first delay and the other half reflecting off the mirror. The half which is delayed is indexed down one unit and is combined with the reflected pulse and half of that combined pulse is delayed further. The output of each delay line is indexed down one unit and combined with the reflected pulse until the required number of delays is achieved. The two outputs can be combined into one beam or left as individual outputs.

One design parameter which remains to be specified is the delay between pulses. If the input pulse is a flat top, then the optical delay unit which leaves no gaps between the subpulses is exactly equal to the input pulse width. For the realistic case of the dye laser pulse shown in Figure 5, the delay unit is chosen to minimize pulse overlap. Figure 19 shows the results of a code calculation varying the length of the optical delay unit. For a delay line unit of 100 ns, which is larger than the pulse width, the subpulses are completely separated and no overlap occurs. This is certainly the best situation except that the delay lines are unduly long and take up valuable real estate. For a delay unit of 60 ns, approximately equal to the Full Width Full

Maximum (FWFM), the photon return is 90% of the full separated case whereas the return signal drops to 75% for a 40 ns delay which is approximately the Full Width Half Maximum (FWHM). Our design chooses 60 ns as the delay line unit.

The White cell concept is illustrated in Figure 20. Three mirrors of identical radii of curvature are used with the field mirror and objective mirrors separated by the radius of curvature. The center of curvature of the field mirror is located between the two objective mirrors and the centers of the objective mirrors are located symmetrically about the center of the field mirror. The minimum number of passes for this geometry is four so that a separation of 15 feet yields the optical delay unit of 60 feet or approximately 60 ns. The other optical delays are obtained by having the input pulses enter the White cell above and exit below the central plane formed by the three centers of curvature at the appropriate distances.

Figure 20 also shows the results of an experiment performed several years ago with a White cell used as a pure delay line. A pulse was injected above the central plane at such an angle as to require 150 passes to exit the White cell. A camera viewing the rear of the field mirror recorded the laser spots leaking through the coating. The scope trace of the photodiode shows a delay of 5 μs for the 150 passes at 10 m per pass with an attenuation of only 26% corresponding to a mirror reflectivity of 0.998.

The entire pulse stretcher can fit into a pipe one foot in diameter and 20 feet long, as shown in Figure 21. For the first set of experiments, multiple White cells are used in a large vacuum chamber, Figure 22. This more versatile arrangement will allow us to develop a control system architecture which minimizes cost and provides maximum beam stability.

V. Deployment at LLNL

The laser guide star experiment will be deployed in two phases at LLNL. Figure 23 shows the layout of the AVLIS complex. The beam exits the Laser Demonstration Facility (LDF) through an underground, evacuated pipe winding up at the first turning vault at the corner of the office complex. This turning vault contains an underground vacuum chamber with steering mirrors, a closed loop pointing and centering control system, fast and slow shutters and the up turn mirror, see Figure 24. The beam is directed through a pipe exiting the pipe at an elevation of 10 feet above grade through a window which is the final vacuum-to-air interface as shown in Figure 25. Presently at the site are a 1/4 meter telescope for atmospheric measurements and a 1/2 meter telescope which will be used for radiometric measurements of the laser guide star.

In the second phase of the experiment, a 1 meter telescope will be located approximately 150 feet to the east of the present site away from buildings and trees. The laser beam will be transported to this site through another underground, evacuated pipe and delivered to a beam director. The laser beam director and telescope will be synchronously driven to track astronomical objects of interest with the laser guide star place in the middle of the field of view.

VI. Compact Laser System

Although we predict that a kilowatt of laser power will be necessary at LLNL due to the small value of r_0=5 cm, much smaller power lasers are needed at a good astronomical site such as Mauna Kea. A subset of the AVLIS lasers has been chosen and a package design is shown in Figure 26. The laser package contains a single chain of CVL's with output of 1500 W.

Since only the 510 nm lines is useful for pumping a dye at 589 nm, the output power at the sodium wavelength is 350 W. Six hundred watts of 578 nm light is also available and studies are underway to design a hybrid guide star format using both Rayleigh and sodium beacons.

The CVL's occupy one side of the vertical optical bench, or monolith as it is sometimes called, and the dye laser chain is mounted on the other side. There is room for the pulse stretcher below the dye laser chain although not shown on the sketch. The CVL's are coupled to the dye laser using fiber optic cables which reduces the complexity of the beam transport system. Indeed, the CVL's could be located remotely from the dye lasers by as much as a few hundred feet. Such a configuration would permit a central location for the CVL's in the midst of a multi telescope installation with smaller dye lasers located close to each unit. The total power consumption for the unit as shown in the figure is approximately 200 kW and the footprint is approximately 160 sq. ft. The unit could be pallet mounted or transported in a small enclosed trailer.

VII. References

1. R. Foy and Labeyrie, Astron. Astrophys. **152**, L29 (1985)

2. L. A. Thompson, C. S Gardner, Nature, **328**, 229, (1987)

3. R. Q. Fugate et al., Nature, **353**, 144, (1991)

4. R. A. Humphries et al., Opt. Lett. **16**, 1367, (1991)

5. E. Kibblewhite, Univ. Chicago, Private Comm. (1991)

6. C. S. Gardner, IEEE, **77**, 3, (1989)

7. G. Megie, F. Bos, J. E. Blamont and M. L. Chanin, Planet. Space Sci., **26**, (1978)

8. J.A. Horton, Patent Applied, 1992

Atomic parameters		
Sodium D_2 line wavelength	λ_{Na}	589 nm
Spontaneous emission lifetime of D_2 line	τ_n	16 ns
Degeneracy correction factor for D_2 line	$g_u/(g_l + g_u)$	0.67
Atmospheric sodium layer parameters		
Column density at zenith	N	5×10^{13} m^{-2}
Mean alitiude	z	≈ 90 km
Vertical depth		25 km
Optical depth at zenith (3 Ghz bandwidth)		0.025
Atmospheric linear propagation parameters		
Transmission coefficient, ground to sodium layer		0.85
r_0 at the sodium D_2 line wavelength		≈ 0.05 m
Illuminated spot area at the Na layer (41° slant path)	A_s	1.13 m^2
Nominal isoplanatic angle at 1μm wavelength		10 μrad
Wavefront sensor		
Sub-aperture area	AWFS	0.01 m^2

Figure 1. Physical data for sodium beacon.

$$\begin{pmatrix}\text{photon}\\ \text{rate}\end{pmatrix} \le \begin{pmatrix}\text{atoms}\\ \text{illuminated}\end{pmatrix} \times \begin{pmatrix}\text{spont. em.}\\ \text{rate}\end{pmatrix} \times \begin{pmatrix}\text{degeneracy}\\ \text{correction}\end{pmatrix} \times \begin{pmatrix}\text{collection}\\ \text{efficiency}\end{pmatrix}$$

$$\dot{N}_{ph} \le A_s N \frac{1}{\tau_n}\left(\frac{g_u}{g_l+g_u}\right)\left(\frac{A_{WFS}}{4\pi z^2} X\right)$$

where
- A_s = illuminated spot area at Na layer
- N = Na column density
- τ_n = spontaneous emission lifetime of Na D_2 line
- $g_{l,u}$ = degeneracy factor for (lower, upper) state
- z = distance to Na layer along propagation path
- A_{WFS} = area of wavefront sensor sub-aperture
- X = atmospheric transmission loss factor from Na layer to the beam director

Figure 2. Useful photon return rate limit for atmospheric sodium layer.

$$\begin{pmatrix}\text{photon}\\ \text{rate}\end{pmatrix} \le \begin{pmatrix}\text{atoms}\\ \text{illuminated}\end{pmatrix} \times \begin{pmatrix}\text{spont. em.}\\ \text{rate}\end{pmatrix} \times \begin{pmatrix}\text{degeneracy}\\ \text{correction}\end{pmatrix} \times \begin{pmatrix}\text{collection}\\ \text{efficiency}\end{pmatrix}$$

$$\boxed{\dot{N}_{ph} \le 1.9 \times 10^8 \quad \text{sec}^{-1}}$$

implies

$$\boxed{\begin{array}{l}\text{pulse length} \ge 10\ \mu\text{sec}\\ \text{or} \quad \text{duty cycle} \ge 1.0\ \%\end{array}}$$

for $N = 5 \times 10^{13}$ atoms / m^2, $z = 90$ km, $A_{WFS} = .01$ m^2, $X = 0.85$, and a 1.2 m diameter illuminated spot at the Na layer.

This is a requirement for all pulse formats. The Na layer cannot emit photons at a higher rate.

Figure 3. Useful photon return rate limit for atmospheric sodium layer.

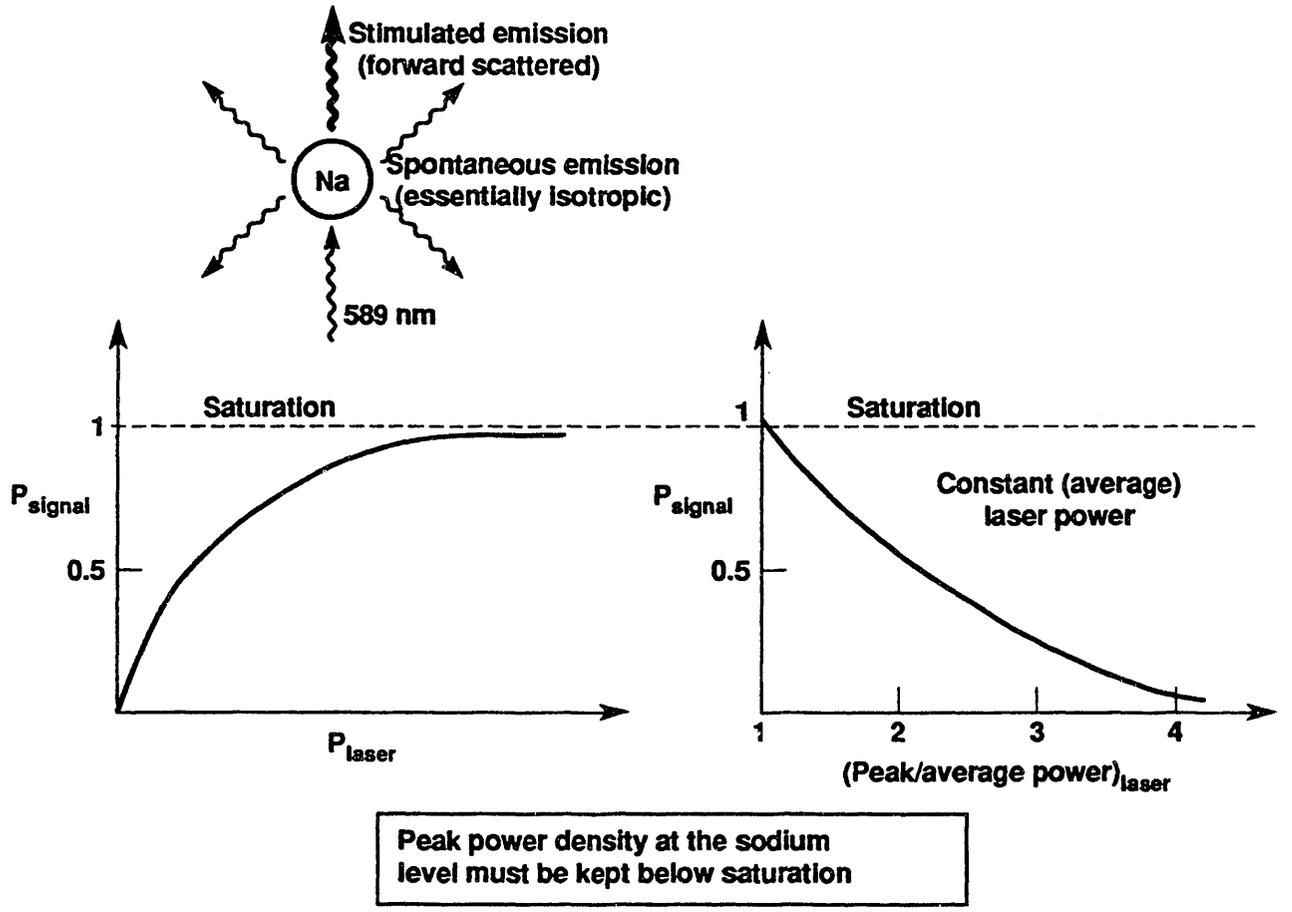

Fig. 4. Saturation effects reduce signal levels at the ground.

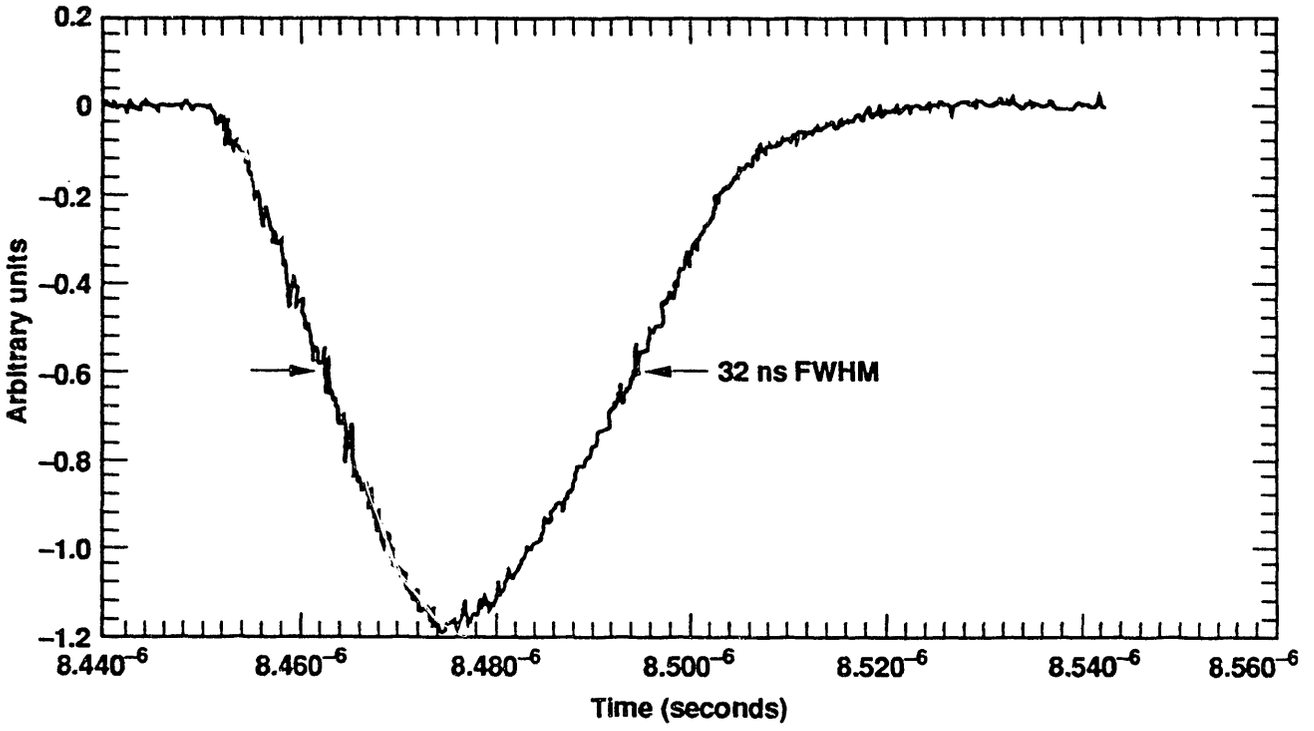

Fig. 5. Dye laser pulse format.

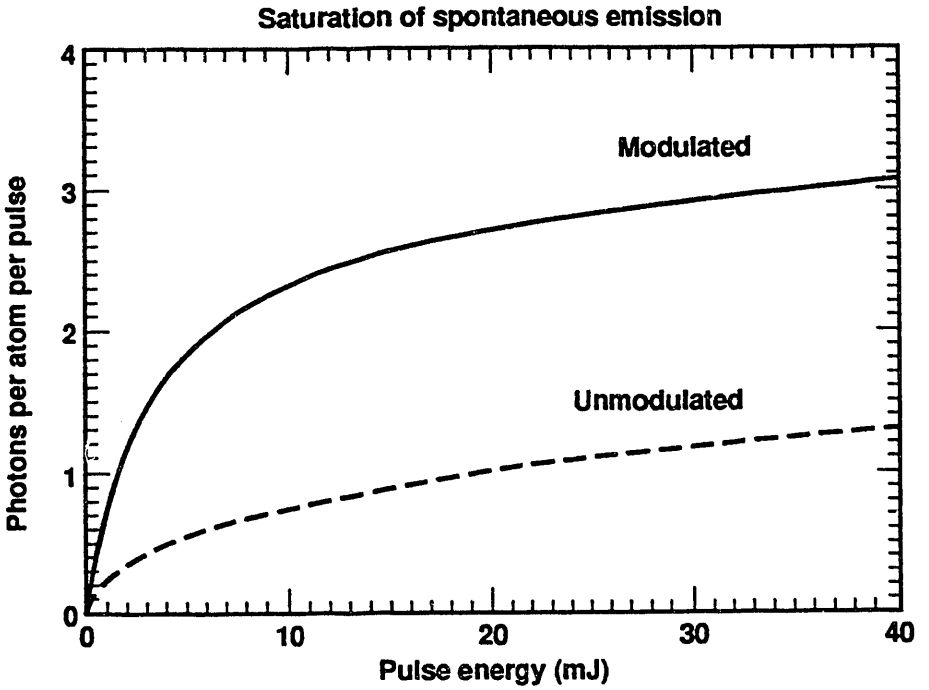

D = 1.3 m uniformally illuminated spot

0.72 atm. transmission

Linear polarization

Actual line profile, 2-level Bloch calculation

32 ns FWHM gaussian pulse

Fig. 6. For our pulse conditions, modulation matched to Na spectrum is 3 times more efficient than unmodulated.

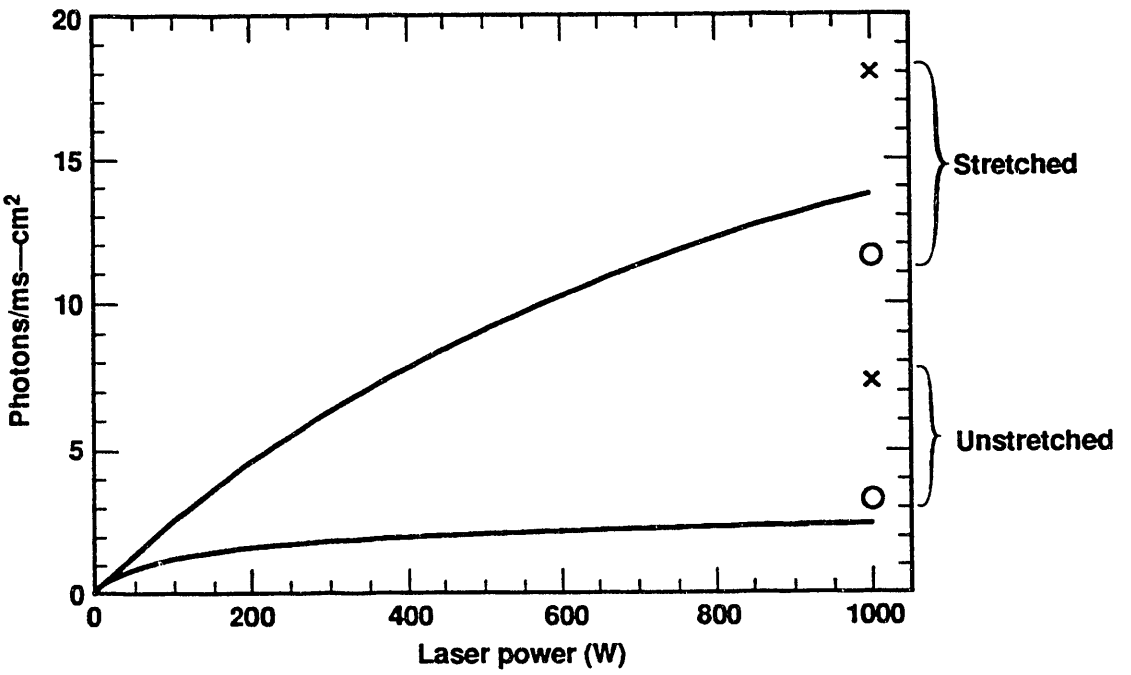

—— Laser power uniformly distributed in 1.3 meter spot

O, × Propagation model (r_o = 5 cm at 500 nm) with backscatter return from (2 meter, entire) spot

Calculation parameters: 6 level Bloch equations
60% atmospheric transmission
Stretch factor = 15
Individual pulse width = 60 ns (FWFM)

Fig. 7. Backscatter return from modulated pulse format

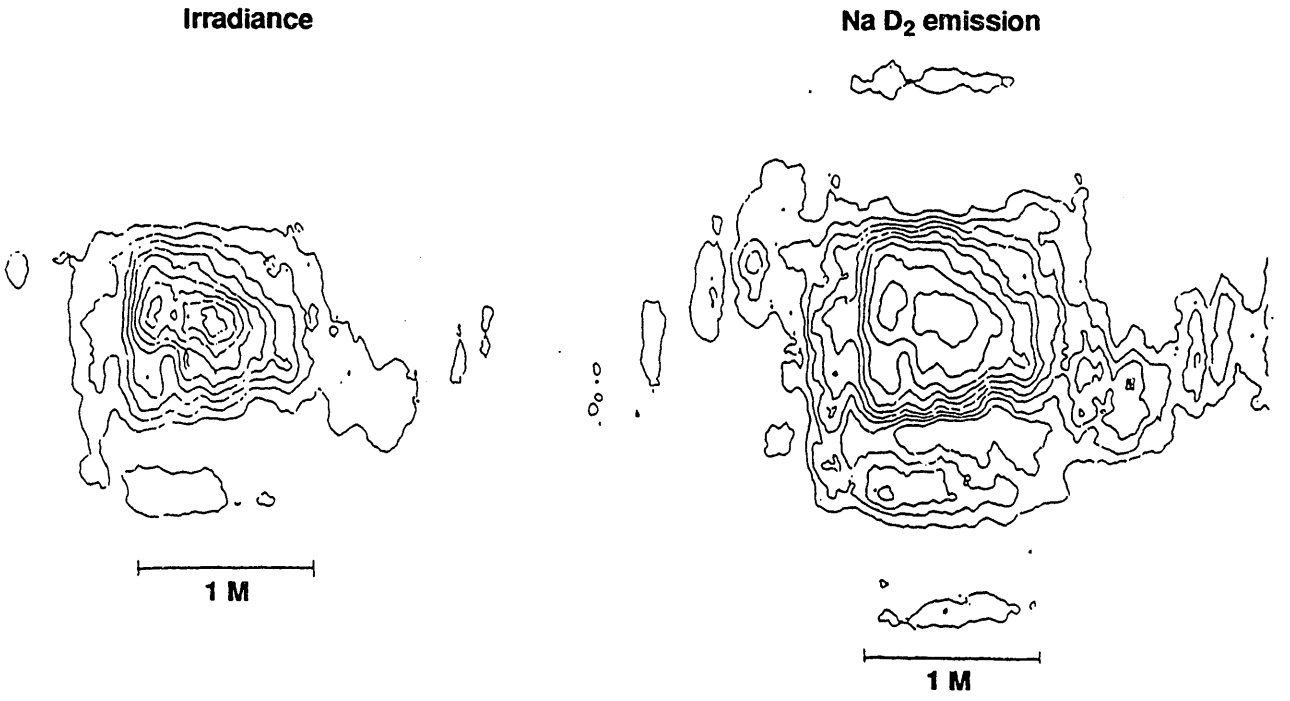

Fig. 8 Irradiance and Na D_2 emission profiles at 10× pulse stretch for a 5 × 8 cm beam and r_0 = 5 cm (at 500 nm)

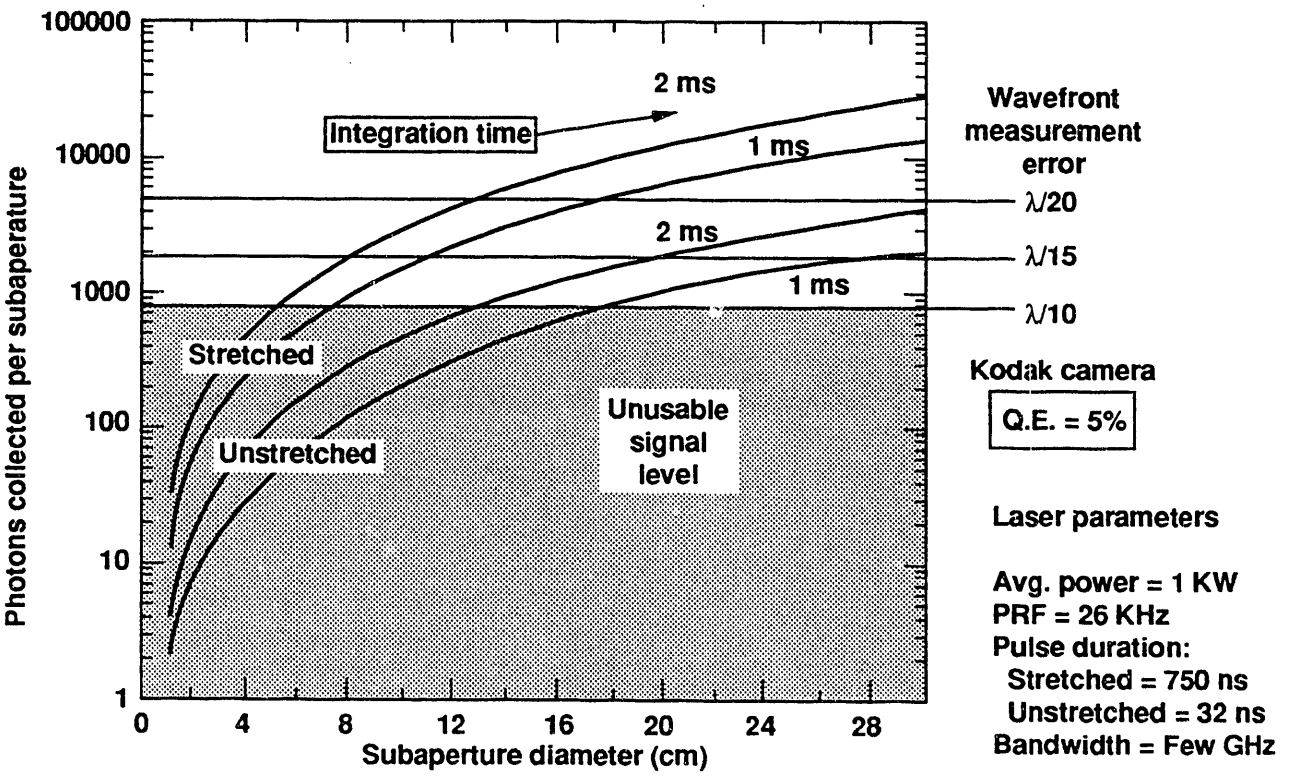

Fig. 9 Guide star signal levels and wave front sensor performance for Kodak camera

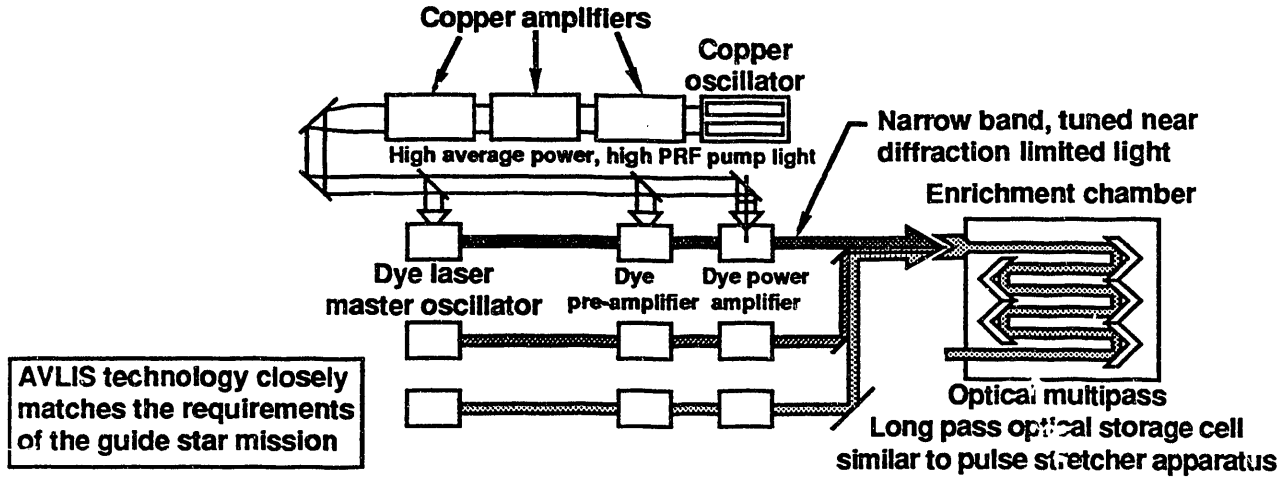

Fig. 10 AVLIS laser system design concept

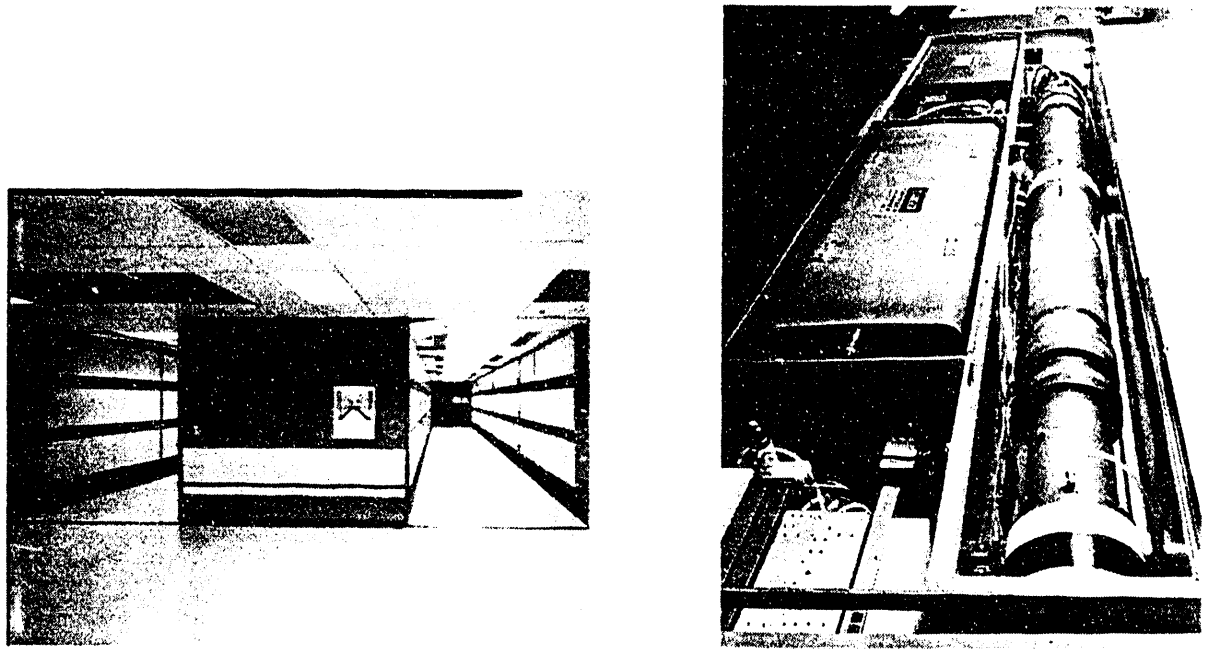

SIS plant scale lasers at 750 W per chain

U–AVLIS plant engineering prototype at 1500 W per chain

Lifetime and operating data at full power to be collected in Laser Demonstration Facility

Fig. 11 Copper lasers operated at plant power

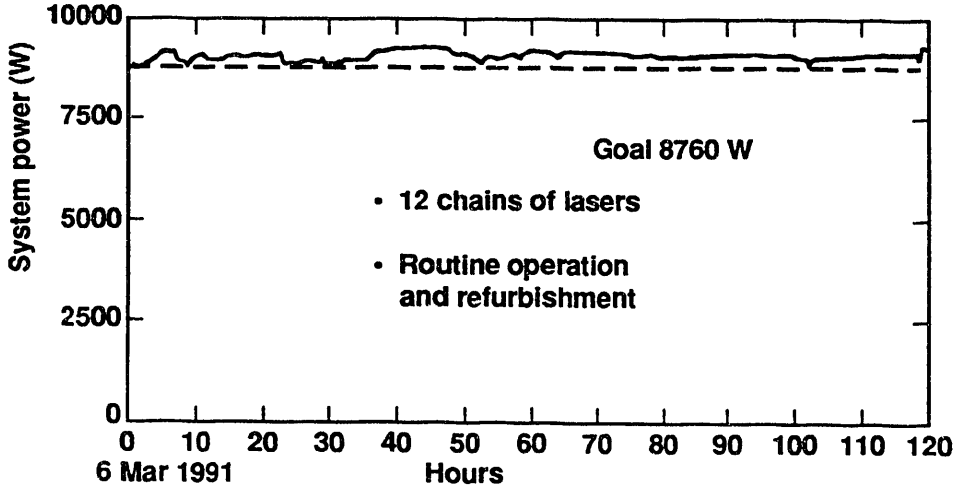

Fig. 12 Copper lasers system performance–corridors 1 and 2

Parameter	Value	Comments
Average power (sustained/highest)	>1300 W/1500 W	Single chain
	>2500 W/2800 W	Total system
Dye conversion efficiency	>50%	ASE<5% typical
Wavelength range	550–650 nm	With available dyes
Wavefront quality	<λ/10 RMS	Using adaptive optics
Center frequency stability	±50 MHz	
Bandwidth	50 MHz - 5 GHz	Modulated single-mode
Repetition rate	13 kHz	Capable of 26 kHz
Pulse width	40 ns	FWHM

Fig. 13. Dye laser system performance summary.

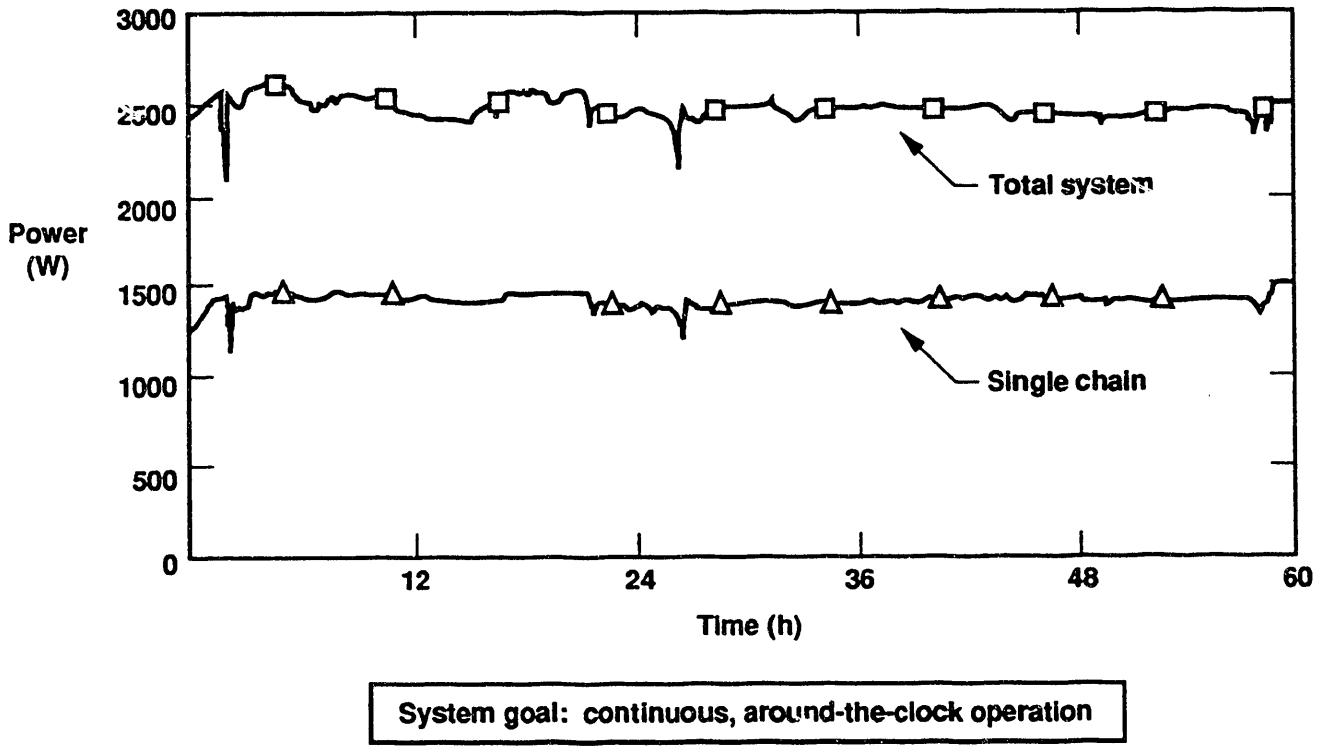

Fig. 14. Dye laser system performance —sustained, high power operation.

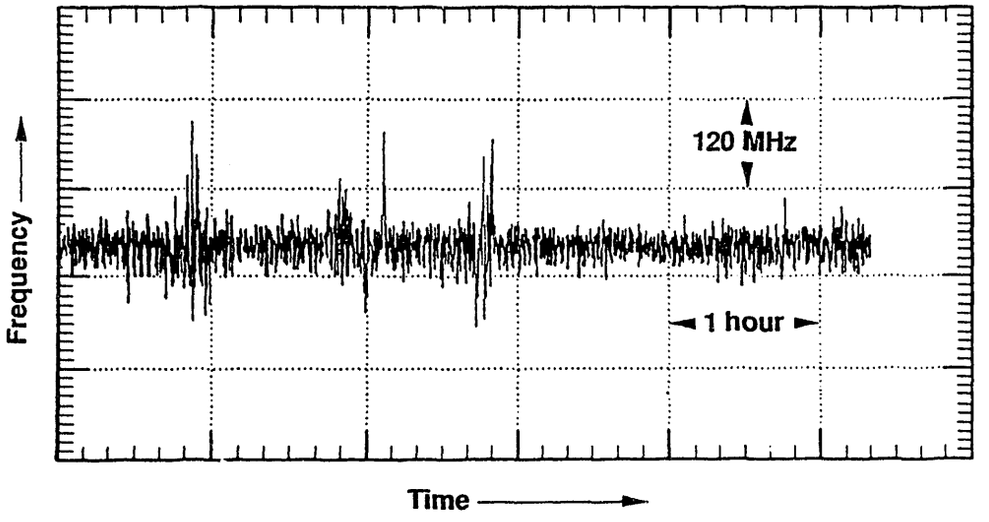

Fig. 15 Long-term frequency stabilization

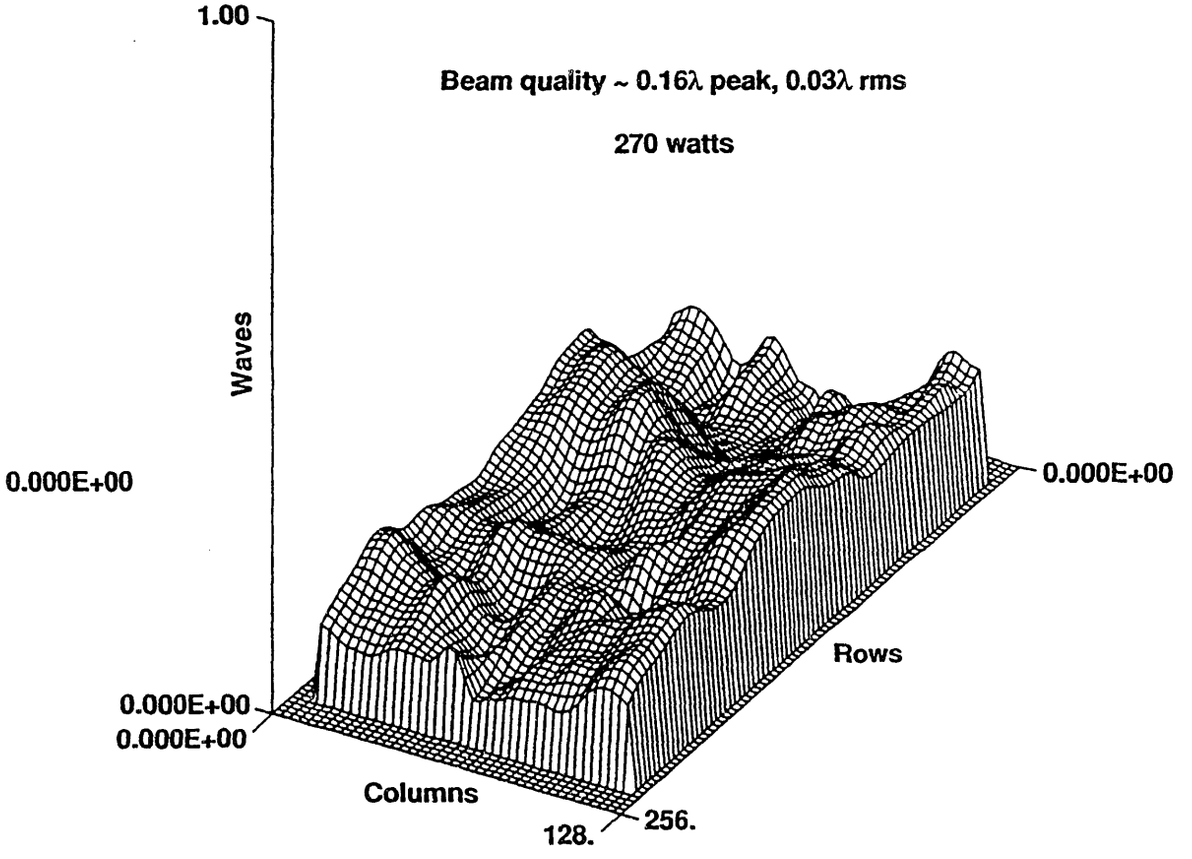

Fig. 16 LDF high power dye laser chain—beam quality

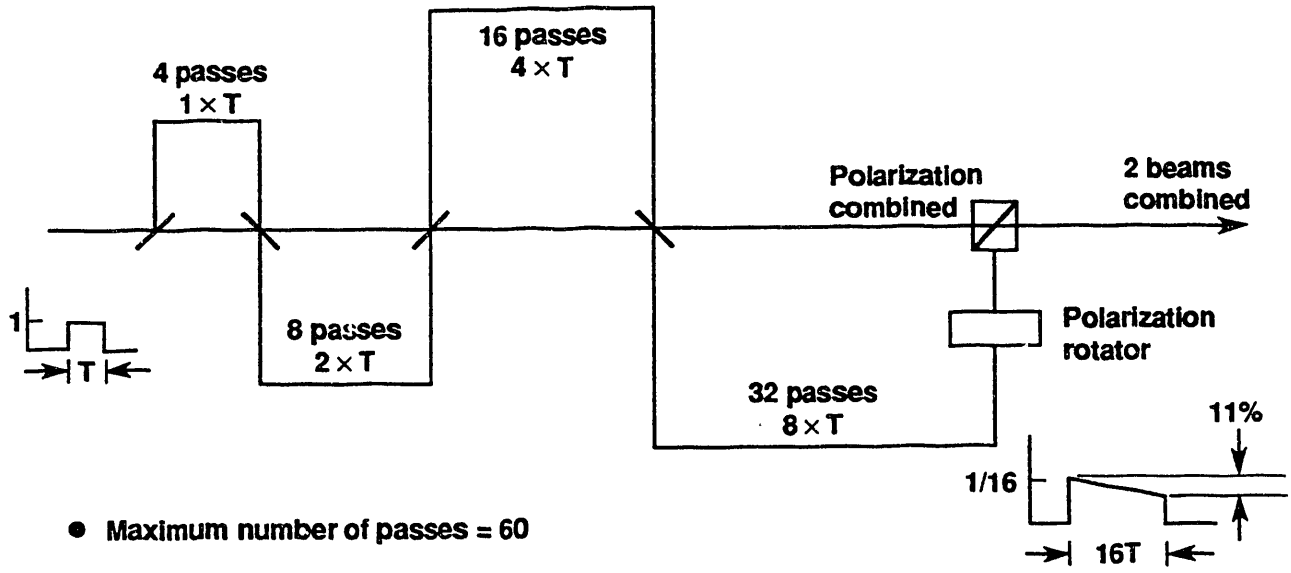

- Maximum number of passes = 60
- Low loss mirrors: $(.998)^{60} = 89\%$
- Relay imaging at each delay is required
- Conceptual design complete, mechanical design and optics layout underway
  - Design review by 9-30-91

Fig. 17. Pulse stretcher topology gives flat top profile with no long tails.

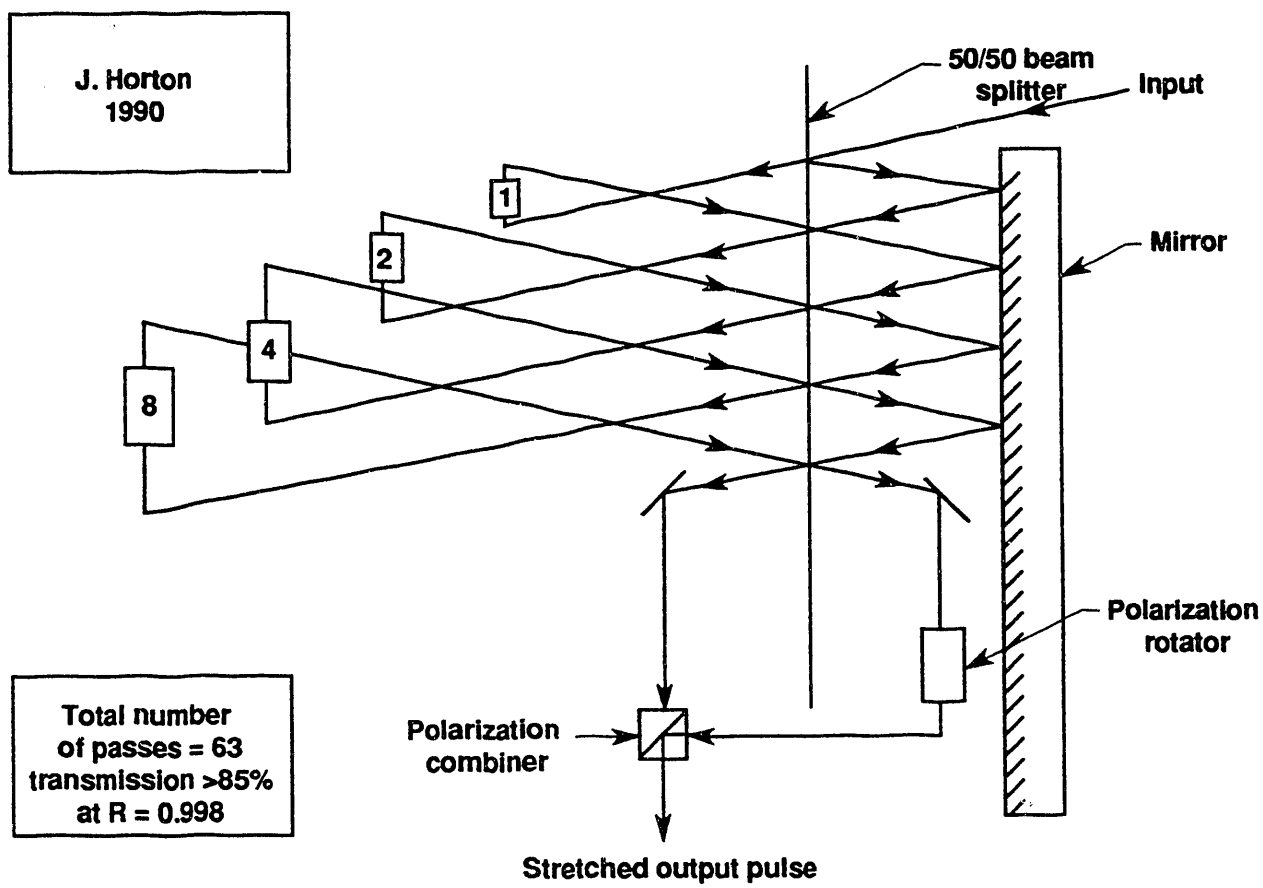

Fig. 18. Pulse stretcher optical design.

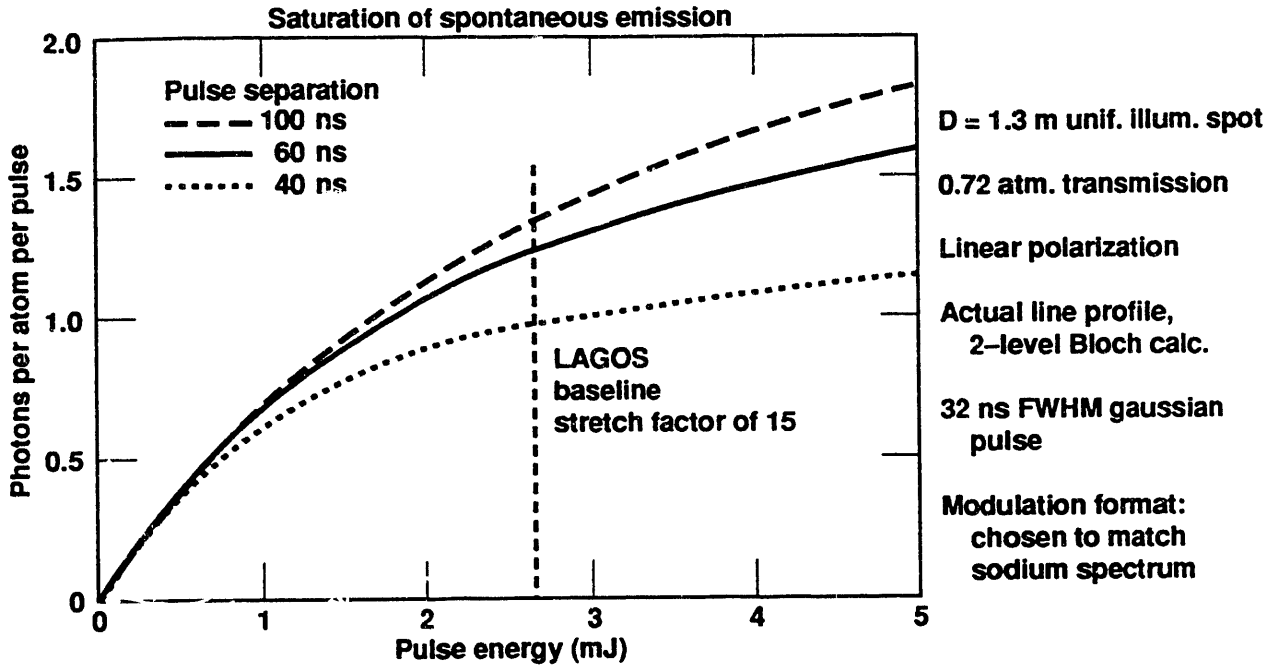

Fig. 19 For our pulse conditions, separation of 60 ns gives ≃ 90% of fully separated result

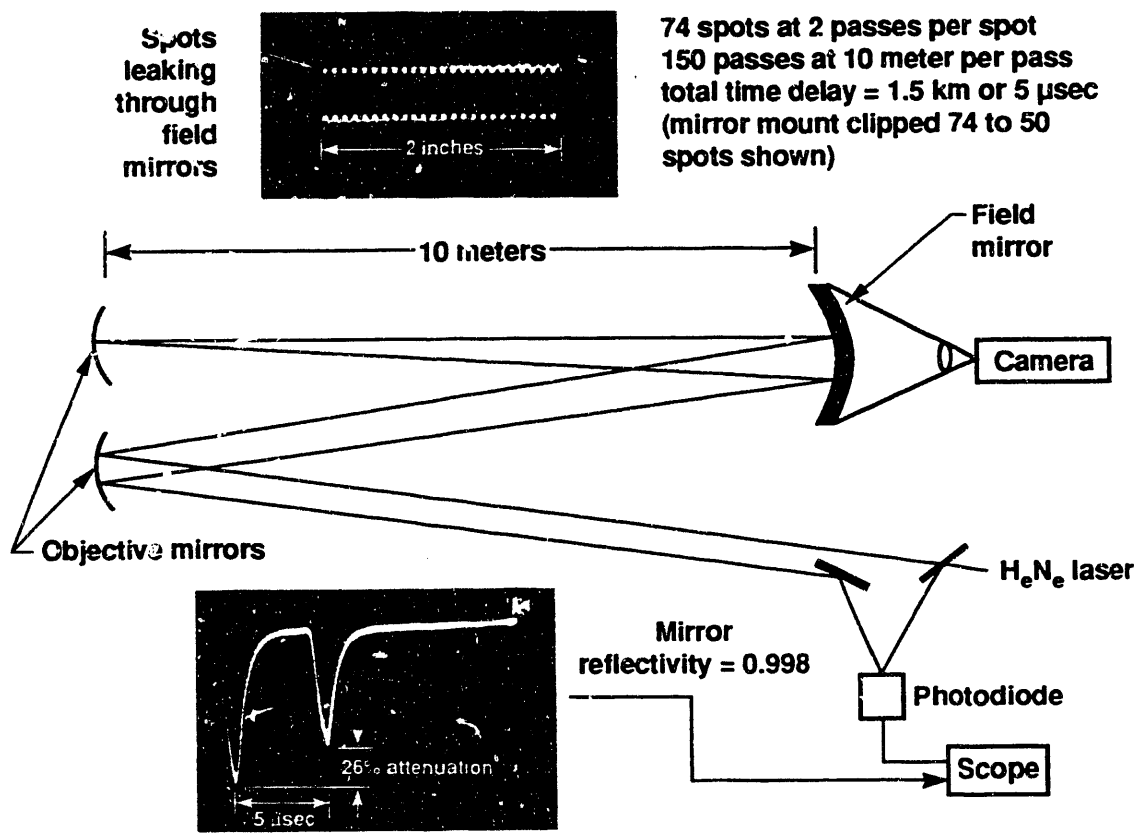

Fig. 20 Long path propagation experiment

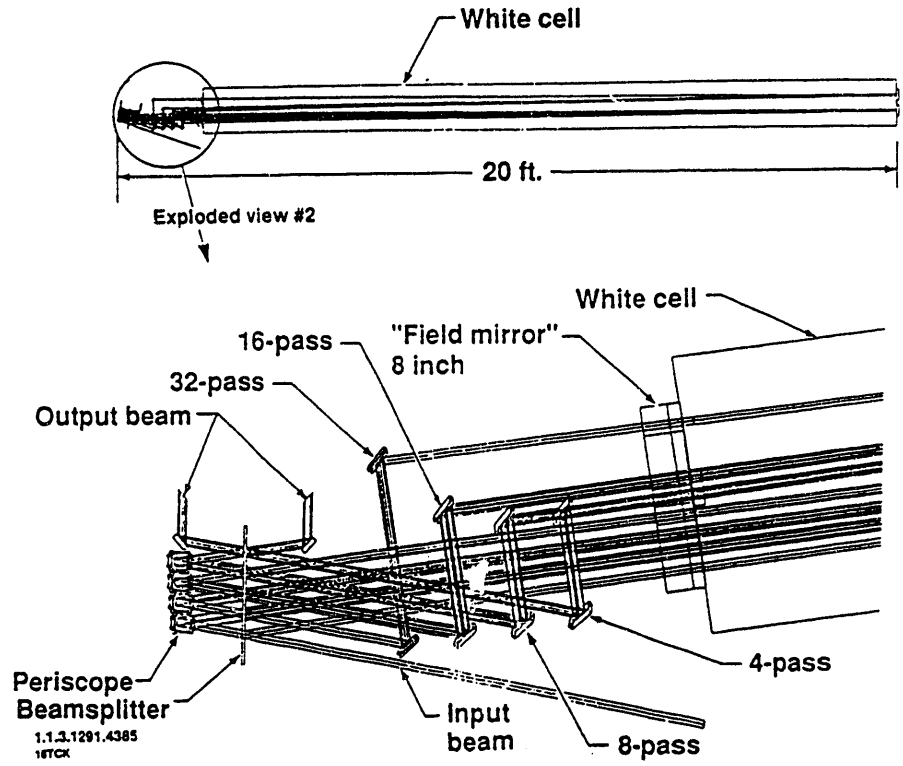

Figure 21. Compact white cell.

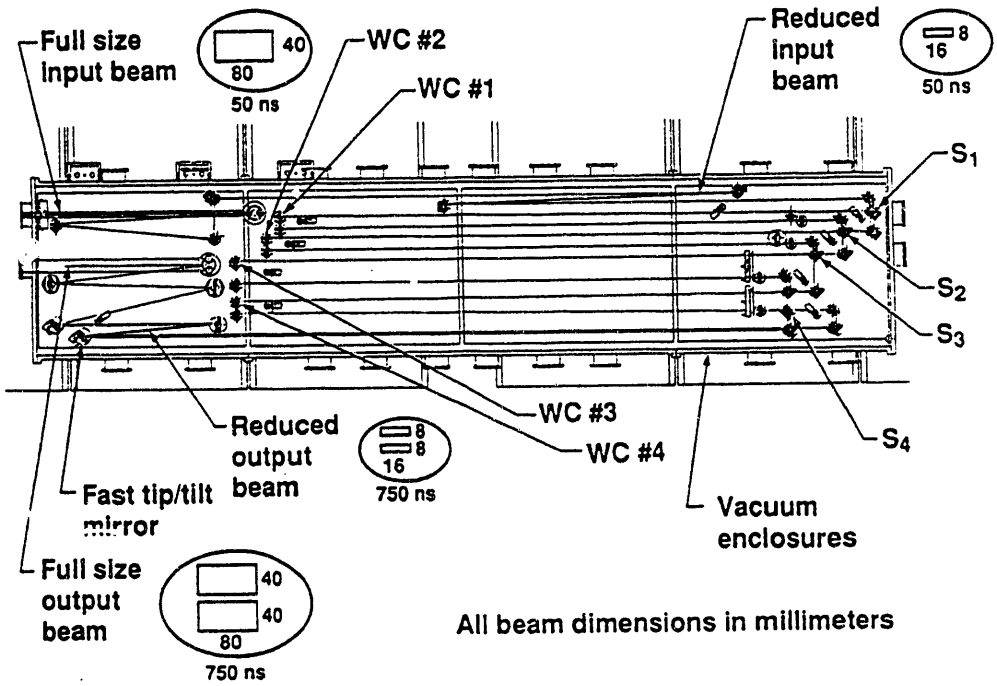

Figure 22. Multiple white cell configuration.

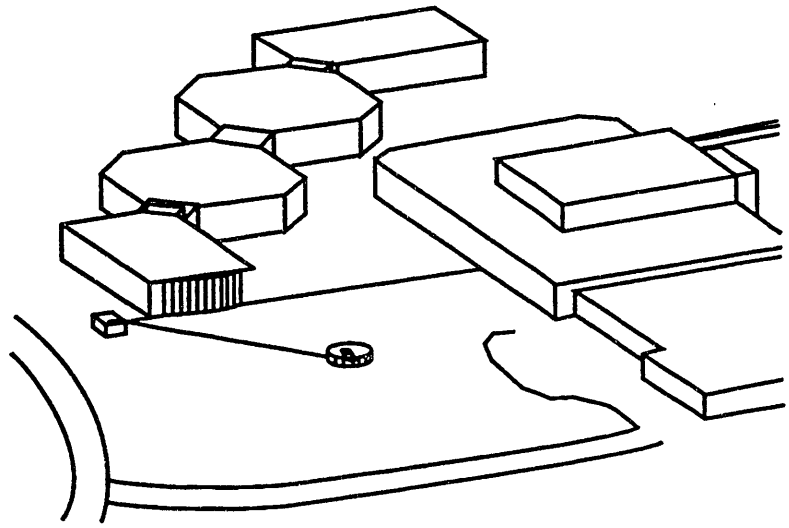

Fig. 23 Far site and South Vault areas

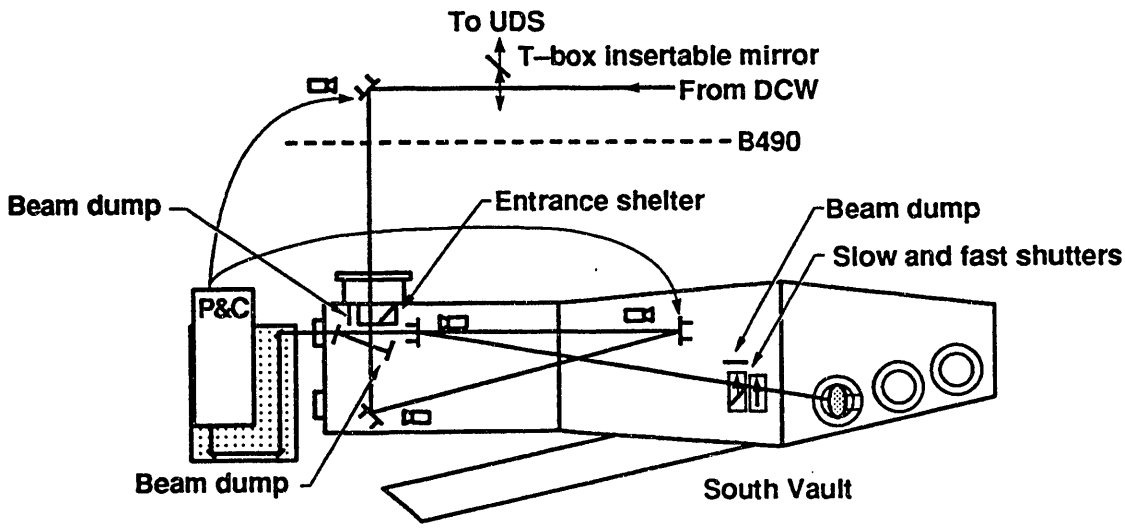

Fig. 24 Optics and alignment controls to be installed in South Vault vacuum box by 9/30/91

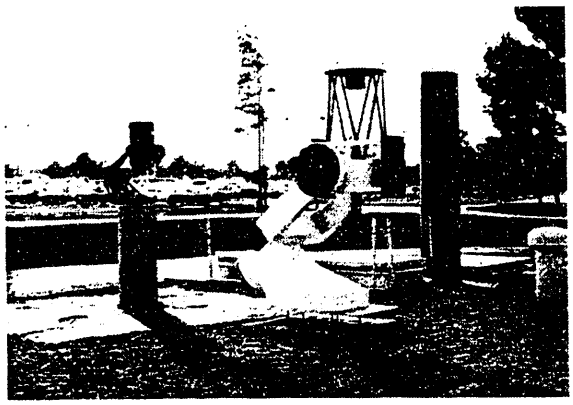

Fig. 25

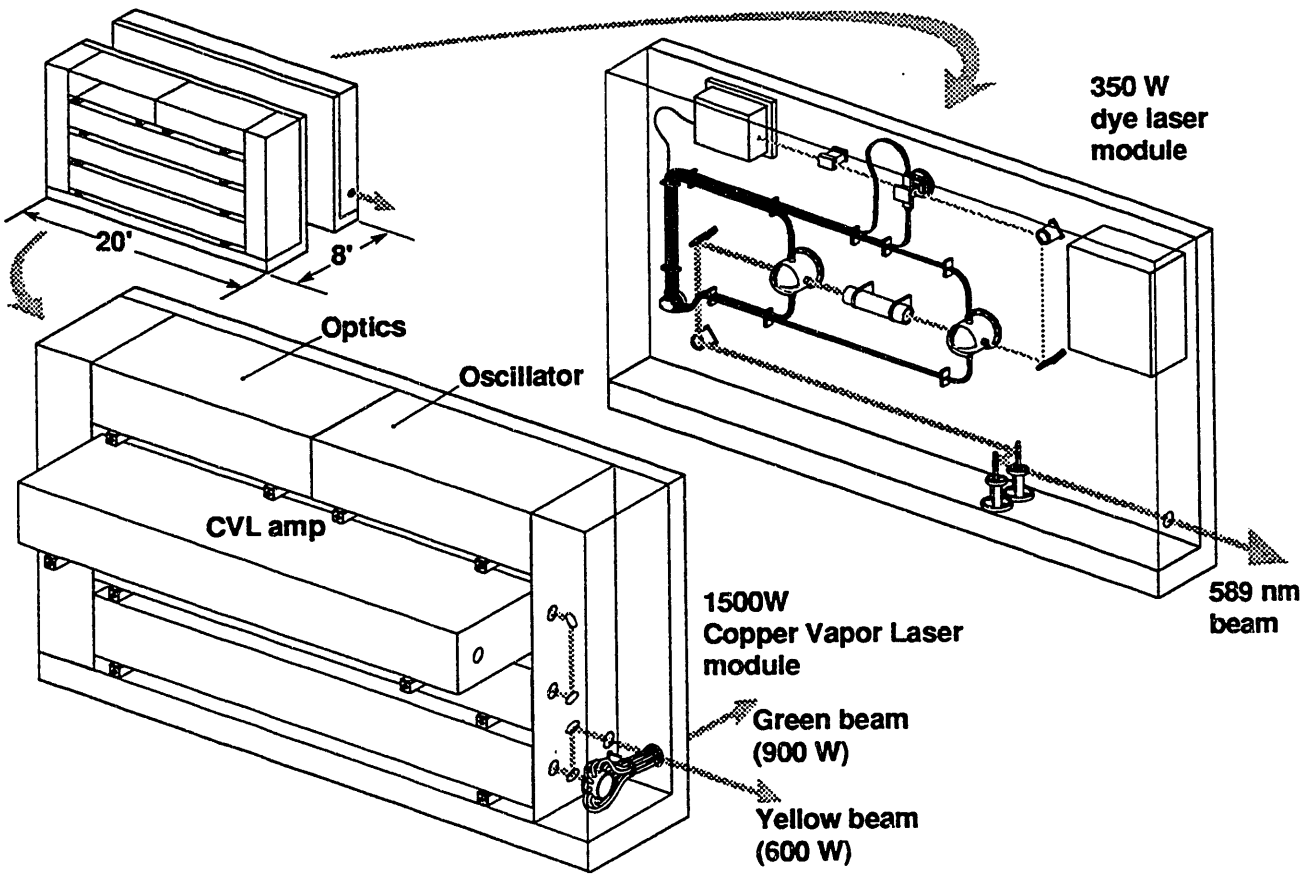

Fig. 26 Lidar laser source module

III.

Sodium Guide Star Adaptive Optics System for Astronomical Imaging in the Visible and Near-Infrared

by

D. T. Gavel, J. R. Morris, and R. G. Vernon

Sodium Guide Star Adaptive Optics System for Astronomical Imaging in the Visible and Near-Infrared *

D. T. Gavel and J. R. Morris, Lawrence Livermore National Laboratory,
Livermore, California
R. G. Vernon, Science Applications International Corporation,
Palm Beach Gardens, Florida

Presented at the DOD/NSF Laser Guide Star Adaptive Optics Workshop
Phillips Laboratory, 10-12 March, 1992

Abstract

We are building an adaptive-optic telescope system that is based on the use of an artificial guide star created by laser-induced fluorescence of the sodium mesospheric layer. This paper discusses the system design for mid-visible to near-infrared compensation of a one meter telescope at Livermore and near-infrared compensation of the ten meter Keck telescope at Mauna Kea.

We calculate the expected Strehl ratio and resolution for a 69 channel deformable mirror system and also for a possible 241 channel system upgrade. With the 69 actuator system we expect near diffraction limited resolution, about 0.2 arcsec, with a Strehl ratio of about 0.5 at λ=0.8 μm on the 1m telescope, and resolution of about 0.05 arcsec with a Strehl ratio of about 0.5 at λ=2.0 μm on the 10m telescope. Resolution will be limited by the performance of the tip/tilt correction loop, which uses an off-axis natural guide star as a reference. The effects which degrade tip/tilt correction are described in a companion paper.

At Livermore, our design uses an existing high power (1 kW) laser source, which is expected to provide an approximately 6'th magnitude artificial guide star. This strong beacon signal allows a short integration time in the wavefront sensor so that temporal changes in the atmospheric turbulence can be tracked accurately. For Mauna Kea, we explore how the system to be built for the Livermore site would perform in the infrared, assuming a 100 W laser source.

1. Introduction

Adaptive optic systems have shown great promise for improving astronomical seeing beyond the limits imposed by atmospheric turbulence. Although efficient collectors of light, the larger aperture telescopes are not able to resolve objects any better than those with an aperture of approximately r_0, the characteristic size of wavefront phase variations. For excellent sites under the best seeing conditions, r_0 is about 20 cm, therefore, the best telescopes in the world resolve no better than a good amateur astronomer's 8-inch telescope.

Adaptive optics technology provides a means of optically correcting for distortions introduced by the atmosphere over a small field of view called the isoplanatic angle, roughly 2-10 arcseconds, depending on the seeing conditions. Resolution can improve dramatically, for example the Keck ten meter telescope which currently has a resolving power of about 1/2 arcsecond in the mid-visible (0.5 μm) could in principal have 0.01 arcsecond resolution with a suitable adaptive optics system installed. Encouraging results have been demonstrated with adaptive optics systems at the Canada-France-Hawaii telescope [1,2], the National Solar Observatory, [3], the Starfire Optical Range [4,5], Maui AMOS facility by Lincoln Laboratory experimenters [6], and at the Observatoire de Haute-Provence (CNRS) in France [7,8]. Additional implementations of adaptive optics systems are planned for the European Southern Observatory [9] and the National Optical

* Work performed under the auspices of the U. S. Department of Energy by the Lawrence Livermore National Laboratory under contract number W-7405-eng-48

Astronomy Observatory [10].

Adaptive optic systems require a point reference source of light in order to measure and correct wavefront distortions. Point reference sources are provided by the stars themselves, but since the angle over which corrections are valid (the isoplanatic angle) is small, the density of bright enough reference stars is not sufficient for full sky coverage. The solution is to "create" a star, wherever we want it in the sky, with a laser illuminator. This paper, and the work at Lawrence Livermore in general, is focused on the sodium beacon approach, that is, laser light tuned to the sodium D_2 line (589 nm) is used to fluoresce a layer of sodium atoms present in the mesosphere at an altitude of 90km [11,12].

2. Guide Star Light

The AVLIS laser at Lawrence Livermore National Laboratory is a copper vapor pumped dye laser that is an ideal high power illumination source for laser guide star use. With only minor retuning, this laser will generate 1000 W at the Sodium D_2 line. Although the AVLIS laser is physically much too large and expensive to be duplicated at a good astronomical site, it allows us to experiment at a local site with plenty of beacon signal. We can then explore the design parameter space at the high end of the laser power range and, for example, by deliberately reducing the signal, determine practical minimum laser power levels for remote sites.

The nominal pulse duration of the AVLIS laser is about 40 ns and the repetition rate is 26 kHz. At 38 mJ per pulse, 1000 W average power is delivered. Unfortunately, the short duty cycle is problematic. The projected beam from an $r_0 \approx 5$ cm aperture will create a roughly 1 meter diameter spot at the sodium layer. The unstretched pulse would therefore illuminate the sodium with 68 W/cm^2 irradiance. However, irradiance levels above about 5 W/cm^2 will not generate additional return signal because the entire population of sodium atoms within the laser beam is too quickly placed in the excited state [11]. In order to take maximum advantage of the 1000 W of power available, the laser pulse will need to be stretched, that is, increased in width and reduced in amplitude, by a factor of about 15. This will be accomplished by a White cell arrangement.

The sodium light return flux density F (photons per m^2 per pulse) is

$$F = \int\int R_{At}(I(x,t))N_{Na}[\frac{T_a}{4\pi z_{Na}^2}]d^2x \tag{1}$$

where N_{na} is the column density of the mesospheric sodium layer, $R_{At}(I(x,t))$ is the spontaneous emission per atom per pump laser pulse with $I(x,t)$ the pump laser irradiance at the sodium layer, z_{Na} is the propagation distance from the ground to the sodium layer, and T_a is the one-way atmospheric transmission factor. The integral folds together the atomic response per atom per pulse and the atomic density to obtain the total photons emitted per pulse assuming linearly polarized light.

At low power, below the effect of saturation, the photons per atom per pulse can be approximated by

$$R_{At}(I(x,t)) = \frac{I(x,t)\sigma_t}{h\nu} = \frac{E\sigma_t T_a}{h\nu\nu_l A_b} \tag{2}$$

where E is the average laser power, ν_l is the repetition rate of the laser, σ_t is the effective cross section of the sodium atoms, h is Plank's constant, ν is the frequency of the sodium D_2 line, and A_b is the area of the illuminating beam at the sodium layer.

Table 1 shows nominal parameters for the Livermore site. Using equation (2) we calculate 34 photons per atom per (stretched) pulse. We also calculated R_{At} numerically using an atmospheric propagation code and 6-level optical Bloch equations to model the sodium atom. The results are shown in Figure 1. At $E = 1000W$ the computed return is about 14 photons per atom per pulse, quite a bit lower than predicted by (2) because of nonlinear saturation effects.

Table 1. Nominal parameters for computing beacon signal strength.

E	1000 W
ν_l	26 kHz
A_b	1 m^2
σ_t	4×10^{-16} m^2
T_a	0.6
N_{Na}	5×10^{13} atoms/m^2
z_{Na}	90 km

The AVLIS laser should be adequate to produce a roughly 6'th magnitude guide star, which, as can be seen in the analysis below, is more than sufficient to drive the adaptive optics system.

3. System Design

a. Optics

A schematic of the optical layout is shown in Figure 2. Light from the 1-meter primary pupil is relayed to a deformable mirror, located at the conjugate of the pupil plane. Both the natural starlight and light from the sodium beacon are reflected off of this mirror. After that, the beacon light is separated using a dichroic beam splitter. Along the path of the beacon light, the pupil is reimaged at the entrance to a wavefront sensor. A 10 arcsecond field stop located at the focal plane of the transfer optics will keep most of the Rayleigh scattered sodium light out of the wavefront sensor.

In our system we plan to use a Hartmann type sensor. This sensor consists of an array of lenslets which focus small subapertures of the beam onto portions of a CCD array. The motions of the Hartmann spots indicate local gradients of the beacon phase in the pupil plane. This information is used to drive the actuators in the deformable mirror so as to correct the beacon wavefront and, along with it, the incoming astronomical starlight. After going through the dichroic filter, the natural starlight is split and focused onto two additional CCD cameras, one to form long-integration-time scientific images of faint objects, and the other to be used as a star tracking sensor.

b. Error Analysis

To achieve near diffraction-limited performance, wavefront phase variations must be reduced to a fraction of a wave rms over the aperture. As fluctuations are reduced, more of the light from a point source is focused into a diffraction limited "core," while some of light still remains in a "halo" of size $1.22\lambda/r_0$ around the core. Earlier analysis has shown that even with a Strehl ratio as low as 0.3 (corresponding to an rms wavefront error of $\lambda/6$) a diffraction-limited core becomes evident.

The Strehl ratio (normalized antenna gain) is defined as the on-axis ratio of the optical system's point spread function to that of the diffraction limit. Here the "system" includes both the atmosphere and the corrections made by the adaptive optics. For small σ_ϕ, Strehl ratio is approximated by

$$S = e^{-\sigma_\phi^2} \tag{3}$$

where σ_ϕ is the wavefront correction rms residual.

Wavefront correction is accomplished in two stages, overall tip-tilt compensation and correction of the higher order modes. In the first part of the analysis we consider only the higher order modes. At the end of this section we return to the analysis of the tip-tilt loop.

The wavefront error remaining after adaptive optic correction (referenced to gross tip and tilt) has three contributors: 1) wavefront measurement error, 2) wavefront fitting error, and 3) servo following error. The

error in measuring the wavefront is a result of the signal-to-noise ratio attainable with a fixed amount of beacon signal and unavoidable noise in the detector. Determining the centroid of the Hartmann spot is subject to both photon shot noise and the thermal and pattern noise of the CCD. This resulting wavefront measurement error is given by [13]

$$\sigma_{\phi_{SNR}} = \frac{\pi[(\frac{3}{16})^2 + (\frac{\varphi d}{8\lambda_S})^2]^{1/2}}{SNR}(\frac{f_c}{f_s})^{1/2}(\frac{\lambda_S}{\lambda_I}), \tag{4}$$

where φ is the size of the sodium guide star as viewed from the ground, in radians, d is the subaperture size, λ_S is the wavelength of the guide star light, λ_I is the wavelength of the imaged light, f_c is the bandwidth of the control loop, and f_s is the wavefront sample rate, that is, the frame rate of the CCD. The formula contains the factor $(f_c/f_s)^{1/2}$ to account for the fact that the closed loop control loop acts as low pass filter on the measurement noise. It also contains the ratio of wavelengths factor to account for the fact that phase variance is less sensitive to the wavefront gradient at longer observation wavelengths.

The signal-to-noise ratio, SNR, is given by

$$SNR = \frac{N}{\sqrt{N + \sigma^2_{\text{readout}} + \sigma^2_{\text{background}}}}, \tag{5}$$

where N is the number of signal photons per subaperture per frame:

$$N = \eta\frac{\pi F d^2 \nu_l}{4 f_s}, \tag{6}$$

where η is the efficiency of the CCD and optical system, F is the return photon flux density per pulse given by equation (1), ν_l is the pulse repetition rate, d is the subaperture size, and f_s is the CCD frame rate.

Anisoplanatism is also an important source of measurement error that has received serious attention [14–19]. Wavefront information provided by the guide star is valid only over a small field of view. Outside this small isoplanatic angle, the light from natural objects travel along different paths through the turbulent atmosphere than does the beacon light. As guide star and astronomical object become separated, wavefront data becomes gradually uncorrelated to the correction that is actually needed to sharpen the image. The isoplanatic angle, θ_0, is given by [17]

$$\theta_0 = \{2.905 k^2 \sec\psi \int_{\text{Path}} C_N^2(z) z^{5/3}\}^{-3/5} \tag{7}$$

where $k = 2\pi/\lambda_I$ is the wavenumber of the imaged light, ψ is the observation angle from zenith, and $C_N^2(z)$ is the index of refraction structure constant [20]. Isoplanatic angle is typically on the order of a few arcseconds. Wavefront measurement error induced by anisoplanatism is

$$\sigma_{\phi_{\text{Anisoplanatism}}} = (\theta/\theta_0)^{5/6} \tag{8}$$

where θ is the separation angle between the guide star and the imaged object. Ordinarily, one would point the sodium guide star directly at the object of interest in order to avoid anisoplanatism, but the problem is not completely solved because 1) location of the sodium guide star spot varies due to atmospheric deflections of the upgoing laser light (therefore it is important to control the high speed tip and tilt of the outgoing beam to keep the spot steady with respect to the background stars), 2) some astronomical objects extend over more than one isoplanatic angle, and 3) a geometrical problem occurs with larger apertures: if the aperture subtends more than the isoplanatic angle of the spherical guide star wavefront, even though the guide star is centered, distortions due to path differences become evident. This latter problem is called focal anisoplanatism. With a 1-meter telescope and the guide star at 90 km, the subtended angle is 10 microradians, roughly θ_0, so it is not a major problem. Larger telescopes require additional guide stars,

about one per subtended θ_0. We will deal with the issue later, when we consider an adaptive optic design for the Keck 10-meter telescope.

Wavefront fitting error is determined by the type of phase correction mirror used and its degrees of freedom. Our design uses a continuous-face-sheet deformable mirror, mostly because this kind of mirror is available to us at relatively low cost and it also avoids the 2π phasing difficulties associated with a flat segmented type. The deformable mirror face has a characteristic deformation in response to the displacement of a given actuator which, for the most part, is local to the zone around the actuator. The response function is designed to roughly approximate 2-dimensional sinc function with zero crossings near the adjacent actuator location, thus it acts as a spatial low pass filter to the delta-function actuator displacements [21]. The ideal actuator spacing is r_0 (as seen at the pupil plane). In our case, with a 1-meter primary mirror aperture and the available 69-actuator deformable mirror, the subapertures are spaced about 11 cm apart. It will be a rare night in the Livermore valley when r_0 (at 589 nm) is 11 cm, however, the spacing is quite appropriate for imaging in the near infrared, where r_0 is larger. We can also expect to get reasonable results for imaging in the visible, as will be justified below.

Deformable mirror fitting error is given by

$$\sigma_{\phi_{\mathrm{DMFit}}} = \mu^{1/2}(d/r_0)^{5/6} \tag{9}$$

where μ is a parameter that depends on the mirror response function. $\mu = 0.27$ has been measured experimentally on mirrors similar to the one we plan to use. Like θ_0, r_0 is a turbulence dependent parameter, precisely defined as

$$r_0 = \{0.423k^2 \sec\psi \int_{Path} C_N^2(z)dz\}^{-3/5} \tag{10}$$

Control servo error is caused by the fact that wavefront corrections can only be made at temporal frequencies as high as the bandwidth of the control loop. Greenwood [22,23] has calculate the power spectrum of turbulence and the errors associated with finite control bandwidth. For $(D/r_0) \gg 0.74$ (which is our case) the characteristic frequency of phase variations is given by

$$f_g = \{0.102k^2 \int_{Path} C_N^2(z)v^{5/3}(z)dz\}^{3/5}, \tag{11}$$

where $v(z)$ is the velocity of the wind at altitude z. The wavefront fitting error due to servo lag is then given by

$$\sigma_{\phi_{ServoLag}} = (f_g/f_c)^{5/6} \tag{12}$$

where f_c, the controller bandwidth, is defined as follows. We consider a type 1 servo, where the mirror actuator drive signal is proportional to the time integral of the phase error. The closed loop system acts as a low pass filter on wavefront error:

$$H(f; f_c) = (1 + if/f_c)^{-1} \tag{13}$$

where f is the temporal frequency in Hertz and f_c is the proportionality constant multiplying the integrated phase error. (units: radians/radians-second=Hertz). From (11), f_c is also -3 db point of the transfer function $H(f; f_c)$, hence it is an appropriate definition for controller bandwidth.

It is important to correct the incoming light for the gross tip and tilt deviations caused by the atmosphere, otherwise, the Strehl improvement accomplished by the higher order wavefront correction will be lost as the jitter will simply smear the diffraction limited core over an area equal to the beam wander. Overall tip and tilt introduced by the atmosphere is[24]

$$\sigma_\alpha = 0.6(\frac{\lambda}{D})(\frac{D}{r_0})^{5/6} \tag{14}$$

radians rms. With $D/r_0 = 20$ (typical for the Livermore site), the $\pm 1\sigma$ beam wander is 17 times the full-width-half-maximum (FWHM) of the diffraction-limited core. For $D/r_0 = 50$ (good seeing at Mauna Kea), the beam wander is 36 times diffraction limit. Therefore, reducing overall tip and tilt by a factor of at least 20 (40 at Mauna Kea) is required if we wish to attain near-diffraction limited resolution.

Performance of the tip-tilt loop is subject to the same sorts of errors that influence the wavefront correction system: measurement error, fitting error, and control lag error. We will assume that the tip-tilt reference guide star is a point source ($\varphi = 0$), in which case the sensor accuracy is given by

$$\sigma_{\alpha_{SNR}} = \frac{3\pi}{16}\frac{1}{SNR}\left(\frac{f_{c_{t/t}}}{f_{s_{t/t}}}\right)^{1/2}\left(\frac{\bar{\lambda}}{D}\right), \tag{15}$$

where SNR is the signal-to-noise ratio as defined earlier, $f_{c_{t/t}}$ is the tip-tilt controller bandwidth, $f_{s_{t/t}}$ is the sample rate of the tip-tilt detector, D is the aperture diameter of the telescope, and $\bar{\lambda}$ is the mean wavelength of the starlight reaching the detector. The signal level, now limited by the magnitude of the natural guide star, can be approximated [25]

$$N = \frac{1}{2}(4 \times 10^{10})10^{-m/2.5} f_{s_{t/t}} \frac{\pi D^2}{4} S \quad \text{photons} \tag{16}$$

where m is the visible magnitude of the star and S is the Strehl ratio associated with the wavefront correction. The count is proportional to the Strehl ratio because the tip-tilt guide star has been sharpened by the adaptive optics system, and therefore S is the fraction of the light that is in the diffraction-limited core. The factor of 1/2 is due to the beam splitting required to share photons with the scientific instrument. Note that the entire aperture of the telescope is used to collect photons, thus a fainter star can be used for the tip-tilt correction than would be required for wavefront correction.

When the astronomical object of interest is too dim to be used as a tip-tilt reference, a nearby guide star must be selected as a substitute. The separation of the guide star from the object of interest however will introduce ***tilt anisoplanatism*** error [15,16,18]. The geometry of the problem is illustrated in Figure 3. If the beam from the guide star and the beam from the astronomical object do not overlap at altitudes where there is significant atmospheric turbulence, then overall tip-tilt of the two beams will be mostly uncorrelated. The tilt isoplanatic angle is roughly D/z_t where z_t is the altitude of the turbulent layer. For example, if D=1 meter and z_t=1 km, the angle is about 200 arcseconds, which is quite a bit larger than the typical isoplanatic angle for wavefront sensing. Nevertheless, there is only about 1 star of magnitude 17 or brighter per 200 arcsecond^2 region of the sky at the galactic pole [26]. This is a problem since diffraction limited performance (reduction of atmospheric tip-tilt by a factor of 20) will require at least 95% tip-tilt measurement correlation, but a star one isoplanatic angle away provides only about 50% correlation [15].

Another issue arises when the tip-tilt guide star is located outside the *wavefront* isoplanatic angle. The adaptive optic system will not sharpen the image of the tip-tilt guide star with the result that accurate determination of its centroid is more difficult. This error, called ***centroid anisoplanatism*** has been the subject of previous analysis given in [27] and [28].

The tilt and centroid anisoplanatism errors that are introduced when off-axis guide stars are used *will fundamentally limit the achievable resolution of an adaptive optic system.* The companion paper [29] describes the tip-tilt analysis in greater detail.

Bandwidth of the tip-tilt control loop is the next important contributor to tip-tilt compensation error. The temporal power spectrum of the atmospherically induced beam tilt has been calculated by Tyler [30]. A characteristic frequency quantifying the power spectrum roll-off is given as

$$f_t = 0.331 D^{-1/6}\lambda_I^{-1}[\sec\psi \int_{Path} C_N^2(z)V^2(z)dz]^{1/2}, \tag{17}$$

where $V(z)$ is the wind velocity at altitude z. The residual tip-tilt error due to finite controller bandwidth is then given by

$$\sigma_{\alpha_{ServoLag}} = (\frac{f_t}{f_{c_{t/t}}})(\frac{\lambda_I}{D}). \tag{18}$$

where $f_{c_{t/t}}$ is the controller bandwidth (defined in a manner similar to that of the wavefront controller).

We can trade off control bandwidth to get a longer integration time on dimmer, but closer, tip-tilt guide stars, thereby reducing anisoplanatism. The manner in which overall tip-tilt correction system can be optimized for resolution performance is described in more detail in reference [29].

4. Predicted Performance

All of the error sources are summarized in a spread-sheet analysis, where we are able to predict overall Strehl and resolution performance and examine trade-offs in the design parameters.

a. Livermore Site

The error tree is shown in Figure 4 for the Livermore site. Our current plans are to use a 1-meter telescope and a 69-channel deformable mirror in a 100 Hz closed-loop-bandwidth system. We later plan to upgrade to a 241-channel system. The actuators on the mirror are aligned to the lenslets on the Hartmann sensor array, so for the 69-channel system, the subapertures are 11 cm in diameter. In the 241-channel system, the subapertures will be 5.8 cm in diameter, which is more appropriate for visible seeing.

Figure 4a summarizes the 69 subaperture system. Total wavefront Strehl is expected to be 0.5 and residual jitter (with on-axis guiding) will be below 0.2 microradians. The major contributor to wavefront Strehl degradation is fitting error. The 241 subaperture system will improve the wavefront fit as shown in Figure 4b. Even though the 241-channel system has smaller subapertures, there is little degradation in wavefront measurement accuracy since plenty of photons are still available per sample integration time (1 ms).

b. Mauna Kea Site

Once closed-loop operation has been demonstrated at the Livermore site, we envision transporting the 69 subaperture system to the 10-meter Keck Telescope on Mauna Kea, Hawaii. The error tree for the Keck system is shown in Figure 5.

With a 10-meter aperture, the subapertures on this system are 1.1 meters in diameter, thus fitting error is a problem at lower wavelengths, as shown in Figure 6. We feel that $\lambda = 2\mu$m is an ideal imaging wavelength for this system.

Focal anisoplanatism is now an important source of corrected wavefront error, since the 10-meter aperture subtends 100 microradians of the sodium beacon wavefront, which is several times the isoplanatic angle. Multiple guide stars have been proposed in order to cover isoplanatic patch size areas of the aperture [31]. The sodium beacon has a distinct advantage over Rayleigh beacons in the large aperture case because the altitude of the sodium layer, 92km, puts sodium guide stars at a much higher altitude, thus reducing the subtended angle. As a result, fewer guide stars are needed. Wavefront variance due to focus anisoplanatism can be calculated [32]:

$$\begin{aligned}\sigma_{\phi_{FocalAniso}} = 0.707 D^{5/6} k[&\frac{\mu_{5/3}(L)}{L^{5/3}} - 0.877\frac{\mu_2(L)}{L^2} + 0.940\frac{\mu_3(L)}{L^3} \\ &- 2.014\frac{\mu_4(L)}{L^4} + 1.204\frac{\mu_5(L)}{L^5} - 0.322\frac{\mu_6(L)}{L^6}]^{1/2}\end{aligned} \tag{19}$$

where

$$\mu_n = \sec^{n+1}\psi \int_{\text{Path}} C_N^2(z) z^n dz. \tag{20}$$

The analysis in Figure 5 shows that if we image at 2 microns, the Strehl contribution due to focal anisoplanatism is 0.72. Assuming that the focal anisoplanatism error in a multiple guide star system will reduce proportional to one over the square root of the number of guide stars, the Strehl contribution will vary with wavelength according to the curves in Figure 7. Additional spots allow imaging deeper into the visible.

Figure 8 shows Strehl dependence on laser power. A single guide star system would need only 10 W. For multiple guide star adaptive optics and imaging in the visible, a much greater number of deformable mirror degrees of freedom will be needed and on the order of 100 W of laser power will be required.

5. Conclusions

We have described the expected performance of a sodium guide star adaptive optics system at both the Livermore experimental site, and at the Keck 10-meter telescope on Mauna Kea. We have developed an error budget analysis that takes into account the many sources of wavefront distortion and attempts to balance the errors among the various subsystems. We are completing an end-to-end simulation of the system and are preparing for local site experiments early this year.

References

1. McClure, R., Grundmann, W., Rambold, W., Fletcher, J., Richardson, E., and Stilburn, J., *An Image-Stabilization, High-Resolution Camera for the Canada-France-Hawaii Telescope*, **Publications of the Astronomical Society of the Pacific**, 101, 1156–1165, December, 1989.

2. Racine,R., and McClure,R., *An Image Stabilization Experiment at the Canada-France-Hawaii Telescope*, **Publications of the Astronomical Society of the Pacific**, 101, 731–736, August, 1989.

3. Dunn, R., *NSO/SP Adaptive Optics Program*, **SPIE 1271, Adaptive Optics and Optical Structures**, 216–231, 1990.

4. Sandler, D., Barrett, T., Palmer, D., Fugate, R., and Wild, W., *Use of a Neural Network to Control an Adaptive Optics System for an Astronomical Telescope*, **Nature**, 351, May 23, 1991.

5. Fugate, R., Fried, D., Ameer, G., Boeke, B., Browne, S., Roberts, P., Ruane, R., Tyler, G., and Wopat, L., *Measurement of Atmospheric Wavefront Distortion Using Scattered Light from a Laser Guide Star*, **Nature**, 353, September 12, 1991.

6. Primmerman, C., Murphy, D., Page, D., Zollars, B., and Barclay, H., *Compensation of Atmospheric Optical Distortion Using a Synthetic Beacon*, **Nature**, 353, September 12, 1991.

7. Rousset, G., Fontanella, J., Kern, P., Gigan, P., Lena, P., Boyer, C., Jagourel, P., Gaffard, J., and Merkle, F., *First Diffraction-limited Astronomical Images with Adaptive Optics*, **Astronomy and Astrophysics**, 230, L29–L32, 1990.

8. Kern, P., Lena, P., Gigan, P., Rigaut, F., Rousset, G., Fontanella, J-C., Gaffard, J-P., Boyer, C., Jagourel, P., Merkle, F., *Adaptive Optics Prototype System for Infrared Astronomy, I: System Description*, **SPIE 1271, Adaptive Optics and Optical Structures**, 243–250, 1990.

9. Merkle, F., and Hubin, N., *Adaptive Optics for the European Very Large Telescope*, **European South-**

ern Observatory Technical Preprint no.32, and *SPIE 1542*, 1991.

10. Goad, L., Roddier, F., Beckers, J., Eisenhardt, P., *National Optical Astronomy Observatories (NOAO) IR Adaptive Optics Program III: Criteria for the Wavefront Sensor Selection*, SPIE 628, Advanced Technology Optical Telescopes III, 1986.

11. Gardner, C., Welsh, B., and Thompson, L., *Design and Performance Analysis of Adaptive Optical Telescopes Using Laser Guide Stars*, **Proceedings of the IEEE**, 78, 11, 1721–1743, November 1990.

12. Thompson, L., and Gardner, C., *Experiments on Laser Guide Stars at Mauna Kea Observatory for Adaptive Imaging in Astronomy*, **Nature**, 328, 229–231, July 16, 1987.

13. Tyler, G., and Fried, D., *Image-position Error Associated with a Quadrant Detector*, **J. Optical Society of America**, 72, 6, 804–808, June 1982.

14. Fried, D., *Varieties of Isoplanatism*, **SPIE 75, Imaging Throught the Atmosphere**, 20–29, 1976.

15. Valley G., and Wandzura, S., *Spatial Correlation of Phase-expansion Coefficients for Propagation Through Atmospheric Turbulence*, **J. Optical Society of America**, 69, 5, 712–717, May, 1979.

16. Valley, G., *Isoplanatic Degradation of Tilt Correction and Short-term Imaging Systems*, **Applied Optics**, 19, 4, 574–577, February, 1980.

17. Fried, D., *Anisoplanatism in Adaptive Optics*, **J. Optical Society of America**, 72, 1, 52–61, January, 1982.

18. Christian, C., and Racine, R., *Dependence of Seeing Correlation on Image Separation at the CFH Telescope on Mauna Kea*, **Publications of the Astronomical Society of the Pacific**, 97, 1215–1225, December, 1985.

19. Chassat, F., Rousset, G., and Primot, J., *Theoretical and Experimental Evaluation of Isoplanatic Patch Size for Adaptive Optics*, **SPIE 1130, New Technologies for Astronomy**, 1989.

20. Tatarski, V., **Wave Propagation in a Turbulent Medium**, McGraw-Hill Book Company, New York, 1960.

21. Ealey, M., *Continuous Facesheet Low Voltage Deformable Mirrors*, **Optical Engineering**, 29, 10, 1191–1198, October, 1990.

22. Greenwood, D., and Fried, D., *Power Spectra Requirements for Wave-Front-Compensative Systems*, **J. Optical Society of America**, 66, 3, 193–206, March, 1976.

23. Greenwood, D., *Bandwidth Specification for Adaptive Optics Systems*, **J. Optical Society of America**, 67, 3, 390–393, March, 1977.

24. Fried, D., *Statistics of a Geometric Representation of Wavefront Distortion*, **J. Optical Society of America**, 55, 11, 1427–1435, November, 1965.

25. Tyson, R., **Principles of Adaptive Optics**, Academic Press, Inc., San Diego, CA, 1991.

26. Wolfe, W., and Zissis, G., eds., **The Infrared Handbook**, Office of Naval Research, Department of the Navy, Washington, DC, 1978.

27. Yura, H., and Tavis, M., *Centroid Anisoplanatism*, **J. Optical Society of America, A**, 2, 5, 765–773, May, 1985.

28. Tyler, G., *The Impact of Centroid Measurement Upon Pointing Accuracy*, **The Optical Sciences Company Report No. TR-634**, April, 1985.

29. Olivier, S., Max, C., Gavel, D., Brase, J., *Resolution Limits for Ground Based Astronomical Imaging Using Adaptive Optics*, **This Workshop**, March, 1991.

30. Tyler, G., *Bandwidth Considerations for Tracking Through Turbulence*, **The Optical Sciences Company Report No. TR-887**, March, 1988.

31. Welsh, B., and Gardner, C., *Effects of Turbulence-induced Anisoplanatism on the Imaging Performance of Adaptive-astronomical Telescopes Using Laser Guide Stars*, **J. Optical Society of America, A**, 8, 1, 69–80, January 1991.

32. Sasiela, R., Presentation on focal anisoplanatism given at Lincoln Laboratory, December, 1989.

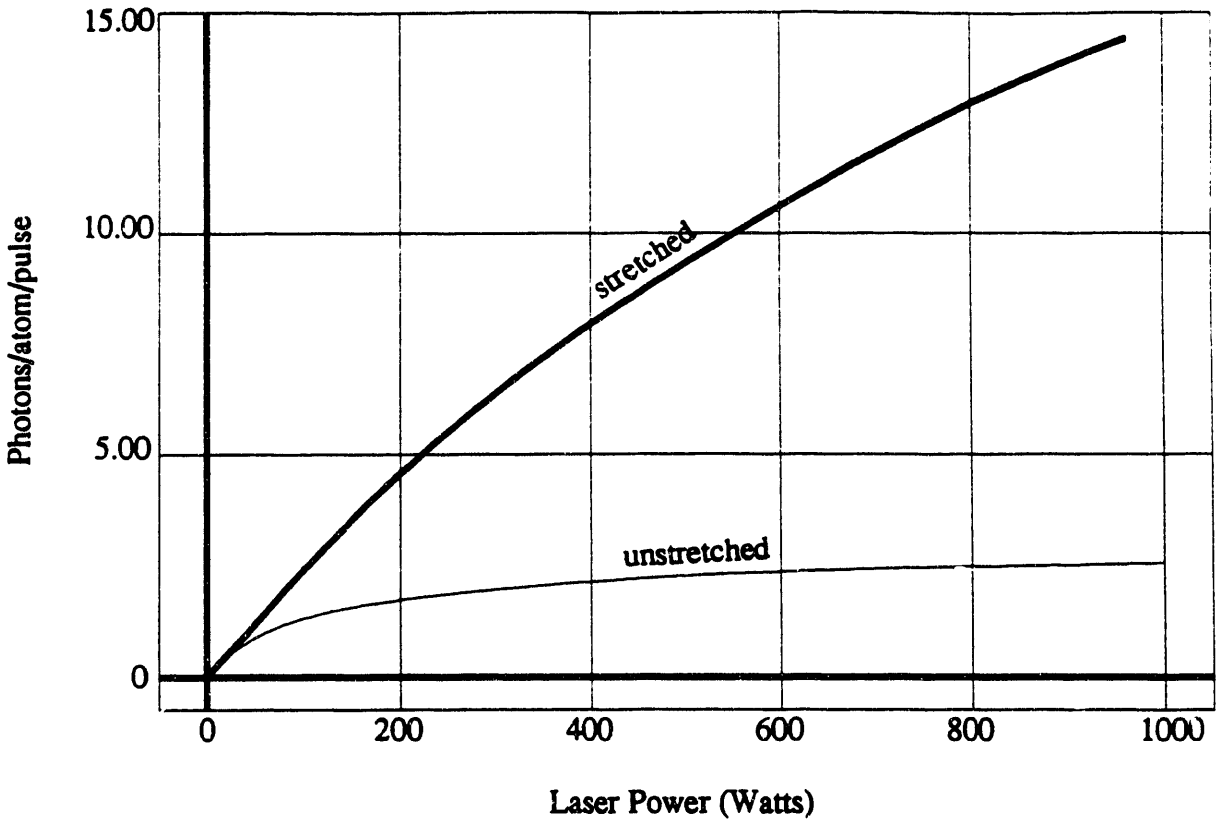

Figure 1 - Sodium beacon return strength as a function of laser power.

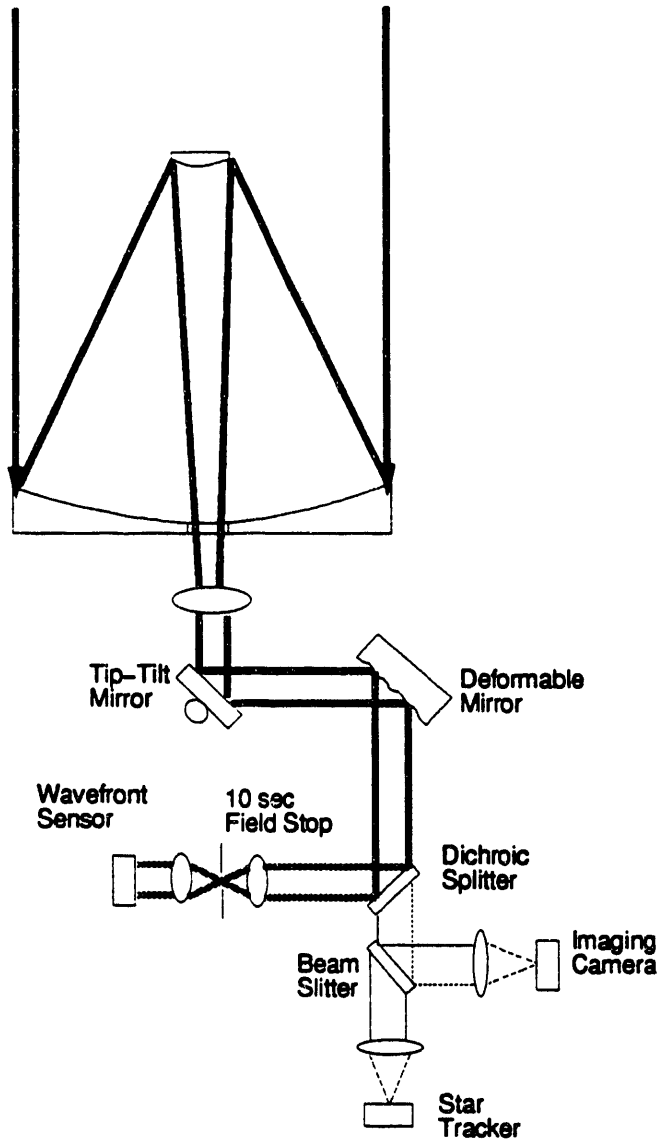

Figure 2 - Laser Guide Star Adaptive Optics Layout.

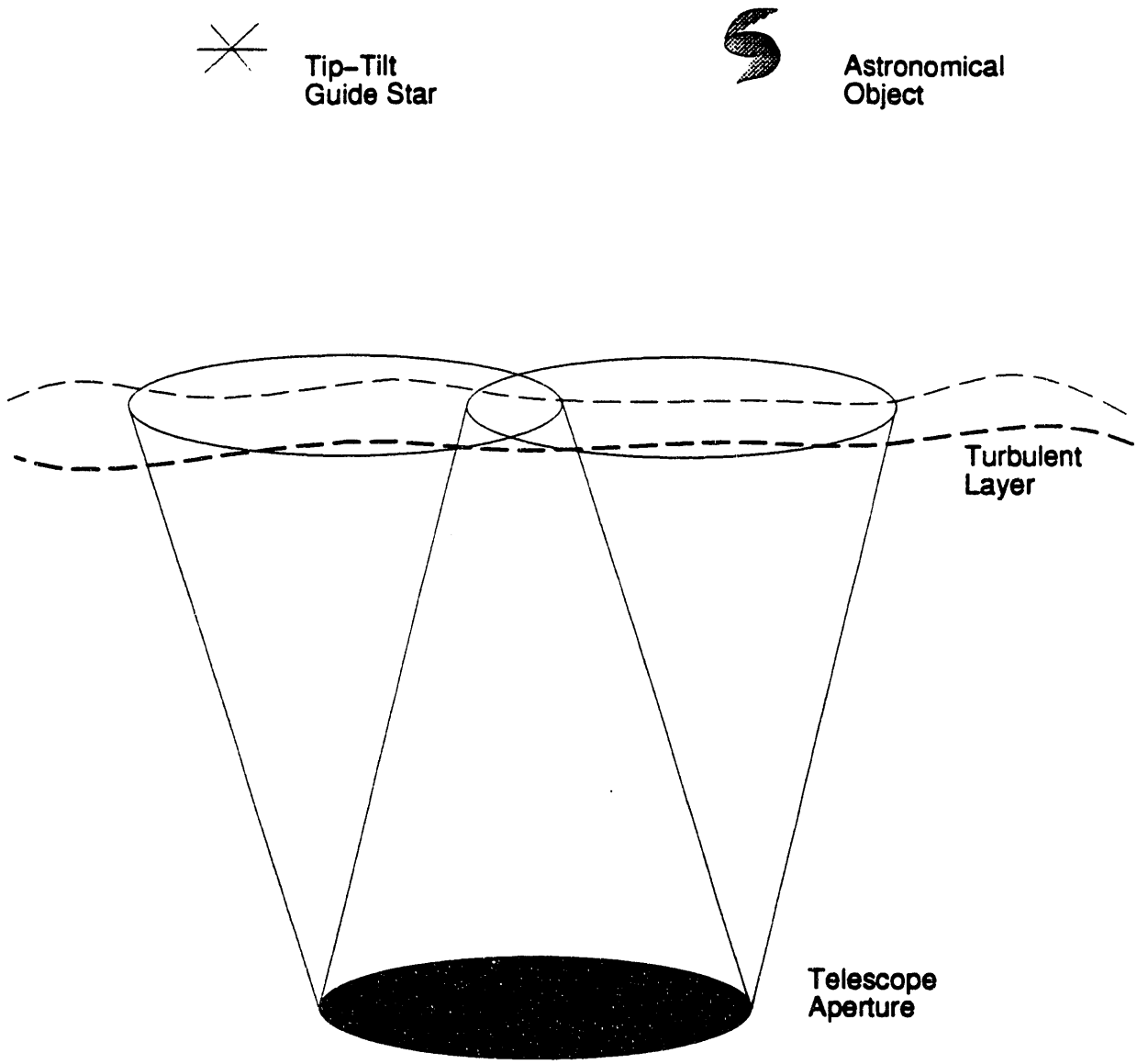

Figure 3 – Geometry of tilt anisoplanatism.

69 Subaperture System - Livermore

Parameters		Derived Parameters		
lambda-gs	5.89E-07	Ni	6.8379E+16	
lambda-astro	8.00E-07	Rat	14	34.8249596
D	1	F	3240.74074	
d	0.111111111	N	25.3270258	
mu	0.27	N-tilt	3.08499525	
eta-wfs	0.031	theta0	1.2304E-05	
eta-tts	0.9	r0	0.08788484	
lgs-sub-angle	1.00E-05	fg	22.7570525	
laser-power	1000	ft	10.125	
Na-cross-sec	4.00E-16			
z-Na	9.00E+04			
c-light	3.00E+08			
h	6.626E-34			
nu	5.09338E+14			
nu-i	26000			
Ta	0.6			
Ab	0.785398163			
col-density	5E+13			
Ar	0.009696274			
Cn2(z)	Hufnagel-Valley	5-7		
V(z)	Bufton Wind			
zenith-angle	0			
fs	1000			
fc	100			
fs-tilt	1000			
fc-tilt	100			
m	16			

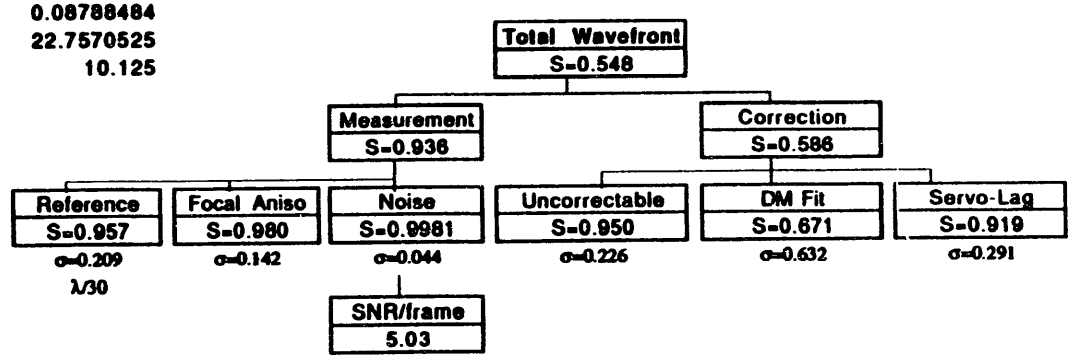

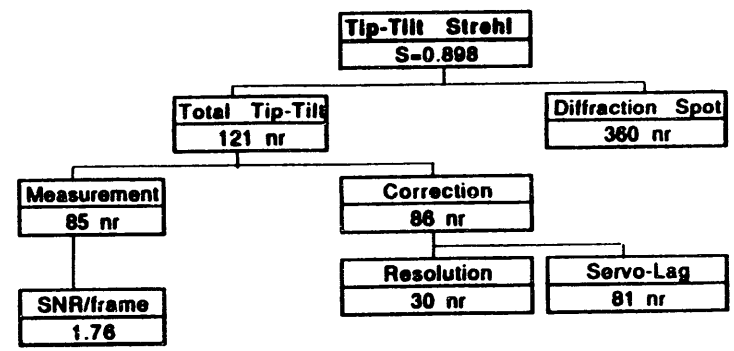

Figure 4a – Error analysis for the Laser Guide Star telescope, Livermore site, 69 subaperture system.

241 Subaperture System - Livermore

Parameters		Derived Parameters		
lambda-gs	5.89E-07	NI	6.8379E+16	
lambda-astro	8.00E-07	Rat	14	34.8249596
D	1	F	4861.11111	
d	0.058823529	N	10.6478673	
mu	0.27	N-tilt	4.00185295	
eta-wfs	0.031	theta0	1.2304E-05	
eta-tts	0.9	r0	0.08788484	
igs-sub-angle	1.00E-05	fg	22.7570525	
laser-power	1000	ft	10	
Na-cross-sec	4.00E-16			
z-Na	9.00E+04			
c-light	3.00E+08			
h	6.626E-34			
nu	5.09338E+14			
nu-I	26000			
Ta	0.6			
Ab	0.785398163			
col-density	5E+13			
Ar	0.002717641			
Cn2(z)	Hufnagel-Valley	5-7		
V(z)	Bufton Wind			
zenith-angle	0			
fs	1000			
fc	100			
fs-tilt	1000			
fc-tilt	100			
m	16			

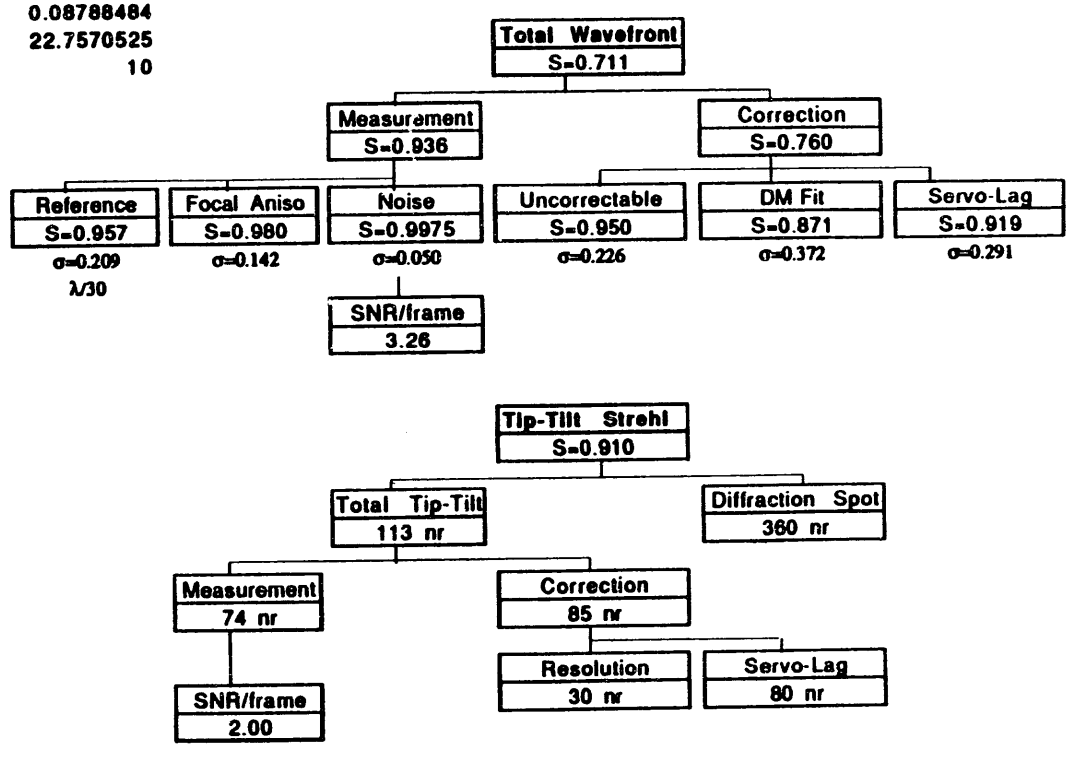

Figure 4b – Error analysis for the Laser Guide Star telescope, Livermore site, 241 subaperture system.

69 Subaperture System - MaunaKea

Parameters	
lambda-gs	5.89E-07
lambda-astro	2.00E-06
D	10
d	1.111111111
mu	0.27
eta-wfs	0.031
eta-tts	0.9
lgs-sub-angle	1.00E-05
laser-power	10
Na-cross-sec	4.00E-16
z-Na	9.00E+04
c-light	3.00E+08
h	6.626E-34
nu	5.09338E+14
nu-l	26000
Ta	0.84
Ab	78.53981634
col-density	5E+13
Ar	0.969627362
Cn2(z)	data
V(z)	data
zenith-angle	0
fs	100
fc	10
fs-tilt	100
fc-tilt	10
m	22

Derived Parameters	
NI	9.573E+14
Rat	0.00487549
F	237.003197
N	1852.22657
N-tilt	6.30801022
theta0	5.5947E-05
r0	0.79170475
fg	5.49447255
ft	0.825

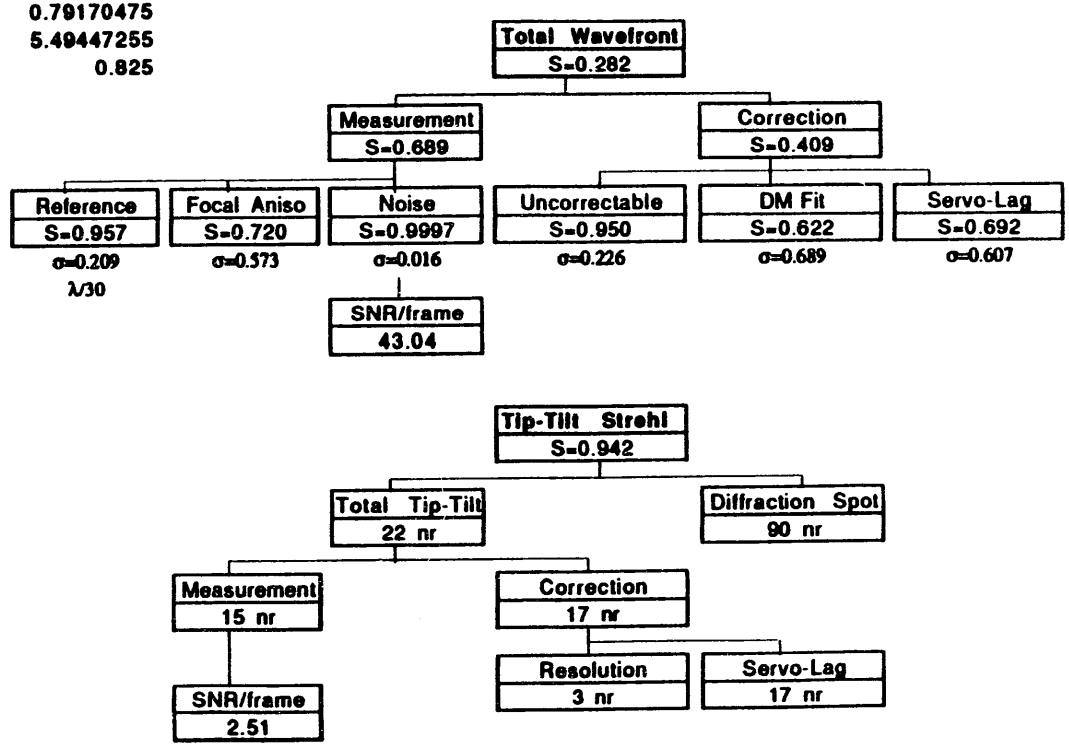

Figure 5 – Error analysis for the Laser Guide Star telescope, Mauna Kea site, 69 subaperture system.

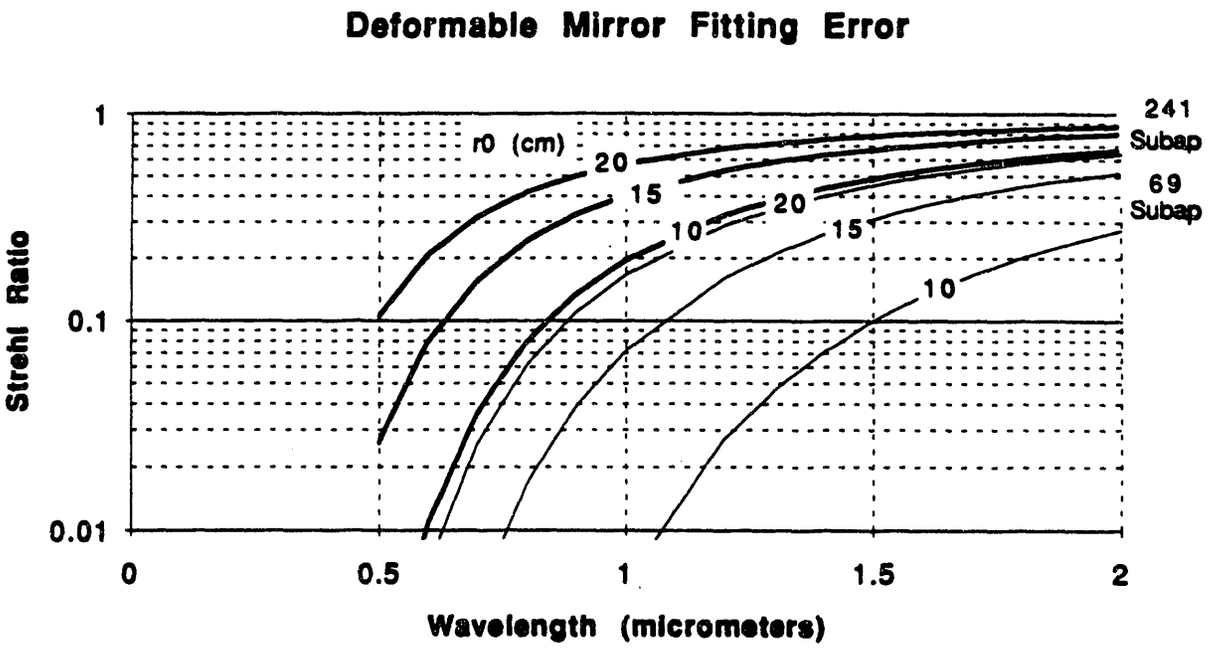

Figure 6 – Wavefront fitting error versus wavelength for various seeing conditions (r_0 at $\lambda = 0.5\mu$m) at Mauna Kea.

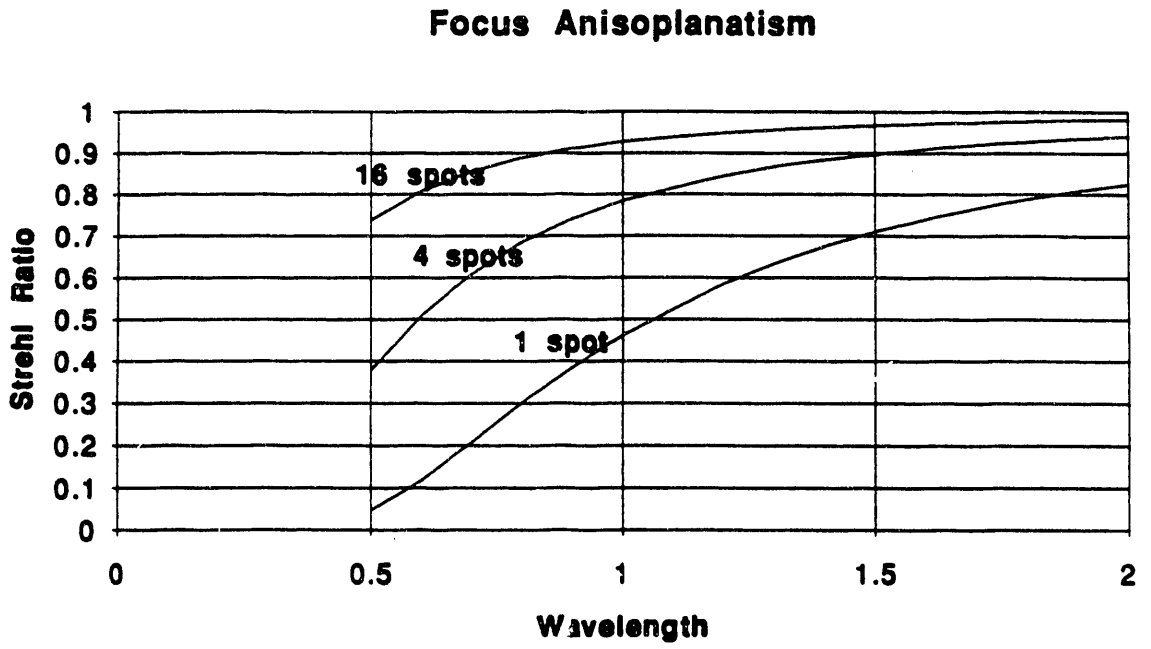

Figure 7 – Focus anisoplanatism versus wavelength and number of guide stars, Mauna Kea site.

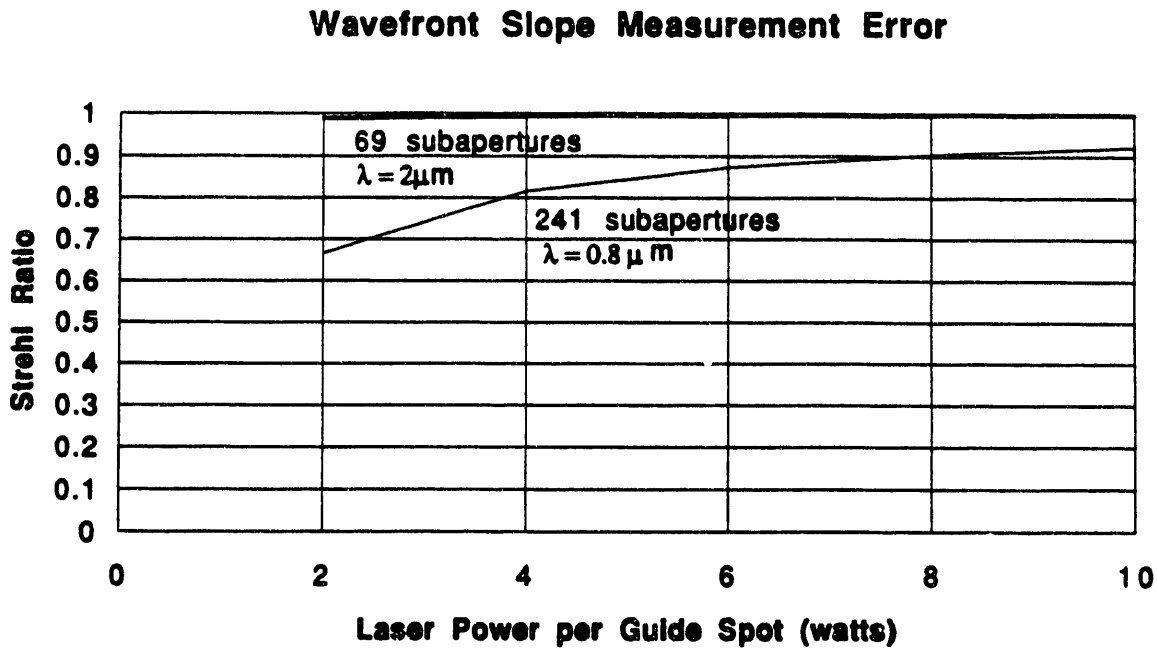

Figure 8 – Wavefront measurement error versus laser power, Mauna Kea site.

IV.

High Frame-Rate, Large Field Wavefront Sensor

by

K. Avicola, J. T. Salmon, J. Brase,
K. Waltjen, R. Presta, and K. S. Balch

High Frame-Rate, Large Field Wavefront Sensor*

K. Avicola, J.T. Salmon, J. Brase, K. Waltjen, R. Presta
Lawrence Livermore National Laboratory

K.S. Balch
Eastman Kodak Company

Abstract

A two-stage intensified 192 x 239 pixel imager developed by Eastman Kodak for motion analysis was used to construct a 1 kHz frame-rate Hartmann wavefront sensor. The sensor uses a monolithic array of lenslets with a focal length that is adjusted by an index fluid between the convex surface and an optical flat. The accuracy of the calculated centroid position, which is related to wavefront measurement accuracy, was obtained as a function of spot power and spot size. The sensor was then dynamically tested at a 1 kHz frame-rate with a 9 x 9 lenslet array and a fast steering mirror, which swept a plane wavefront across the wavefront sensor. An 8 cm diameter subaperture will provide a return signal (589 nm) level of about 1000 photons/ms using the AVLIS 1 kW laser (stretched pulse) as guide star source, which is sufficient to yield a wavefront measurement of better than $\lambda/10$ rms. If an area of 6 x 6 pixels per Hartmann spot were allocated, this wavefront sensor could support a 32 x 32, or 1024, element deformable mirror.

1. Introduction

An overview of the sodium-layer laser guide star experiment at LLNL[1], the laser system to be used[2], and the adaptive optics system design[3] are discussed in other papers at this workshop. The Shack-Hartmann wavefront sensor used in the early phases of this program has a monolithic array of microlenses and a commercially available high frame-rate motion analysis camera developed by Eastman Kodak.[4-6] Initially we planned to use this wavefront sensor only as an on-line diagnostic instrument, but we now anticipate more extensive use of this sensor. It will be used first for atmospheric characterization at the LLNL site using a 0.5 meter telescope and natural stars. Subsequently it will be used as one of several instruments measuring initial laser guide star return signals and as the adaptive optics wavefront sensor in a laboratory closed-loop A-O system with a 69 element DFM, which will be installed on a 1 meter telescope. The complete wavefront sensor, with lenslet array mated to the camera, is described here, but most of the experimental work reported was obtained using a single lens to form the spot. The ability to determine centroids, and hence wavefront tilt, was examined as a function of spot size and power.

* This work was performed under the auspices of the U.S. Department of Energy by Lawrence Livermore National Laboratory under Contract No. W-7405-Eng-48.

2. Wavefront Sensor Description

The design of the wavefront sensor is illustrated in the simplified schematic of Figure 1, for use with the 1/2 meter telescope. The sensor consists of a lenslet array placed in the reimaged pupil plane and a fast framing video camera. Because of the large number (192 x 239) of pixels available with this camera, an area of 10 x 10 pixels for each Hartmann spot was chosen. This allows a local tilt of about 12 arc seconds before the spot would fall on a neighboring spot's pixel area, which is well under the expected atmospherically induced tilts.

The center-to-center spacing of the lenslet array is set by the 10 pixels per Hartmann spot selection. The center-to-center pixel spacing, referred to the intensifier input photocathode, is 52.4 microns. Therefore, the lenslet center-to-center spacing must be 10 x 52.4 microns, or 524 microns. This geometry results in a spot centered in each 10 x 10 pixel section. The focal length of the lenslets is selected to produce a diffraction limited spot size of the desired diameter. As will be shown in Section 4, a spot diameter equal to 2.5 to 3.0 times the pixel pitch is desired.

The lenslet array is fabricated by a photolithographic process by Corning. The clear aperture of each lenslet is 472 microns, and the desired focal length is 43 mm. Because the focal length for such high f-numbers cannot be controlled very well and also because the area between lenslets is not opaque when high f-numbers are produced by this process, we specify a focal length of 9 mm and adjust it by means of an index fluid. The lenslet is placed between two flat glass plates and the space between filled with a fluid with index of refraction chosen to result in the required 43 mm focal length.

The lenslet array described above is on order, but not yet received. We had on hand lenslet arrays of 880 micron center-to-center spacing and these were used to assemble a sensor with equivalent spot geometry on the photocathode. This was done with a reimaging lens that again produced spots of about 2.5 pixels in diameter, centered in 10 x 10 pixel areas. This optical system is much longer and not desirable for the telescope instrument. It did, however, allow laboratory experiments to proceed.

The 9 x 9 array of lenslets shown in Figure 1 result in the wavefront at the primary mirror being sampled in a diameter of 50/9.5 = 5.2 cm. This is about equal to the r_0 that is expected on good nights at the LLNL site.

3. Camera Description

The Kodak EktaPro 1012, shown in Figure 2, was developed by Kodak for motion analysis applications. This video camera has a two stage intensifier coupled to a 192 x 239 pixel NMOS photo-capacitor solid state sensor. The two stage intensifier is shown in Figure 3. The first stage is a generation 2 intensifier, which uses a microchannel plate (MCP) to provide the gain. A photoelectron emitted by the photocathode is accelerated and multiplied by the MCP. The electrons then strike a phosphor screen and form a brighter image than existed at the input photocathode. This image then is coupled to the

photocathode of the second stage generation 1 intensifier via a fiber optic plate. The photoelectrons released are accelerated and focused onto the phosphor screen of this stage. The intensified image on this phosphor is coupled through a second fiber optic plate to the sensor. The generation 2 stage can function as a high speed shutter, with gate times as low as 10 μs by controlling the potential between the photocathode and MCP.

The quantum efficiency of the input photocathode at 589 nm is approximately 5%, and the relative response of the photocathode and the sensor are shown in Figure 4. The photons striking the solid-state sensor are integrated for a period of time set by the frame rate. A full frame of 192 x 239 pixels can be read out at rates up to 1000 frames/second. Partial frames can be read out at higher rates. A screen split to 1/6 the full height can be read out at 6000 frames/second. In our application a frame rate of 1000 frames/second and a gate time of 1 ms (no "dead" time) are planned. The camera has enough solid-state memory to store 1200 full frames. Currently, frames are transferred to a PC for analysis via a GPIB interface. A special interface to permit a full frame 1 kHz transfer rate is being developed by LLNL and Kodak. This data will be processed in real time to determine the centroids and to control the deformable mirror.

Center-to-center pixel spacing of the sensor is 32 μm with a fill factor of 65%. The intensifier stages produce a demagnification such that the pixel spacing, referred to the input photocathnode, is 52 μm. The typical gain of the camera system from input photons (550 nm) to sensor output electrons is from 10,000 to 50,000. Other camera specifications are given in Table 1.

4. Experimental Results

Several experiments have been conducted to evaluate the camera described above for use as a wavefront sensor. The first tests used a single camera lens to obtain RMS wavefront tilt measurement error as a function of spot power and size. Signal decay time was next examined, and signal-to-noise measurements were made. With the single lens replaced by a lenslet array, wavefronts were measured at 1 kHz frame rates.

4.1 Wavefront Tilt Measurement Error

The set-up shown in Figure 5 was used to produce a spot of given size and power. The He-Ne laser beam is expanded and adjusted for flat wavefront using a shear plate. The polarizer is used for fine adjustment of the beam power level. Mirror M2 is mounted on a rotation stage which is driven by a stepper motor. A pinhole is placed at the input to the camera lens, which results in a diffraction limited spot (Airy profile) at the focal plane (intensifier input photocathode). The focal length of this lens is 50 mm.

The calibrated power meter cannot make accurate measurements directly at the low levels at which we test the camera. To make these power measurements, the ND filters are removed, and the power meter is inserted in the beam path. The measurement is made at this high level, and then the ND filters are inserted to drop the power level by known

amounts. The filters used were in the ND4 range. The power level at the photocathode is:

(1) $$P_{pc} = Pm \left(\frac{A_p}{A_m} \right) 10^{-ND} T_L, \quad \text{where}$$

P_m = Power Measured by Meter
A_p = Pinhole Area
A_m = Area of Power Meter Aperture
T_L = Lens Transmission

To obtain the same camera response at 589 nm as at 633 nm, the power level must be increased by $k = (R_{589}) / (R_{633})$ where R_{589} and R_{633} are the photocathode response at these wavelengths. For this camera, the ratio was 1.16. The power in terms of photons per unit time is:

(2) $P = (hc/\lambda)(N)(1/t)$ where

N = Number of Photons
t = Integration Time

For example, for 1000 photons/ms, we need 0.337 pw at 589 nm. Accounting for relative response difference, we need 0.392 pw at 633 nm. And finally, accounting for the lens loss (T_L= .9), we need 0.431 pw in the beam. We wanted to test at 1000, 2000, 4000, and 8000 photons/ms, and the required Pm was calculated for each case and obtained by adjusting the ND value and the polarizer rotation.

The spot was moved across the photocathode by rotating M2 to 60 discrete positions, spanning about seven pixels. Each spot position shift is, therefore, about 1/10 of a pixel. Each spot position change required 40 steps of the stepper motor. While it is possible to get a measure of wavefront tilt accuracy by taking repeated frames without moving the spot, we wanted to include any measurement errors arising from random spot to pixel orientations. The spot size is adjusted by choice of pinhole diameter. The diameter measured to the first dark ring is

(3) $D = 2.44 f\lambda/d$

where f is the lens focal length and d is the pinhole diameter. The pixel pitch, or center-to-center spacing, referred to the input photocathode is 52.4 μm. The pinhole sizes chosen resulted in spot diameter (D) to pixel pitch (P) ratios of D/P = 1.47, 1.99, 3.21, and 4.10.

To check the actual spot size compared to the calculated (2.44 fλ/d) spot size, a smaller pinhole with a 200 μm diameter was used to make a more easily resolved spot. The calculated spot diameter for this pinhole is 386 μm, or 386/52.4 = 7.4 pixels. Figure 6 shows the intensity distribution for this spot as captured by the camera. The diameter at

baseline is 7 pixels. The light level was intentionally increased to better see the wings, resulting in slight saturation at the center.

The spot was moved to 60 discrete positions on the photocathode, and for each position a 1 ms camera exposure was taken and the frame stored. The stepper motor and camera were controlled by a Mac II running LabView. After completion of a scan run, the 60 stored frames were transferred to a SUN workstation for analysis. There are many methods of calculation centroids. Stone[7] compared several of these digital centering algorithms used for centroiding star images and found that a modification to the moment algorithm produced the best results. The moment algorithm for calculating the x coordinate of the image is

$$(4) \qquad X_c = \sum_x X\,[M(x) - b] \quad / \sum_x [M(x) - b]$$

where

$$M(x) = \sum_y I(x, y)$$

is the signal sum over all y pixel elements for each x pixel position and b is the background level. In the modified moment algorithm most of the count data in the background are eliminated by selecting a threshold higher than that set by the background and then only considering those counts in the array above this threshold level in the centroiding process. This is done by thresholding each pixel as follows:

$$I(x, y) = I(x, y) - b \qquad \text{if} \qquad I(x, y) \geq T$$
$$I(x, y) = 0 \qquad \text{if} \qquad I(x, y) < T$$

Although centroiding star images against the sky-background is not the same as centroiding Hartmann spots, many of the issues are the same and we elected to use the moment algorithm with thresholding. In our case, the thresholding was performed by the camera electronic hardware rather than in the software. A fixed threshold (sometimes called black level) is set in the camera by observing an end pixel in each row which is metalized over and, hence, no light on it. In our experiments then, the software performed a simple moment calculation to obtain the centroid, with the camera operating with its normal fixed threshold.

For each of the 60 spot positions in the scan the centroid was calculated. The results are shown in Figure 7 with both the x and y coordinates . The RMS deviation to the straight line fit to the data was then calculated. This is the RMS measurement error in pixels. Figure 8 shows the RMS error in pixels for the four spot sizes and for spot powers of 1, 2, 4, and 8 thousand photons/ms.

As illustrated in Figure 9, a tilt of 1 wavelength across the aperture of diameter d causes a spot displacement of $\Delta x = f\lambda/d$. The number of waves per pixel is $P/\Delta x = Pd/\lambda f$. Since the spot diameter is $D = 2.44\ f/\lambda d$, the number of waves per pixel can also be expressed as 2.44 P/D. Using this conversion, the RMS centroid error in units of pixels is shown in Figure 10. Finally, this same data rearranged to show the error as a function of the spot size for the various spot powers is shown in Figure 11

The top curve (1,000 photons/ms) turns up at the largest spot size of 4.1 pixels because the S/N per pixel is getting too small. The curves at higher spot powers will also turn up, but at successively greater spot sizes. The optimum spot size increases for increasing spot power. To minimize the laser power required we must work with low signal levels. This pushes the optimum spot size to smaller values of around 2.5 pixels in diameter.

4.2 Camera Time Response

To faithfully capture spot position changes at high rates, the intensifier phosphor screens must have a decay time that is short relative to the frame time. The phosphor 90% to 10% decay time is specified as 120 ns, with a slower low level tail. This camera is designed for motion analysis at up to 6,000 frames/sec. (split screen) and phosphor decay times of the order of 200 μs would result in image blur. Transient response was measured to verify suitability for use as a wavefront sensor at 1 kHz sample rates.

To observe the transient response, a 200 μm pinhole was placed in front of the camera lens. A shutter moving across this pinhole makes light-to-dark and dark-to-light transitions in less than 100 μs. The camera was set at maximum gain, a gate time of 50 μs and a frame rate of 1 kHz. Figure 12 shows the results. The vertical axis is the signal level of a single pixel (256 gray scale), and the horizontal axis is the frame number. The graph at the left shows both transitions; top right shows an expanded view of the turn-off and the lower right an expanded view of the turn on. The 10% - 90% transition times are less than one frame time or 1 ms.

In operation the gate setting will be 1 ms, and each frame will integrate light for this period. The ability to measure changes in position or intensity will be limited by this integration time and not other camera effects such as phosphor decay.

4.3 Signal-to-Noise

The power signal-to-noise ratio of a photodetector with gain ahead of the signal amplifier, such as a photomultiplier, is given by [8, 9]

$$(5) \qquad (S/N)_p = \frac{G^2 (P_s e\eta/h\nu)^2}{2G^2 Fe\Delta f\,(i_s + i_b + i_d) + (4kT\Delta f/r)}$$

where

P_S = Signal power

e	=	Electronic charge
η	=	Quantum efficiency
G	=	Gain
Δf	=	Bandwidth
F	=	Noise factor in gain process
i_s	=	Signal current = $\eta P_s e/h\nu$
i_b	=	Background current = $\eta P_b e/h\nu$
P_b	=	Background power
k	=	Boltzmann's constant
η	=	Planck's constant
r	=	Load resistance
i_d	=	Dark current

In the signal shot noise limit, i_s dominates the noise terms and (assuming F = 1),

(6) $(S/N)_p = \eta P_s/2h\nu\Delta f$

if:

S	=	Signal photoelectrons/sec. (= $\eta P_s/h\nu$)
B	=	Background photoelectrons/sec.
D	=	Dark current electrons/sec.
R	=	Read noise electrons
t	=	Integration time (= $1/2\Delta f$)

the $(S/N)_p$ for a CCD with intensifier of gain G in front can be expressed as,

(7) $$(S/N)_p = \frac{S^2 t}{S + B + D + \frac{1}{G^2}(R^2/t)}$$

neglecting the background and dark current terms, this becomes

(8) $$(S/N)_p = \frac{S^2 t}{S + \frac{1}{G^2}(R^2/t)}$$

At gains high enough to suppress the read noise term, the signal shot noise limit of equation 6 is again obtained. This limit is shown in Figure 13 for a quantum efficiency of 5%. Also shown are four data points taken with our sensor. Signal powers of 500, 1000, 5000, and 10,000 photons/ms were made to be incident on a single pixel. One hundred frames, each with 1 ms integration time, were captured for each spot power. The mean signal to rms noise for each of these time traces were calculated. These are the data points of Figure 13. The $(S/N)_p$ is proportional to the signal strength (S) for the signal shot noise limit, but proportional to S^2 when we are read noise limited. The slope for the read noise limited case which intersects the 500 photon/ms data point is shown.

From Figure 13 we see that we are near the shot noise limit for signal levels above 1000 photons/ms. At 500 photons/ms, with the intensifier at maximum gain, we begin to have other noise terms start to dominate. From measurements described earlier, we need at least 1000 photons/ms to obtain accuracy better than $\lambda/10$ in tilt measurement. For a spot size of about 2.5 pixels in diameter, this would result in approximately 250 photons/ms on pixels near the center of the spot. Extrapolating the fit to the data in Figure 13, this corresponds to $(S/N)_p = 4$.

4.4 Wavefront Measurement

The wavefront sensor described in Section 2 was used to capture wavefront data from a collimated He-Ne beam being swept by a fast steering mirror, and also from a high rep-rate dye laser. The data from the He-Ne laser has not yet been analyzed. To illustrate the general performance, four frames of reconstructed wavefront of the dye laser are shown in Figure 14. The frame rate for Hartmann spot image capture was 1000 frames/sec. The four frames shown are at 1 ms time intervals. Frames (A) through (D) have a peak-to-valley wavefront deviation of 3.7, 1.6, 2.3, and 3.9 waves respectively. Significant tilt from frame to frame is easily seen.

The spot images were recorded at 1 kHz and stored in the camera processor memory. A maximum of 1200 full frames can be stored in this manner. The centroids and wavefront were calculated off-line on a SUN workstation. The hardware and software that perform these functions in real time are under development and are expected to be operational in six months.

5. Expected Performance with Laser Guide Star

The Guide Star experiments reported by MIT Lincoln Laboratory[10] resulted in approximately 40 photons of return signal per pulse in a 15 cm collection aperture. Accounting for differences in laser power and saturation level in the sodium layer, we expect about 19 photons/cm^2/s using the LLNL laser. This scaling of experimental data agrees very well with our model predictions of return signal level for our stretched pulse case. Knowing the performance of our wavefront sensor as a function of signal level, we can now relate wavefront measure error to subaperture diameter and integration time. This is done in Figure 15.

6. Conclusions

The Kodak EktaPro 1012 intensified motion analysis camera was found to be suitable for use as the wavefront sensor video imager in initial Guide Star experiments at LLNL. For signal levels of 1000 photons/ms per subaperture, the optimum Hartmann spot diameter is 2.5 - 3.0 pixels and yields local wavefront tilt information to better than $\lambda/10$ rms. The camera transient response is fast enough for operation at 1 kHz frame rates. The video memory of 1200 frames is sufficient to begin testing as a Hartmann wavefront sensor at 1

kHz rates, and development of continuous real-time data transfer to support this data rate is underway.

7. Acknowledgments

The authors wish to thank Claire Max, Herb Friedman, and Erlan Bliss of LLNL, and Jerry Van Vleck of Eastman Kodak for helpful discussions and support. We also thank John Toeppen of LLNL for providing the modified focal length lenslet array.

8. References

1. C. Max, K. Avicola, H. Bissinger, J. Brase, C. Chocol. H. Friedman, D. Gavel, J. Morris, S. Olivier, J.T. Salmon, K. Waltjen, "Feasibility Experiment for a Sodium-Layer Laser Guide Star Adaptive-Optics System," Laser Guide Star Adaptive Optics Workshop, Phillips Laboratory, Kirtland AFB, March 10-12, 1992.

2. H. Friedman, J. Horton, J. Morris, "System Design for High Power Sodium Beacon Laser," Laser Guide Star Adaptive Optics Workshop, Phillips Laboratory, Kirtland AFB, March 10-12, 1992.

3. D. Gavel, J. Morris, R. Vernon, "Sodium Guide Star Adaptive Optics System for Astronomical Imaging in the Visible and Near-Infrared," Laser Guide Star Adaptive Optics Workshop, Phillips Laboratory, Kirtland AFB, March 10-12, 1992.

4. K. Balch, "Image Intensification for High Speed Videography," SPIE vol. 1155 Ultrahigh Speed and High Speed Photography, Photonics, and Videography, pp. 189-202, 1989.

5. M. Brown, "Novel Technical Advances Provide Easy Solutions to Tough Motion Analysis Problems," SPIE vol. 1346 Ultrahigh and High-Speed Photography, Videography, Photonics, and Velocimetry, pp. 24-32, 1990.

6. K. Balch, "Bring Your Motion Analysis Out of the Dark," Research and Development, June 1990

7. R.C. Stone, "A Comparison of Digital Centering Algorithms," Astron, J. 97 (4), April 1989.

8. A, Yariv, "Optical Electronics," New York, 1985.

9. R.H. Kingston, "Detection of Optical and Infrared Radiation," New York, 1978.

10. R.A. Humphreys, et al., "Atmospheric-Turbulence Measurements Using a Synthetic Beacon in the Mesospheric Sodium Layer," Optics Letters, vol. 16, no. 18, September 15, 1991.

TABLE 1

Kodak EktaPro 1012 Specifications

System Features	
Image Rate:	30 to 6000 pictures per second
Gate Limits:	10 microseconds to 5 milliseconds
Gate Steps:	10, 15, 20, 30, 50, 70, 100, 150...
Gain Steps:	1 to 100 in increments of one
Intensified Imager	
Spectral Sensitivity:	Model VSG 440 nm to 700 nm at 50% level 350 nm to 800 nm at 10% level
Sensor Resolution:	15.6 1 p/mm (approximate)
Typical Illumination Example:	1000 FPS with 1 millisecond gate and a gain setting of 100 requires 1.5 lux
Warranty Life:	500,000,000 effective exposures
Size:	4" x 5" x 14" (approximate)
Weight:	Approximately 9 lbs.
Intensified Imager Controller	
Gain Control:	Increases or decreases light amplification (gain)
Gate Control:	Increases or decreases shutter speet (gate)
Overload Limit:	Threshold at which an exposure is classified as an overload
Overload Limit Steps:	25%, 50%, 100% and 200%
Trigger Input:	Strobe pulsefrom EKTAPRO Processor
Size:	8" x 14" x 11" (approximate)
Weight:	Approximately 17 lbs.
Cables:	Two 15 ft. cables are included; one from the Intensified Imager to the Processor and one from the Intensified Imager to the Controller. Optional cables may be added in 15, 50, or 100 ft. lengths, up to a maximum of 100 ft.
Processor	
Recording Technique:	Digital images stored in Dynamic Random Access Memory (DRAM)
Recording Modes:	RECORD: Records images until memory is full and then stops. RECORD-STOP: Continually records images until "stop" button is pushed. The last "n" images are saved in memory. RECORD-TRIGGER: Continually records images until a trigger signal is received. When signal is received, saves "n" images before trigger point. Continues to record until memory is full and then stops. RECORD-ON-COMMAND: Records images at the selected recording rate each time a user-supplied signal is received. May be used in conjunction with all the recording modes. EXTERNAL SYNCRONIZATION: Records at frame rates that correspond to a user-supplied signal.
Recording Rates:	50, 125, 250, 500 and 1000 full-frame images per second.
Frame Storage:	From 400 to 4800 full-frame images. Up to approximately 58000 split-frame images.
Playback Rates:	1, 2, 3, 4, 5, 6, 8, 10, 15, 30, 60, 90, 120, 240, 480 and 960 frames per second, plus single step freeze frame, forward or reverse.
Playback Modes:	One image per frame in cine mode or multiple images per frame in scroll mode.
Reference reticle:	Built-in X-Y electronic crosshairs with reference marker for data reduction.
Video Output:	NTSC or PAL. Dwnload to standard VCR tape.
DATA-FRAME Border:	Date, ID number, record rate, exposure rate, image split, elapsed time, playback rate, frame number, pixel depth, reticle position, real time and system status messages.
External Signal Inputs:	TRIGGER: TTL through BNC connector, positive or negative true logic. RECORD-ON-COMMAND: TTL through BNC connector, positive or negative true logic. EXTERNAL SYNC: TTL through BNC connector, positive or negative true logic.
Size:	17" x 19.5" x 12.75" (43 cm x 50 cm x 32 cm)
Weight:	Approximately 43 lbs. (20 kg)
Power:	110/220 FAC, 60/50 Hz, 5/3 amps

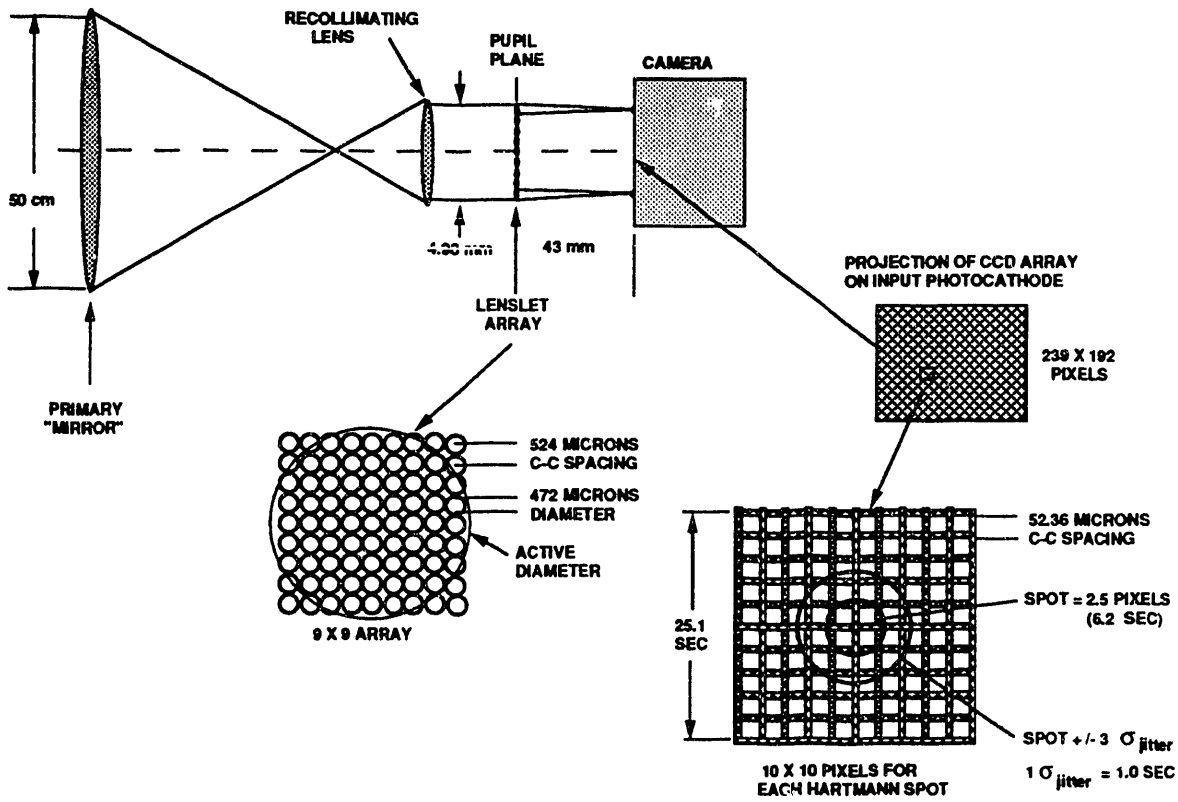

Figure 1. Wavefront Sensor Simplified Optical Schematic and Spot/Pixel Geometry

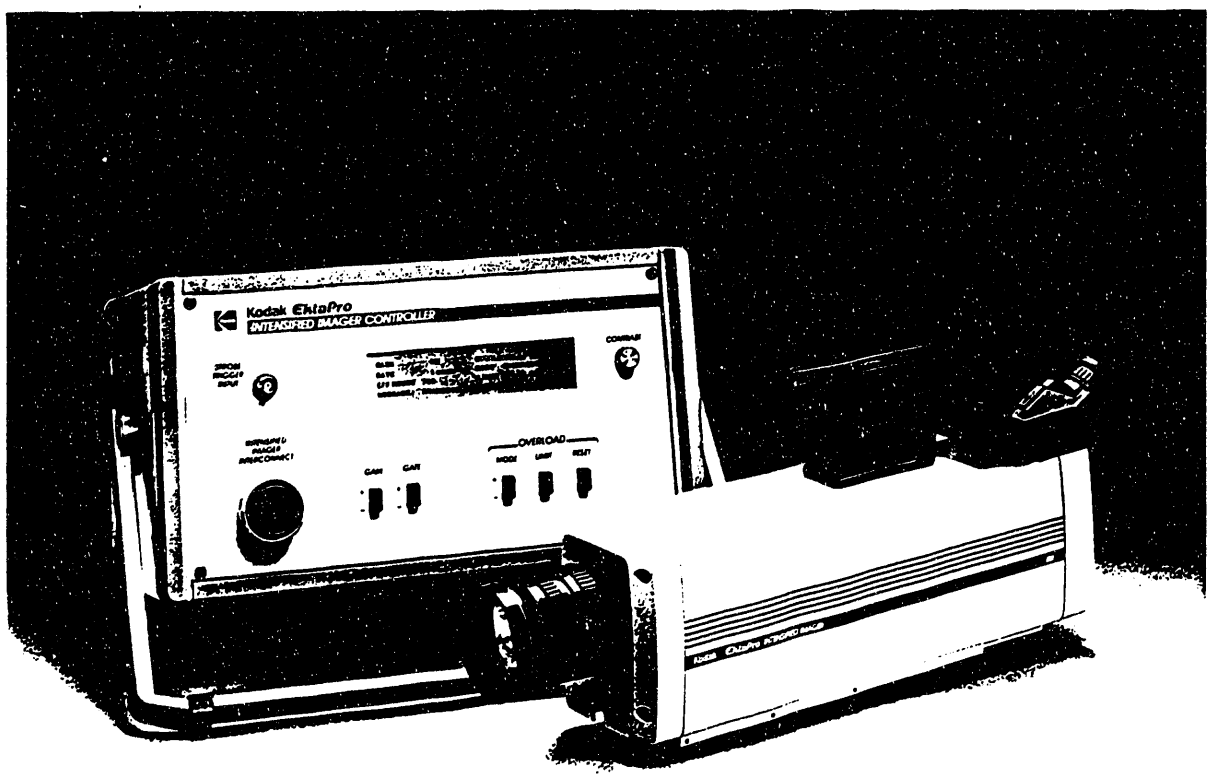

Figure 2. Kodak Intensified Imager and Intensifier Controller (Processor not Shown)

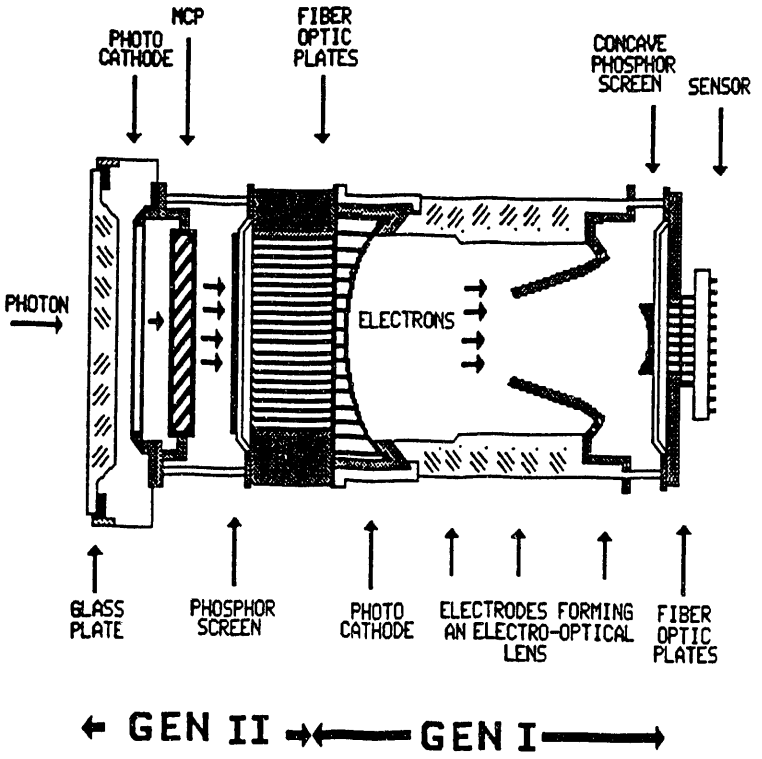

Figure 3. Two-Stage Intensifier Construction

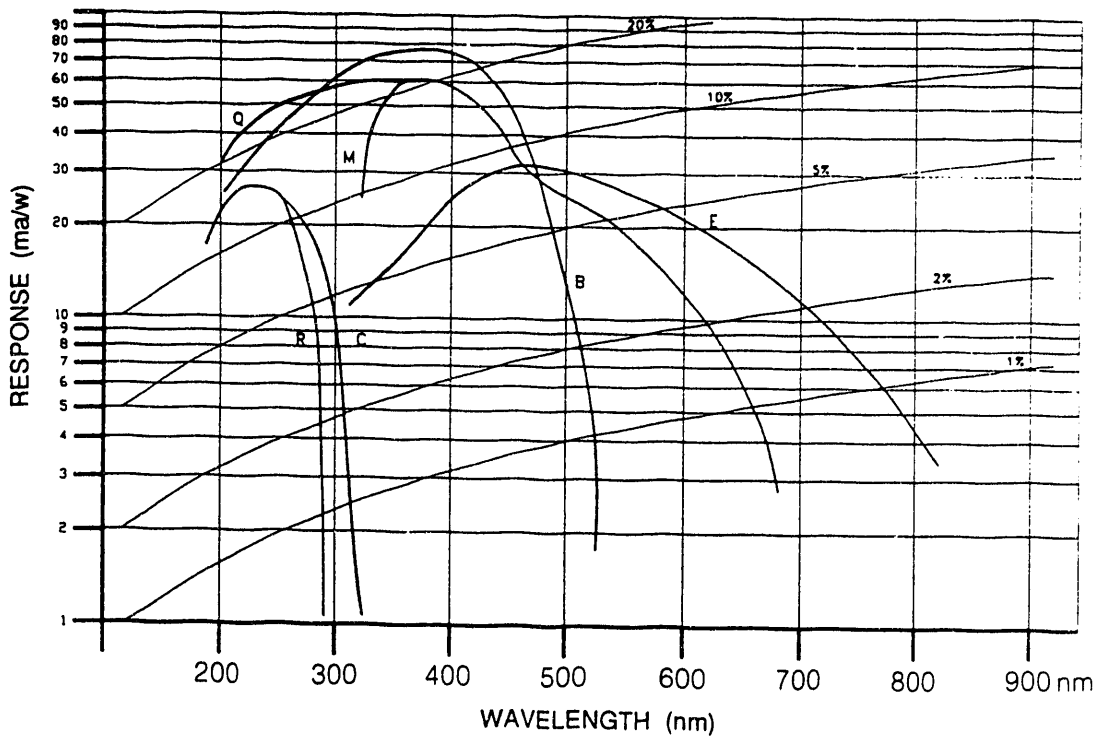

Figure 4. Relative Response of Several Photocathodes. Curve E is Photocathode Used in Kodak Camera Intensifier.

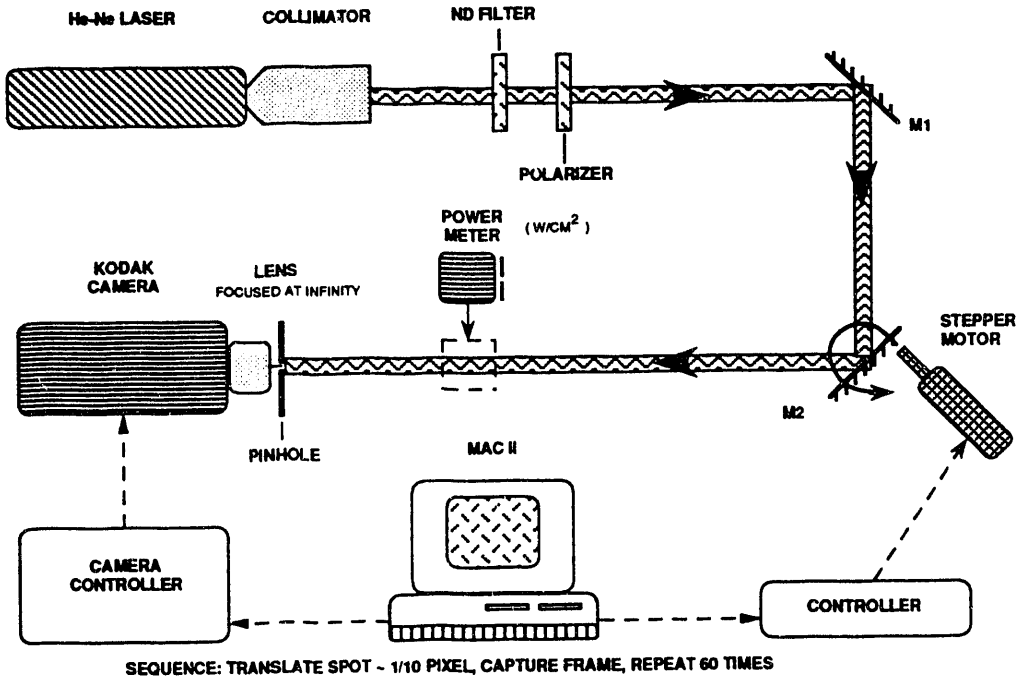

Figure 5. Experimental Set-Up For Wavefront Tilt Measurement Error

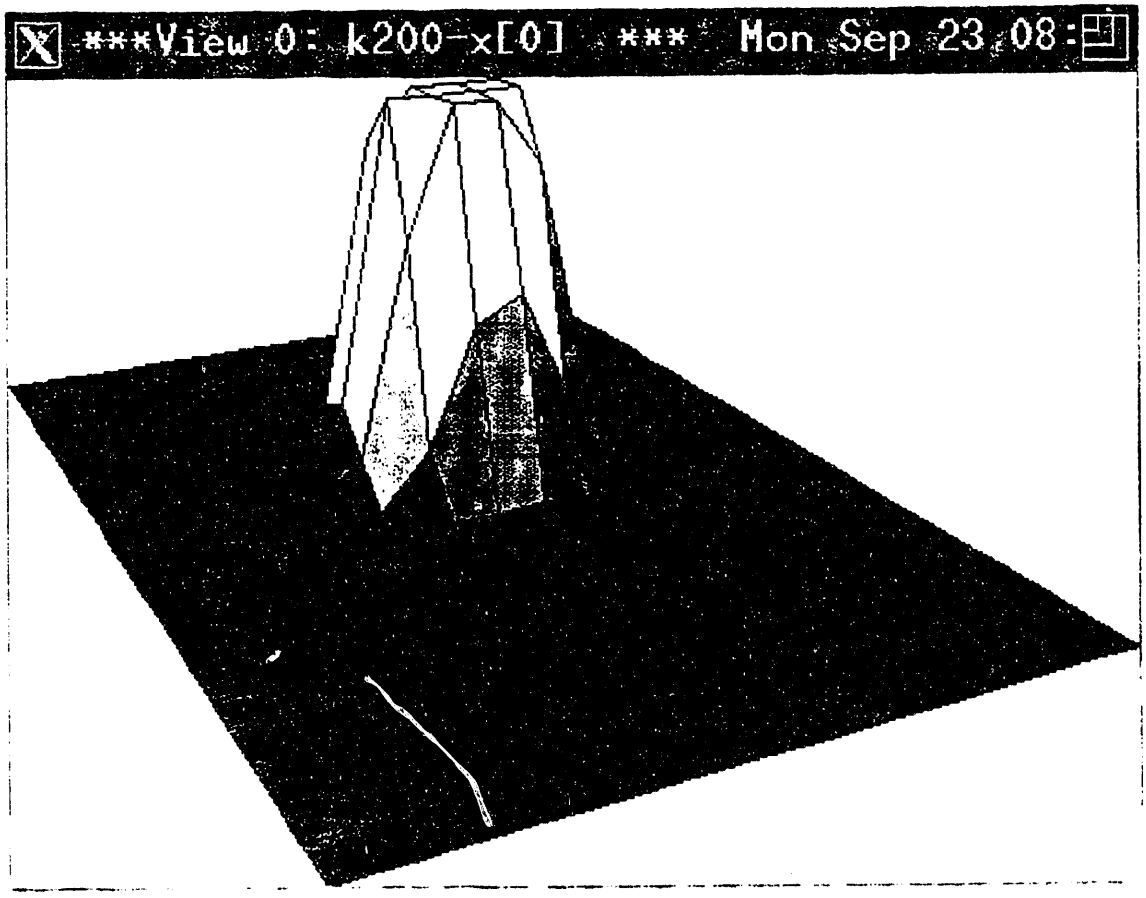

Figure 6. Spot Intensity Distribution with 200 Micrometer Pinhole

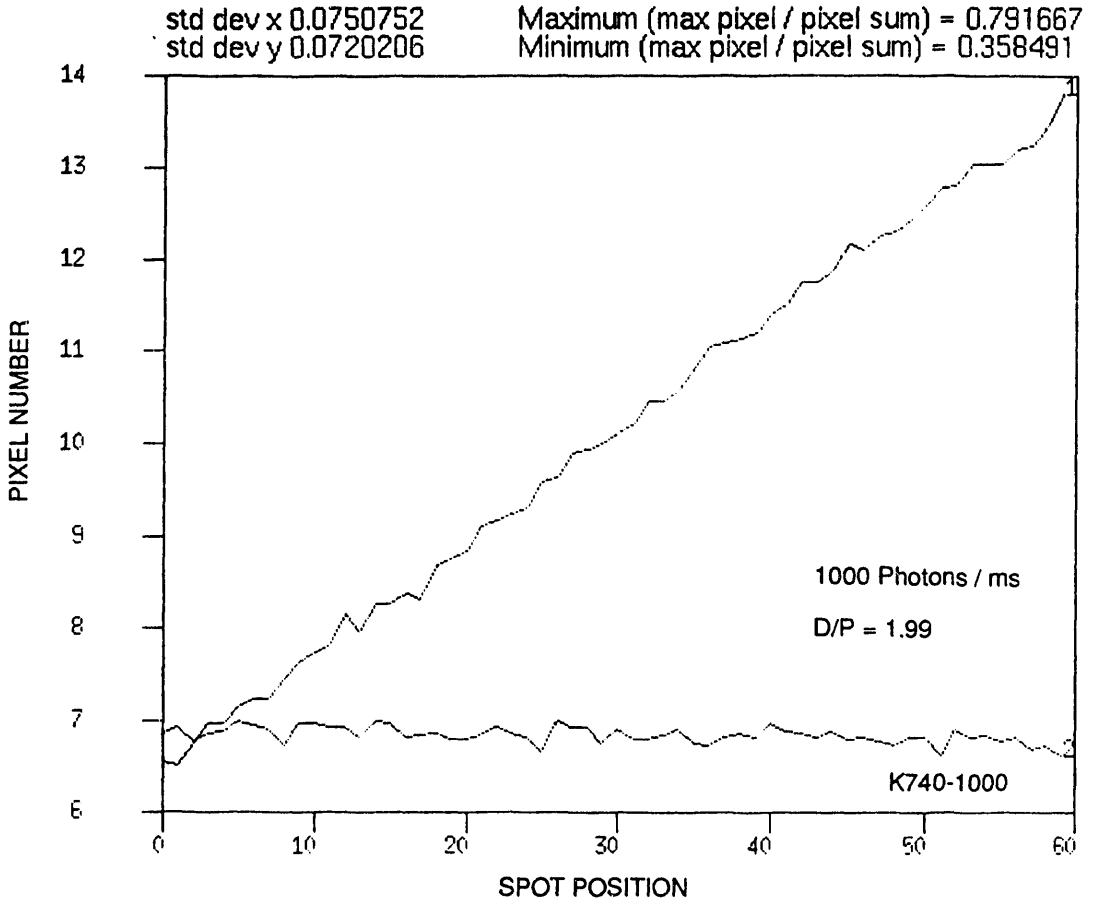

Figure 7. Calculated Centroid of Scanned Spot

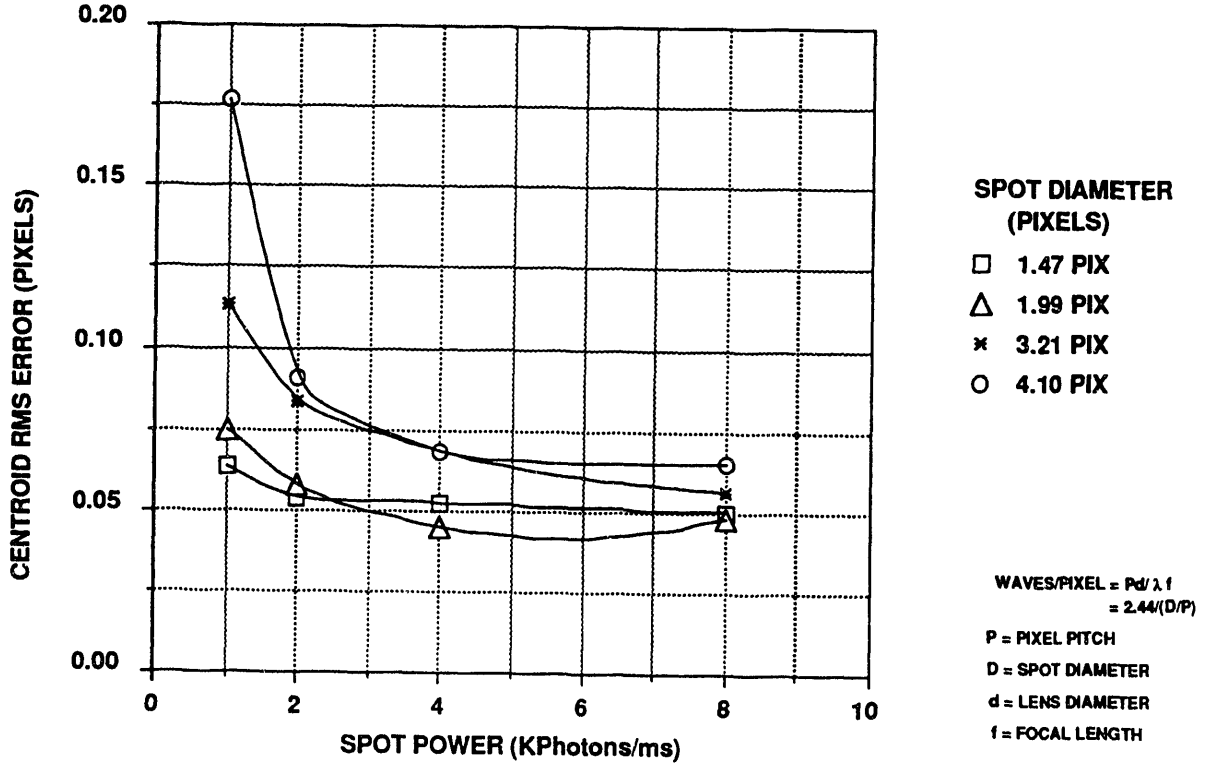

Figure 8. Centroid Error (Pixels) vs Spot Power

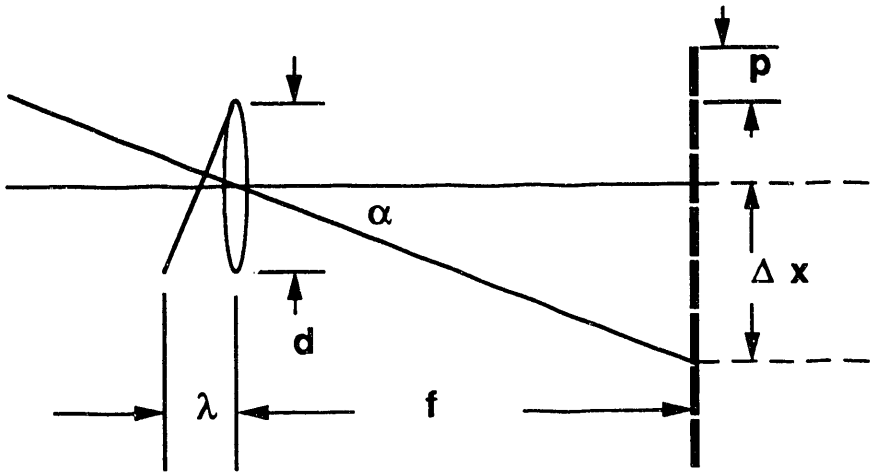

FOR 1 λ TILT $\alpha = \lambda / d$

$\Delta x = f \lambda / d$

WAVES / PIXEL = $P / \Delta x$

$= Pd / \lambda f$

FOR DIFFRACTION LIMITED SPOT, DIAMETER D TO FIRST DARK RING
D = 2.44 f λ /d , EXPRESSED IN PIXEL UNITS,
D/P = 2.44 f λ / dP , AND SUBSTITUTING IN ABOVE
WAVES / PIXEL = 2.44/ (D/ P)

Figure 9. Conversion from Pixels to Waves

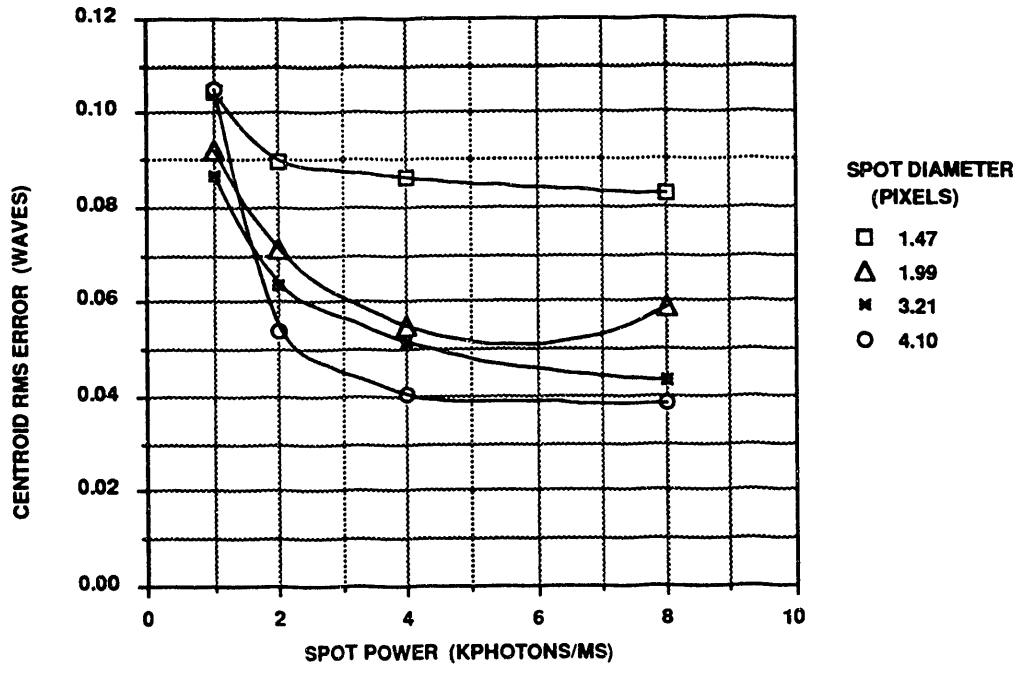

Figure 10. Centroid Error in Waves vs Spot Power

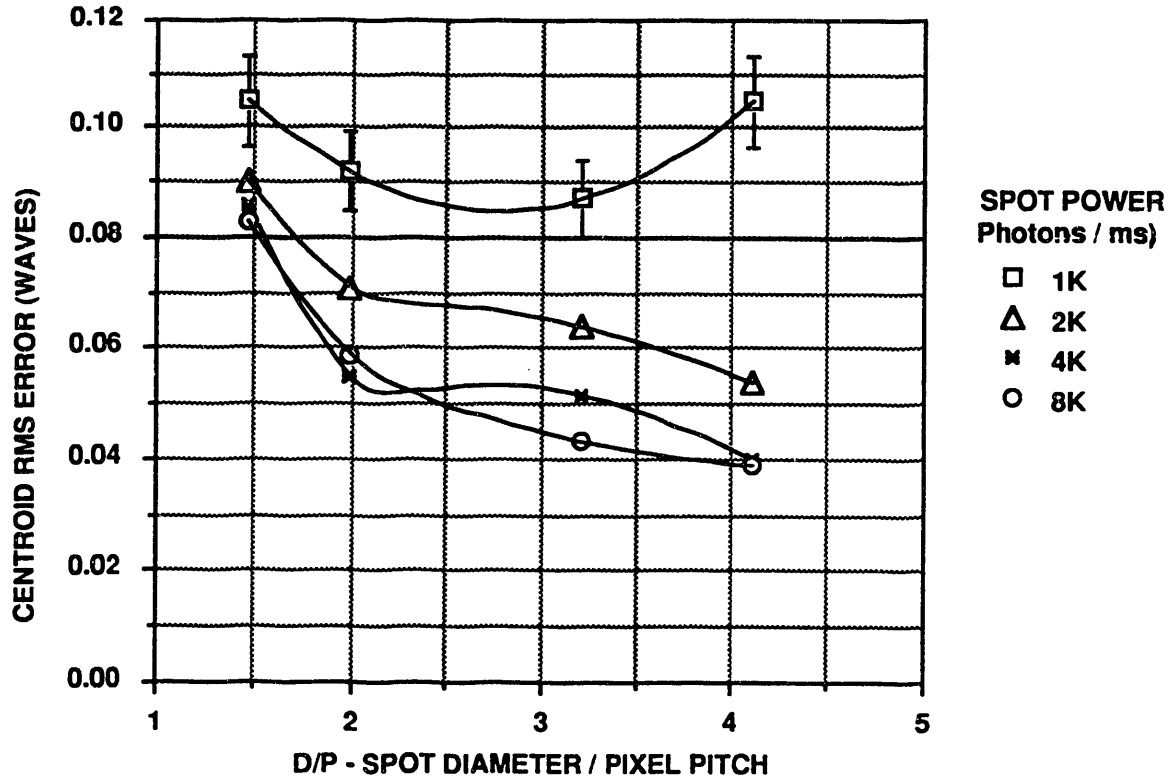

Figure 11. Centroid Error in Waves as Function of Spot Size (in Units of Pixels)

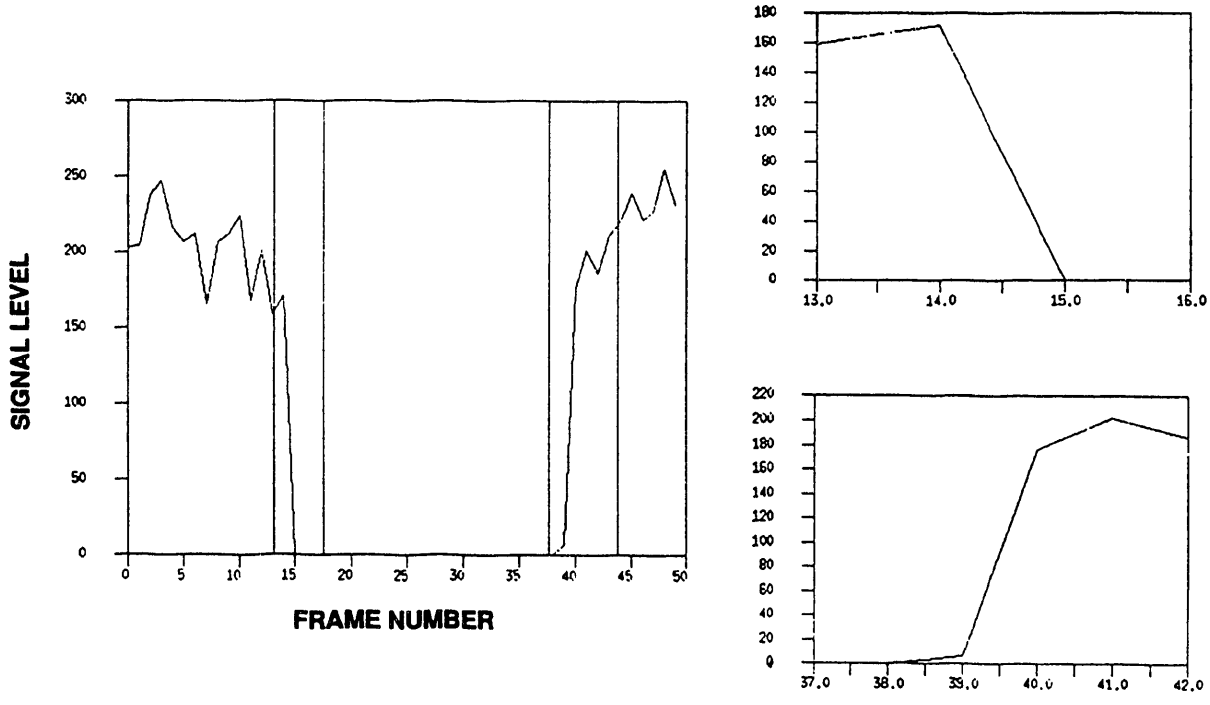

Figure 12. Response to Transient Light Levels

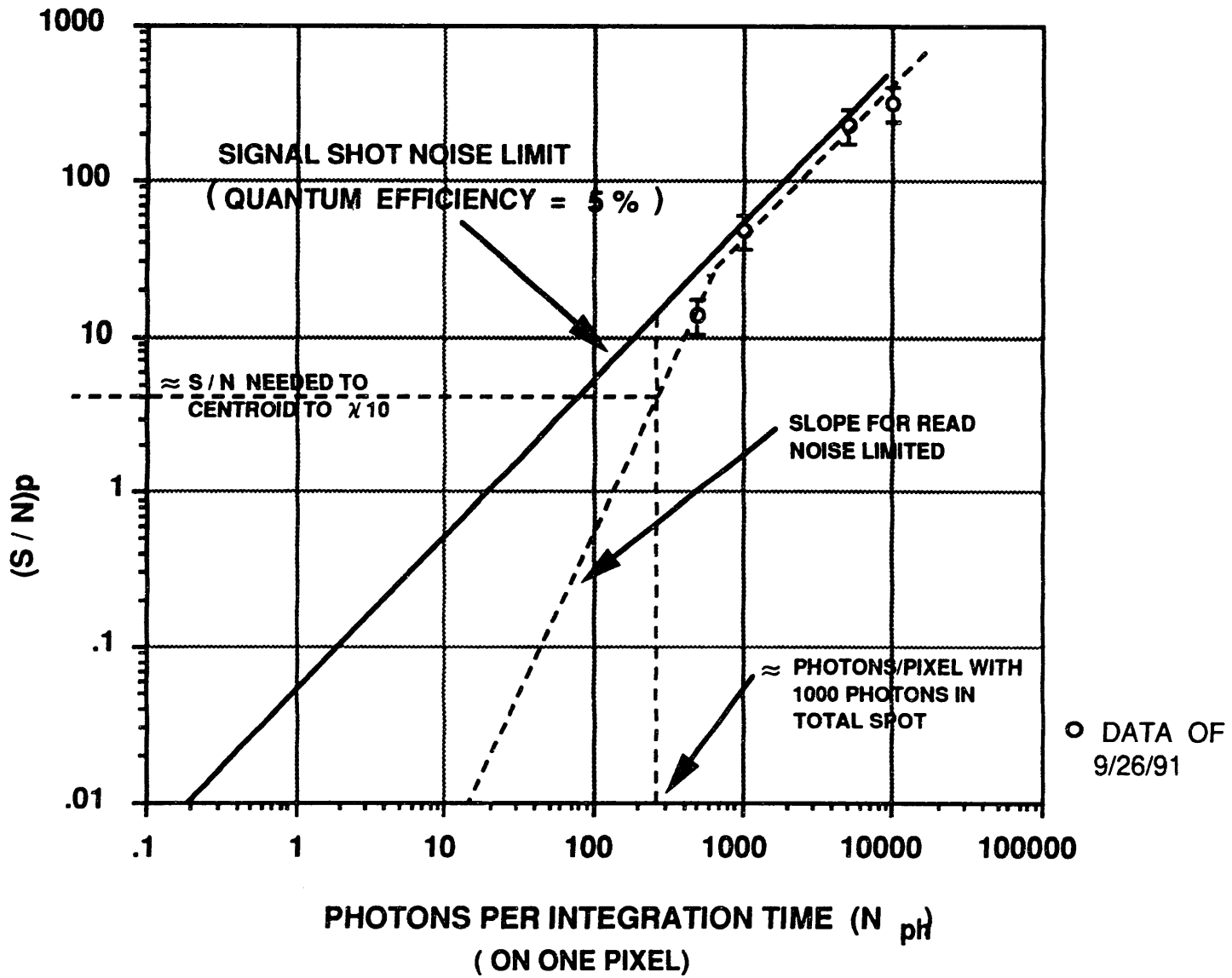

Figure 13. Signal-to-Noise Ratio Relative to the Signal Shot Noise Limit

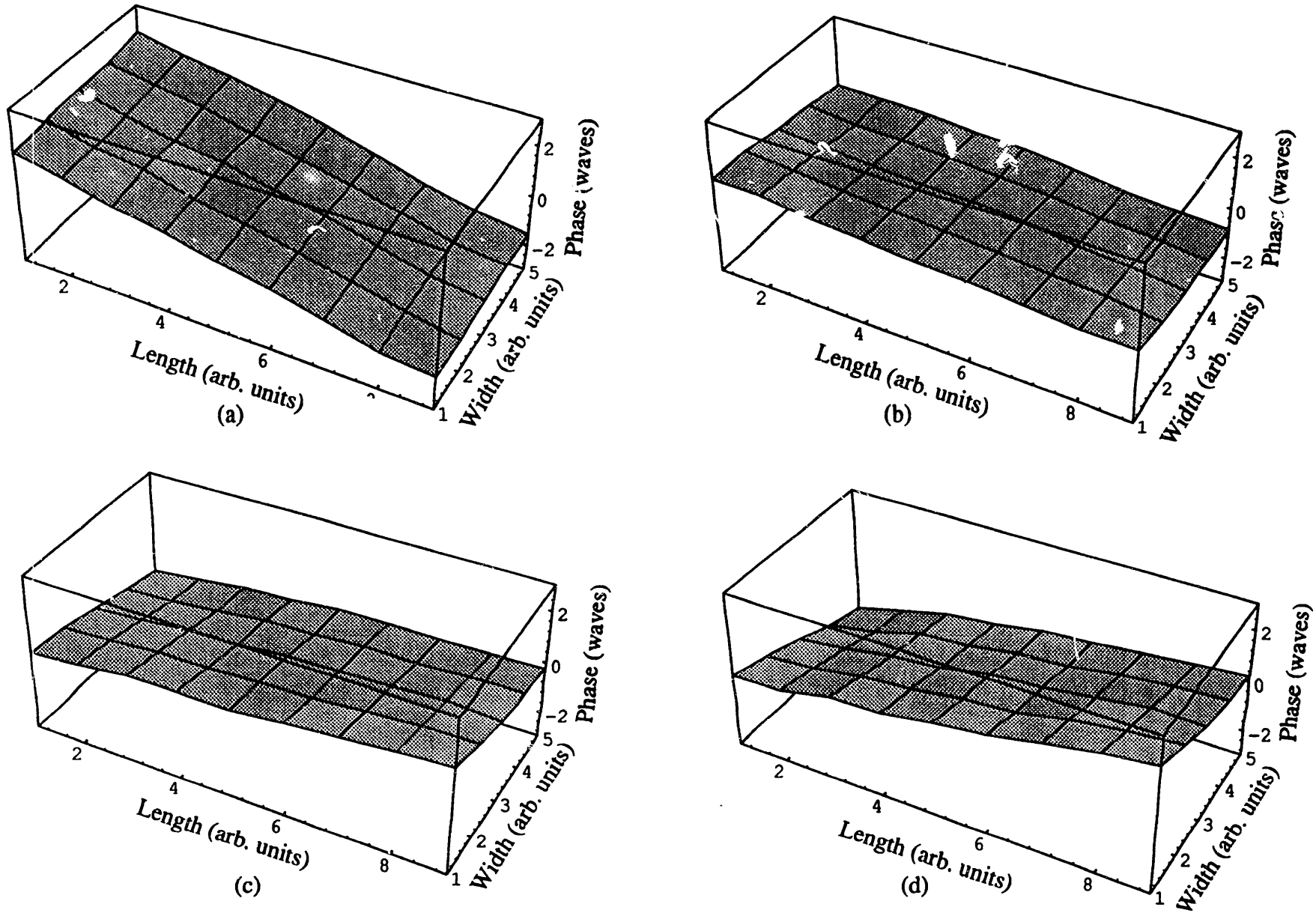

Figure 14. Reconstructed laser wavefront with 1 ms between frames. Peak-to-valley values are (a) 3.7 waves, (b) 1.6 waves, (c) 1.2 waves and (d) 3.9 waves.

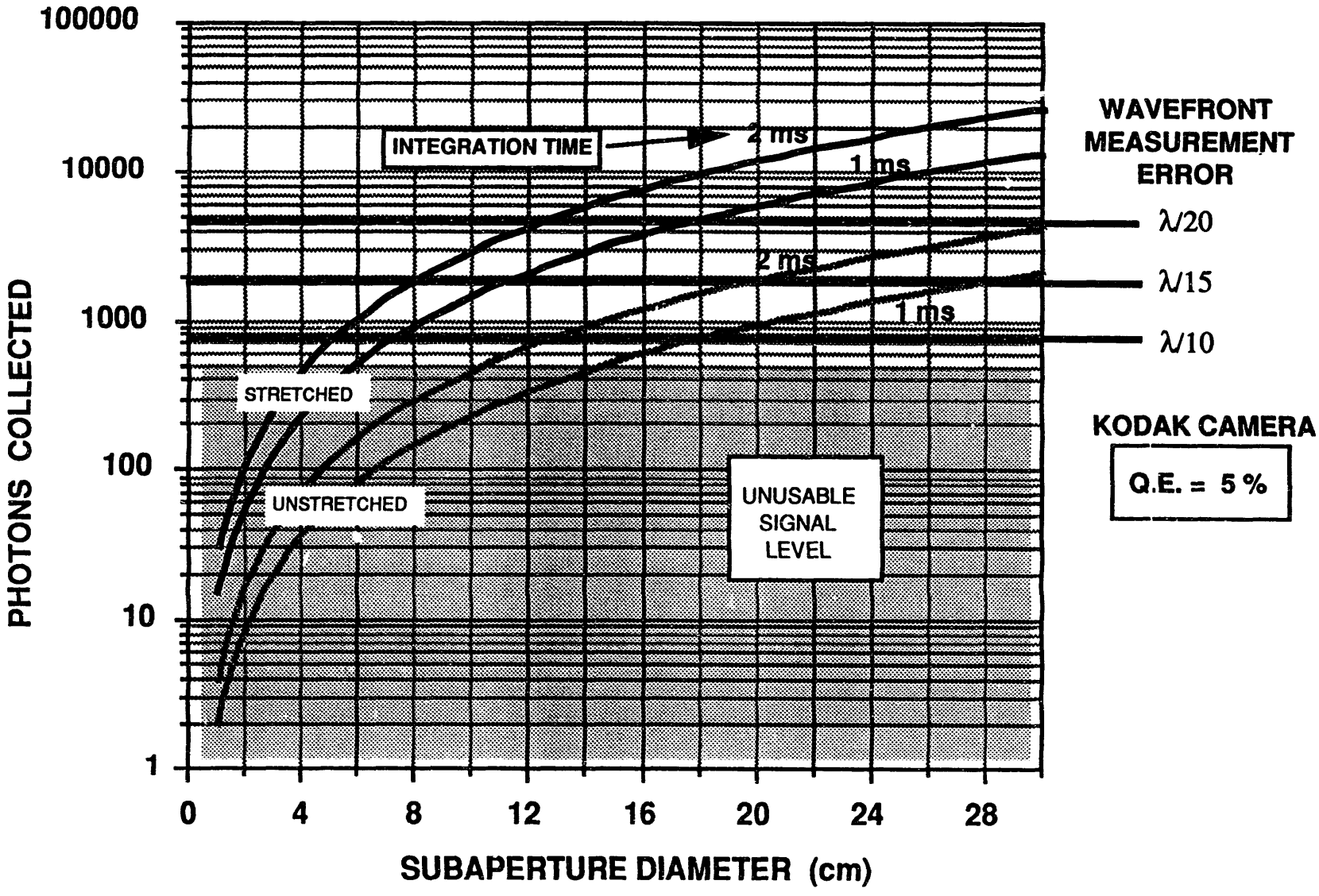

Figure 15. Expected Guide Star Return Signal Levels and Wavefront Sensor Performance with 5% Quantum Efficiency Photocathode on Kodak Camera.

V.

Resolution Limits for Ground-Based Astronomical Imaging

by

S. S. Olivier, C. E. Max, D. T. Gavel, and J. M. Brase

RESOLUTION LIMITS FOR GROUND-BASED ASTRONOMICAL IMAGING

Scot S. Olivier, Claire E. Max, Donald T. Gavel, James M. Brase

Lawrence Livermore National Laboratory

ABSTRACT

We study the residual jitter present in astronomical images after the effect of the earth's atmosphere has been compensated using a fast steering mirror. This residual jitter places a limit on the resolution that can be achieved for long exposure images even when more elaborate adaptive optics systems are used to correct the image. We assume that the fast guiding system uses a star as its reference source. Then, from the observed characteristics of Galactic stellar populations, we are able to predict the optimal performance of the fast guiding system as a function of the sky covering factor, that is the fraction of the sky for which the given level of performance can be achieved. The performance for a particular sky covering factor is optimized by choosing the appropriate closed-loop bandwidth and guide star magnitude.

The performance also depends on a number of atmospheric and system parameters; however, we find that the optimal performance is relatively insensitive to all but two of these parameters, the telescope aperture size and the strength of the atmospheric turbulence. Therefore, we consider two specific examples: first, a ten meter telescope imaging through an atmosphere with relatively weak turbulence (3/4 arcsecond seeing in V), and second, a one meter telescope imaging through an atmosphere with relatively strong turbulence (2 arcsecond seeing in V). For these cases we find, for example, that a residual jitter of less than 0.03 and 0.3 arcseconds respectively can be obtained over about half the sky for nominal choices of the other parameters. The required closed-loop bandwidths in these cases are about 5 and 20 Hz while the appropriate guide stars are approximately 18th and 14th magnitude in V.

1. INTRODUCTION

The resolution of ground based astronomical images is limited by atmospheric turbulence to angular sizes that are much larger than the theoretical diffraction limit of typical observatory telescopes. Adaptive optics systems offer the possibility of correcting the turbulence induced image degradation and producing near diffraction limited images; however, in general, the achievable resolution will be somewhere between the atmospheric *seeing* and the telescope diffraction limit.

By using a *laser guide star* it is theoretically possible to obtain corrected images anywhere on the sky; however, even with an arbitrarily bright laser guide star, it may not be possible to achieve diffraction limited resolution. The fundamental problem is that even an adaptive optics system that uses a laser guide star, must make an *independent* estimate of the tilt component of the wavefront aberration since the absolute position of the laser guide star is dependent on the atmospheric characteristics along the upgoing beam path which are not typically known. Thus, even if perfect phase conjugation is performed by the adaptive optics system relative to the laser guide star, thereby creating an instantaneous diffraction limited image, the tilt aberration introduced in the upgoing beam path will cause the long-exposure image to be smeared out. Consequently, even in elaborate adaptive optics systems using a laser guide star, it is necessary to correct for image motion.

The simplest technique to measure and correct for image motion of an astronomical object is first to measure the tilt component of the wavefront from a star which is in close angular proximity to the object and then to use an adaptive optics element with two degrees of freedom to actively compensate the temporal variations in tilt. This is typically done by monitoring the x-y centroid position of the stellar image and using a fast steering mirror in a feedback loop to stabilize that position. In this paper, we study the fundamental limits on the accuracy of such techniques.

2. TILT COMPENSATION ERROR

There are four main sources of error inherent in tilt compensation. Each of these errors is introduced because of a difference between the estimate of the tilt for the reference stellar wavefront and the actual tilt in the wavefront of the astronomical object being imaged. The first error source is simply the finite signal-to-noise-ratio (SNR) in the reference wavefront tilt measurement (Tyler and Fried 1982). The second error source is the finite angular separation between the reference and the astronomical object being imaged

error source is the finite angular separation between the reference and the astronomical object being imaged (Fried 1976). The third error source is the finite closed-loop bandwidth of the tilt compensation system (Tyler 1988). The fourth and final error source is the presence of higher order aberrations, specifically pure coma of all orders, in the reference wavefront (Tyler 1985).

We denote the one-axis rms tilt error corresponding to each of the four error sources by σ_{cSNR}, σ_{ta}, σ_{bw} and σ_{cc} respectively. To first order, we can treat the errors from each of these four sources as being uncorrelated; therefore, the square of the total residual jitter will be given by their quadrature sum; $\sigma^2_{tilt} = \sigma^2_{cSNR} + \sigma^2_{ta} + \sigma^2_{bw} + \sigma^2_{cc}$. In the next section, we describe how to minimize the residual jitter by choosing an appropriate reference star and system bandwidth.

3. OPTIMAL TILT COMPENSATION: THEORY

The fundamental factor limiting a tilt compensation system that uses a star as its reference is the distribution of stars both in angular number density and magnitude. In choosing a reference there is typically a trade-off between the star's brightness and its angular proximity to the astronomical object being imaged. A brighter star will give a larger SNR so that σ_{cSNR} will be reduced; however, there are fewer bright stars, so the angular separation between an arbitrary astronomical object and a star will be larger for a brighter star, and σ_{ta} will be increased. The opposite sense of the dependence of σ_{cSNR} and σ_{ta} on stellar magnitude, m, suggests that an on optimal m can be found for which the quadrature sum of these two terms is a minimum.

A similar trade-off exists for the choice of the system bandwidth. Since the system bandwidth differs from the sampling frequency by a fixed numerical constant, systems with lower bandwidths will have smaller sampling frequencies and thus longer sampling times. Since increasing integration time raises the SNR, a system with a lower bandwidth will have a larger SNR so that σ_{cSNR} will be reduced; however, lowering the system bandwidth will increase σ_{bw}. Once again, the opposite sense of the dependence of σ_{cSNR} and σ_{bw} on system bandwidth, f_c, suggests that an optimal f_c can be found for which the quadrature sum of these two terms is a minimum.

The process of minimizing the residual jitter, σ_{tilt} therefore involves finding the minimum of the quadrature sum $\sigma^2_{cSNR} + \sigma^2_{ta} + \sigma^2_{bw}$ in the two dimensional space defined by the variables m and f_c. We have done this using a simple bisection method for both variables. Of course, it is first necessary to specify all of the remaining parameters (other than f_c and m). In the next section, we present the results of example calculations for which specific choices of these parameters have been made.

TABLE 1. Nominal system and operational parameter values

parameter description	symbol	nominal value
telescope aperture diameter	D	10 m (Mauna Kea) 1 m (Livermore)
mean wavelength	λ	0.6 μm
effective optical bandwidth	$\delta\lambda_e$	0.1 μm
detector noise equivalent detected photons per sample	n_d	100
reference image geometry factor	β	2.5
ratio of sampling frequency to closed loop bandwidth	κ	10
sky covering factor	P_{sky}	0.5
Galactic latitude	b	30°
zenith angle	ϕ	30°

4. OPTIMAL TILT COMPENSATION: EXAMPLE CALCULATIONS

Before the optimization calculation described in the previous section is performed, we must specify a variety of parameters. First, we must determine three atmospheric characteristics: C_n^2 (refractive index structure constant), V_w (wind speed) and I_{sky} (sky surface brightness). Then we must specify six tilt compensation system parameters: D (telescope aperture diameter), λ (mean wavelength), $\delta\lambda_e$ (effective optical bandwidth), n_d (detector noise), β (reference image geometry factor) and κ (ratio of sampling frequency to closed-loop bandwidth). Next, we must chose three operational parameters: P_{sky} (sky covering factor), b (galactic latitude) and ϕ (zenith angle). Finally, it is necessary to know the characteristics of the Galactic stellar populations, namely $\Sigma_m(b)$ (stellar angular number density) and T_e (mean stellar effective temperature).

The nominal values for the system and operational parameters are given in Table 1. We calculate $\Sigma_m(b)$ by interpolating the star count data (for visual magnitudes) from Allen (1973). We also use a single value of $T_e = 6000$ K for all m and b.

Since the atmospheric parameters vary considerably with geographic location, we consider two sets of nominal parameters. The first set of characteristics corresponds to typical conditions found on Mauna Kea (Hawaii) for which enough measurements have been reported in the literature (e.g. Roddier 1990) that we are able to develop reasonably detailed models. For the second set of nominal atmospheric parameters, we use models corresponding to the conditions typically expected in Livermore (California) where we are currently involved in a program to construct a laser guide star and adaptive optics test facility. In this case no detailed measurements for this particular site are available so we use estimates made with data taken at similar sites.

Figures 1 and 2 show plots of our models of $C_n^2(z)$ and $V_w(z)$ respectively for both Mauna Kea and Livermore. We use $I_{sky}(\lambda) = (21.8\ \lambda\ \mu\text{m}^{-1} - 7.2) \times 10^{-18}$ J s^{-1} m^{-2} μm^{-1} μrad^{-2} for the sky background on Mauna Kea. This corresponds to a sky brightness of 21.2 magnitudes per square arcsecond in the V band. For the sky background at Livermore we use the expression for Mauna Kea multiplied by a factor of 12 corresponding to a sky brightness of 18.5 magnitudes per square arcsecond in the V band.

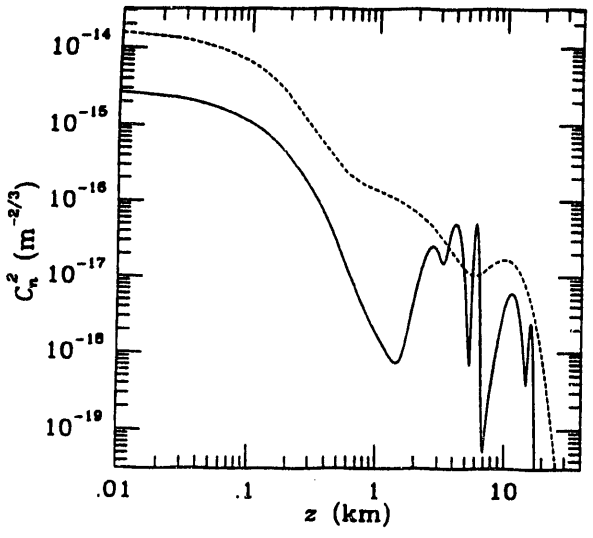

Figure 1. Nominal forms of $C_n^2(z)$ supposed to be typical for Mauna Kea (solid line) and Livermore (dashed line). These forms of C_n^2 correspond to 3/4 and 2 arcsecond seeing in V respectively.

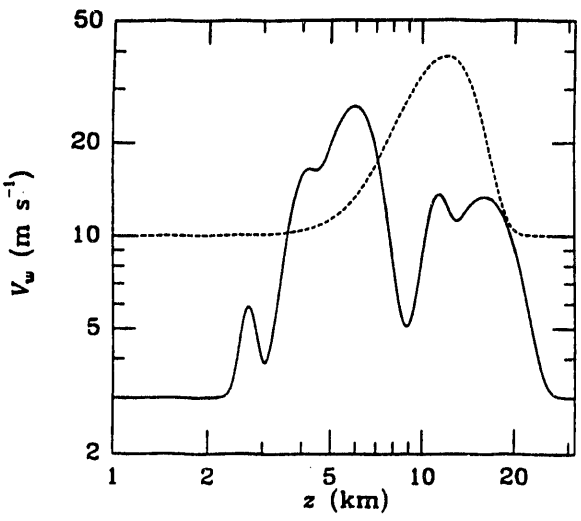

Figure 2. Nominal forms of $V_w(z)$ supposed to to be typical for Mauna Kea (solid line) and Livermore (dashed line).

The results of our optimization calculation for $\sigma_{\rm tilt}$ versus P_{sky}, with all other parameters equal to their nominal values, are shown in Figure 3. Figure 3 also shows each of the four contributing error terms separately. It is clear from Figure 3a that the dominant error term on Mauna Kea is σ_{cc}; however, more elaborate wavefront sensing techniques can, in theory, eliminate this error so that the residual jitter would be given by the quadrature sum of the other three terms, which is also shown in Figure 3a. On the other hand, Figure 3b shows that the dominant term at Livermore is $\sigma_{\rm ta}$.

Figure 4 shows the optimal values of f_c and m corresponding to the results for the residual jitter shown in Figure 3. Also shown in Figure 4 is the guide star separation, α, which sets the required field of view for the system.

Having determined the residual jitter, we can now calculate the FWHM of the PSF for a compensated imaging system (which produces diffraction limited short exposure images). If the diffraction limited *Airy pattern* of the telescope is approximated as a Gaussian with the same FWHM, and is then convolved with a Gaussian residual jitter component with a variance $\sigma^2_{\rm tilt}$, the resulting PSF is another Gaussian with a FWHM given by $\theta_{FWHM} = 1.03\,[(\lambda_{obs}/D)^2 + (\sigma_{\rm tilt}/0.437)^2]^{1/2}$, where λ_{obs} is the mean wavelength at which the observation is being made. Note that λ_{obs} may be different from the mean wavelength for the tilt compensation system, λ.

Dividing $1.03\,\lambda_{obs}$ by θ_{FWHM} gives the ratio of the diffraction limited FWHM to the actual FWHM (including the residual jitter) in units of the aperture diameter. Thus, $D_e = \lambda_{obs}\,[(\lambda_{obs}/D)^2 + (\sigma_{\rm tilt}/0.437)^2]^{-1/2}$ This corresponds to the aperture diameter of a telescope with diffraction limited resolution equal to the resolution obtained by the actual telescope and image compensation system (assumed to produces diffraction limited short exposure images) after the effects of the residual jitter are taken into account.

Figure 5 shows the effective diffraction limited diameter as a function of the sky covering factor calculated using the results for $\sigma_{\rm tilt}$ shown in Figure 3. Since D_e is also a function of the observing wavelength, we plot the results for six of the Johnson photometric bands (B, V, R, I, J, K). Figure 5 also shows the results for Mauna Kea neglecting the effect of σ_{cc} (i.e. assuming $\sigma^2_{\rm tilt} = \sigma^2_{cSNR} + \sigma^2_{\rm ta} + \sigma^2_{\rm bw}$).

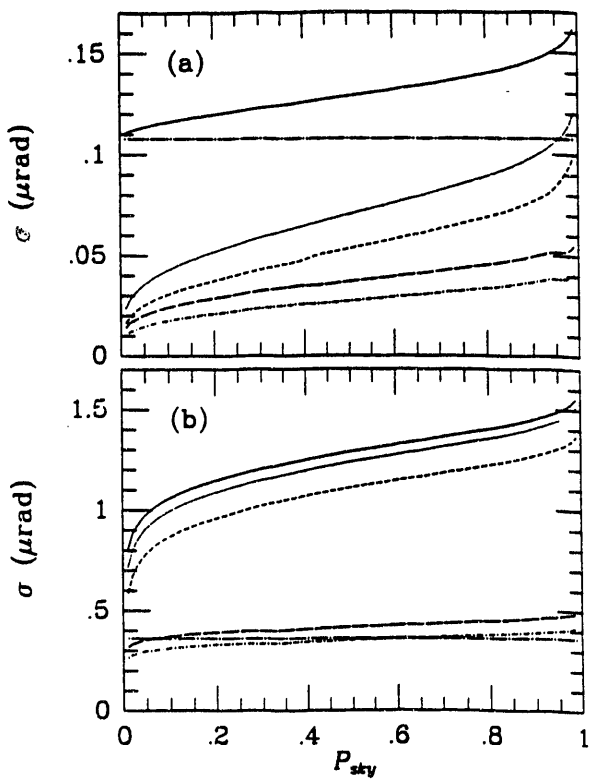

Figure 3. Residual jitter and contributing rms tilt errors corresponding to optimal choices of guide star magnitude and closed-loop bandwidth as a function of the sky covering factor for Mauna Kea (3a) and Livermore (3b). The curves shown are $\sigma_{\rm tilt}$ (solid line), $\sigma_{\rm ta}$ (short-dashed line), σ_{cSNR} (long-dashed line), $\sigma_{\rm bw}$ (short-dash-dotted line), σ_{cc} (long-dash-dotted line) and $(\sigma^2_{\rm tilt} - \sigma^2_{cc})^{1/2}$ (dotted line).

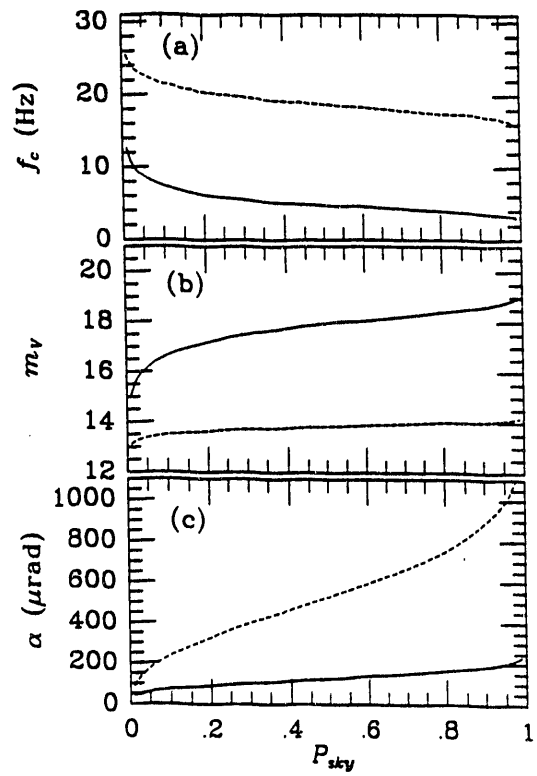

Figure 4. Optimal closed-loop bandwidth (4a), guide star magnitude (4b) and guide star angular distance (4c) as a function of the sky covering factor for Mauna Kea (solid lines) and Livermore (dashed lines).

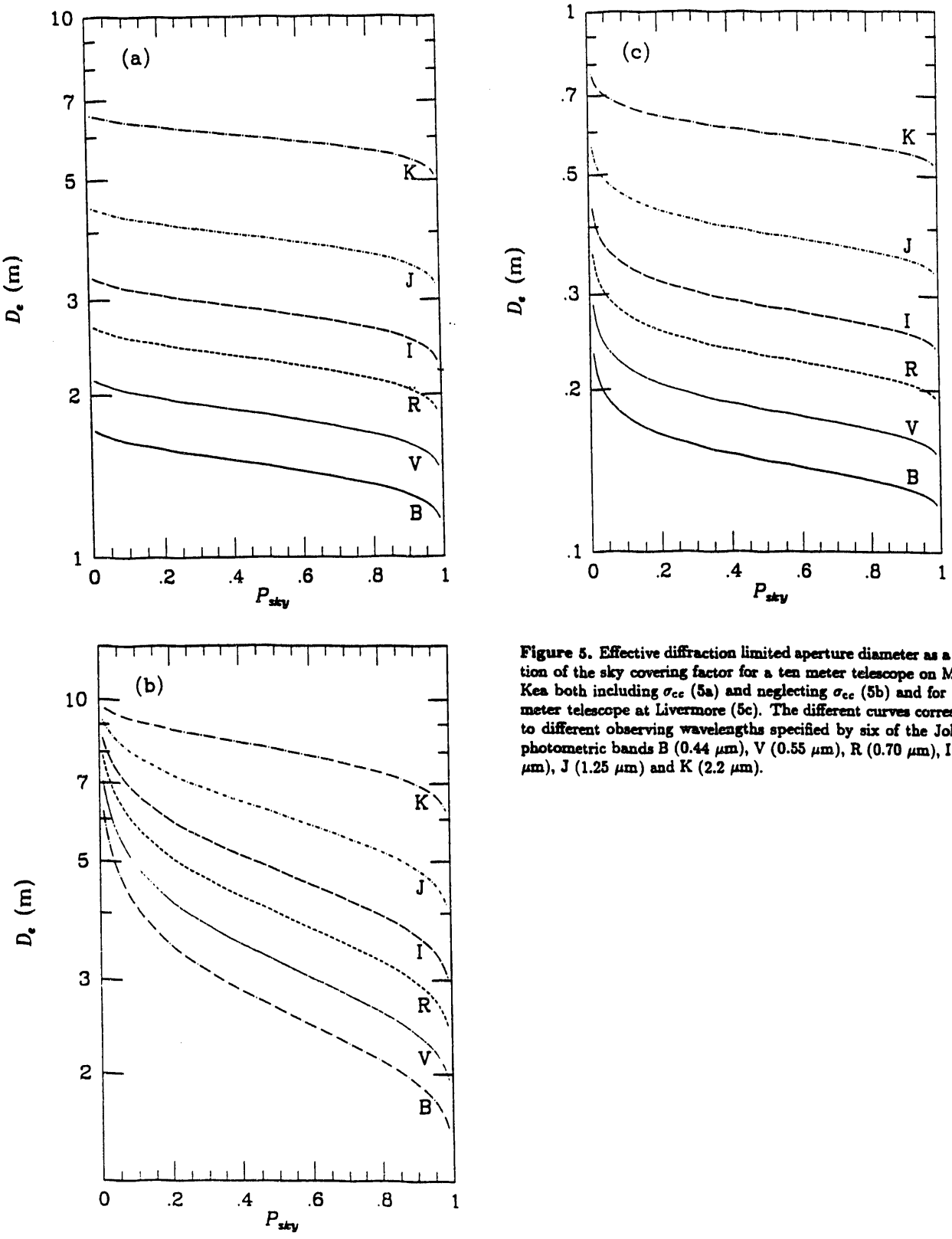

Figure 5. Effective diffraction limited aperture diameter as a function of the sky covering factor for a ten meter telescope on Mauna Kea both including σ_{cc} (5a) and neglecting σ_{cc} (5b) and for a one meter telescope at Livermore (5c). The different curves correspond to different observing wavelengths specified by six of the Johnson photometric bands B (0.44 μm), V (0.55 μm), R (0.70 μm), I (0.88 μm), J (1.25 μm) and K (2.2 μm).

5.0 CONCLUSIONS

We have calculated the optimal performance for a tilt compensation system that uses an uncorrected image from a single natural star as its reference. The performance is optimized for each value of the sky covering factor by choosing the appropriate guide star magnitude and closed-loop bandwidth.

When the tilt compensation system uses a simple centroid measurement, we find that a ten meter telescope imaging through an atmosphere with characteristics typically found at Mauna Kea can obtain long exposure images over about half the sky with resolutions that range from about 15% diffraction limited in B (0.44 μm) to about 60% diffraction limited in K (2.2 μm).

The limiting error source in this case is the presence of higher order aberrations in the reference wavefront that cause the reference image centroid to give a biased estimate of the reference wavefront tilt. If this error is eliminated, then resolutions ranging from about 25% diffraction limited in B to 80% diffraction limited in K can be obtained over about half the sky. This resolution is an order of magnitude better than can be obtained at the best seeing sites without any image compensation; furthermore, it is as good as the diffraction limit of HST in B and a factor of three better in K.

Work performed under the auspices of the U.S. Department of Energy by Lawrence Livermore National Laboratory under Contract W-7405-Eng-48.

REFERENCES

Allen, C. W. 1973, *Astrophysical Quantities* (The Athlone Press) p. 244.
Fried, D. L. 1976, *SPIE*, **75**, p. 20.
Roddier, F. *et al.* 1990, *SPIE*, **1236**, p. 485.
Tyler, G. A. 1985, *TOSC*, Report No. TR-634.
Tyler, G. A. 1988, *TOSC*, Report No. TR-887.
Tyler, G. A., and Fried D. L. 1982, *JOSA*, **72**, p. 804.

DATE
FILMED
6/23/94
END